NASA/TP—1999-208522

High-Area-Ratio Rocket Nozzle at High Combustion Chamber Pressure—Experimental and Analytical Validation

Robert S. Jankovsky and Timothy D. Smith
Glenn Research Center, Cleveland, Ohio

Albert J. Pavli
NYMA, Inc., Brook Park, Ohio

National Aeronautics and
Space Administration

Glenn Research Center

June 1999

Available from

NASA Center for Aerospace Information
7121 Standard Drive
Hanover, MD 21076
Price Code: A04

National Technical Information Service
5285 Port Royal Road
Springfield, VA 22100
Price Code: A04

HIGH-AREA-RATIO ROCKET NOZZLE AT HIGH COMBUSTION CHAMBER PRESSURE—EXPERIMENTAL AND ANALYTICAL VALIDATION

Robert S. Jankovsky and Timothy D. Smith
National Aeronautics and Space Administration
Glenn Research Center
Cleveland, Ohio 44135

and

Albert J. Pavli
NYMA, Inc.
Engineering Services Division
Brook Park, Ohio 44142

Summary

Experimental data were obtained on an optimally contoured nozzle with an area ratio of 1025:1 and on a truncated version of this nozzle with an area ratio of 440:1. The nozzles were tested with gaseous hydrogen and liquid oxygen propellants at combustion chamber pressures of 1800 to 2400 psia and mixture ratios of 3.89 to 6.15. This report compares the experimental performance, heat transfer, and boundary layer total pressure measurements with theoretical predictions of the current Joint Army, Navy, NASA, Air Force (JANNAF) developed methodology. This methodology makes use of the Two-Dimensional Kinetics (TDK) nozzle performance code.

Comparisons of the TDK-predicted performance to experimentally attained thrust performance indicated that both the vacuum thrust coefficient and the vacuum specific impulse values were approximately 2.0-percent higher than the turbulent prediction for the 1025:1 configurations, and approximately 0.25-percent higher than the turbulent prediction for the 440:1 configuration.

Nozzle wall temperatures were measured on the outside of a thin-walled heat sink nozzle during the test firings. Nozzle heat fluxes were calculated from the time histories of these temperatures and compared with predictions made with the TDK code. The heat flux values were overpredicted for all cases. The results range from nearly 100 percent at an area ratio of 50 to only approximately 3 percent at an area ratio of 975. Values of the integral of the heat flux as a function of nozzle surface area were also calculated. Comparisons of the experiment with analyses of the heat flux and the heat rate per axial length also show that the experimental values were lower than the predicted value.

Three boundary layer rakes mounted on the nozzle exit were used for boundary layer measurements. This arrangement allowed total pressure measurements to be obtained at 14 different distances from the nozzle wall. A comparison of boundary layer total pressure profiles and analytical predictions show good agreement for the first 0.5 in. from the nozzle wall; but the further into the core flow that measurements were taken, the more that TDK overpredicted the boundary layer thickness.

Introduction

The design and analysis of efficient, high-area-ratio rocket nozzles requires the knowledge of core flow effects, boundary layer effects, contour effects, supersonic shock effects, wall heat transfer effects, and the specific impulse attainable. Data on these effects have been difficult to obtain because there are few altitude test facilities available for testing nozzles with area ratios in the range of 700:1 to 1000:1. As a result, the primary tools for nozzle designers are theoretical methods incorporated in numerical codes. Many of these codes are based on the Joint Army, Navy, NASA, Air Force (JANNAF) prediction methodology outlined in reference 1. One of the computer programs most often used for nozzle analysis is the Two-Dimensional Kinetics (TDK) Nozzle Performance Computer Program (ref. 2). As stated in reference 3, when the methodology was developed, area ratios of 100:1 were considered large-area ratio nozzles. In the past 20 years, the need for increased performance from orbital transfer vehicles has required investigation into area ratios of up to 1000:1. Several experimental programs have been undertaken to validate codes developed with the JANNAF methodology at higher area ratios (refs. 3 to 7). As a result of these activities, the codes are considered validated for low-area-ratio nozzles (up to 300:1) and are being used to extrapolate results to high-area-ratio nozzles. These extrapolations lack confidence without experimental validation and raise questions as to the relevance of trade studies for future rocket engine designs. Hence an experimental program (ref. 8) was undertaken to provide data to validate the codes for high-area-ratio nozzles at high chamber pressures. As part of this effort, a series of tests were conducted in the altitude test capsule at the

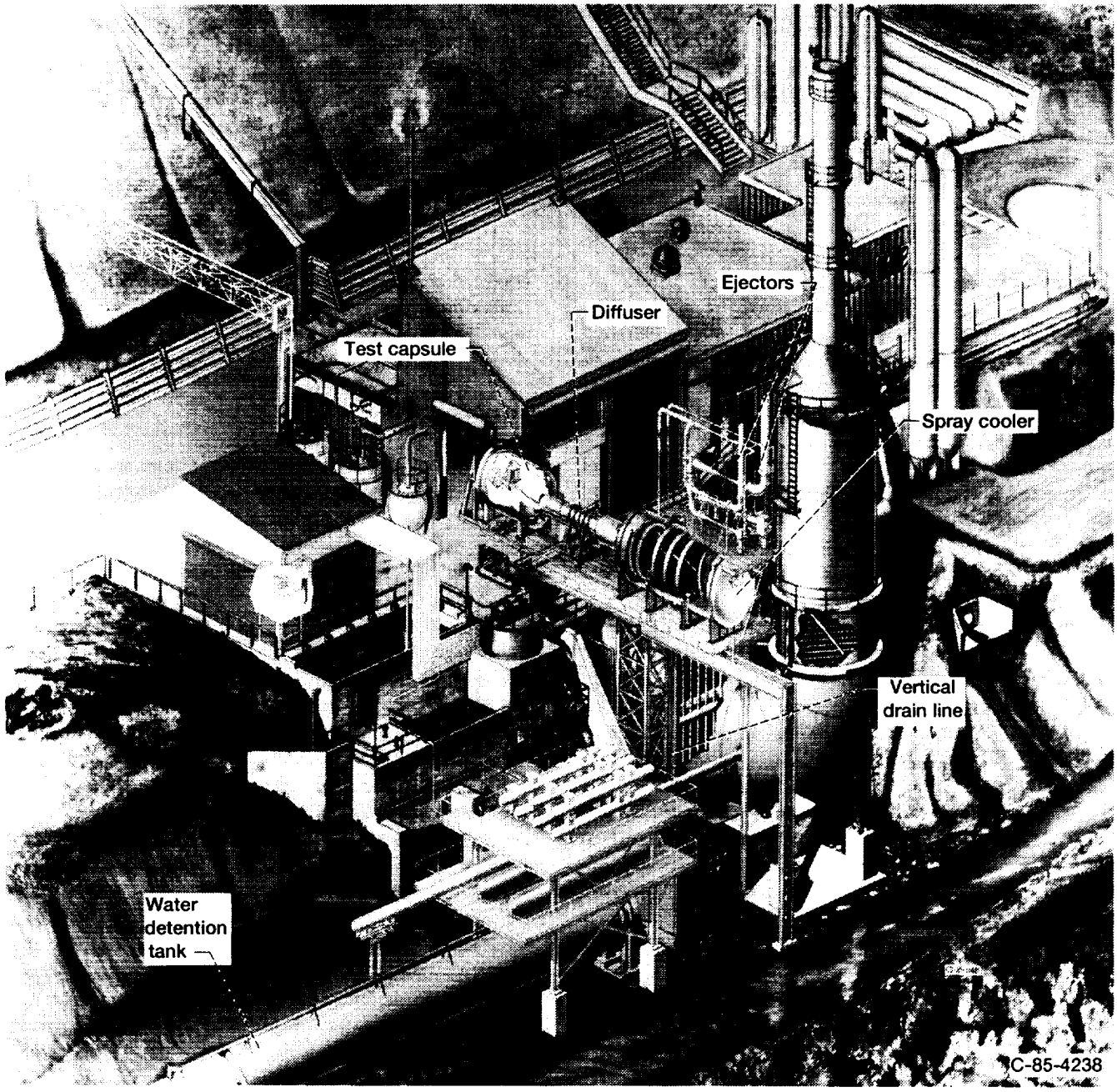

Figure 1.—NASA Lewis Research Center's Rocket Engine Test Facility.

NASA Glenn Rocket Engine Test Facility (RETF). Previous tests in this program were reported to be in the laminar boundary-layer regime (refs. 3 to 5) at a nominal combustion-chamber pressure of 2.4 MPa (350 psia) and at a Reynolds number, based on throat diameter, that ranged from 3.11×10^6 to 4.14×10^5. Present tests were considered to be in the turbulent boundary-layer regime at combustion-chamber pressures that ranged from 12.4 to 16.5 MPa (1800 to 2400 psia) and Reynolds numbers, based on throat diameter, that ranged from 1.43×10^6 to 2.05×10^6 (ref. 9). The nozzles used in these tests had nominal 2.54-cm- (1.00-in.-) diameter throats with area ratios of 1025:1 and 440:1, and were fired with gaseous hydrogen and liquid oxygen. This report compares the performance and heat transfer test results with the theoretical predictions of the TDK computer code. In addition, boundary layer rakes were used to measure the total pressure profile of the boundary layer for comparison with analytical predictions. A symbols list is provided in appendix A.

Apparatus

Facility

Testing was conducted at the NASA Glenn Rocket Engine Test Facility (RETF) (fig. 1) and utilized on the facility's altitude test capsule, thrust stand, propellant feed system, and data acquisition system. The altitude test capsule (fig. 2) simulated the static pressure at altitude by three methods of vacuum pumping, all acting simultaneously. The first method, a second-throat diffuser, utilized the kinetic energy of the rocket exhaust to pump the nozzle flow into a spray cooler. The second method chilled the exhaust gas in the spray cooler where approximately half was condensed to liquid water and drained. The third method pumped the remaining uncondensed exhaust by nitrogen-driven ejectors. The facility ejector system reduced the capsule pressure to approximately 4.1 kPa (0.6 psia), with further pumping accomplished by the engine exhaust. Additional facility details are given in references 4 and 8.

The thrust stand, which had a full-scale measurement range of 17.8 kN (4000 lb_f), was designed to have a standard deviation (2-σ) variation of less than ±0.1 percent of full scale. With the test capsule at altitude pressure, the thrust stand was calibrated against a reference load cell, which had a 2-σ variation of less than ±0.05 percent of full scale and a calibration traceable to the National Institute of Standards and Technology (NIST).

The propellant feed system consisted of a gaseous hydrogen fuel circuit and a liquid oxygen oxidizer circuit. High-pressure gaseous hydrogen bottles comprised the fuel circuit; the oxidizer circuit was a high-pressure liquid oxygen tank pressurized from high-pressure gaseous helium bottles (fig. 3). The flow rates were measured with calibrated venturis.

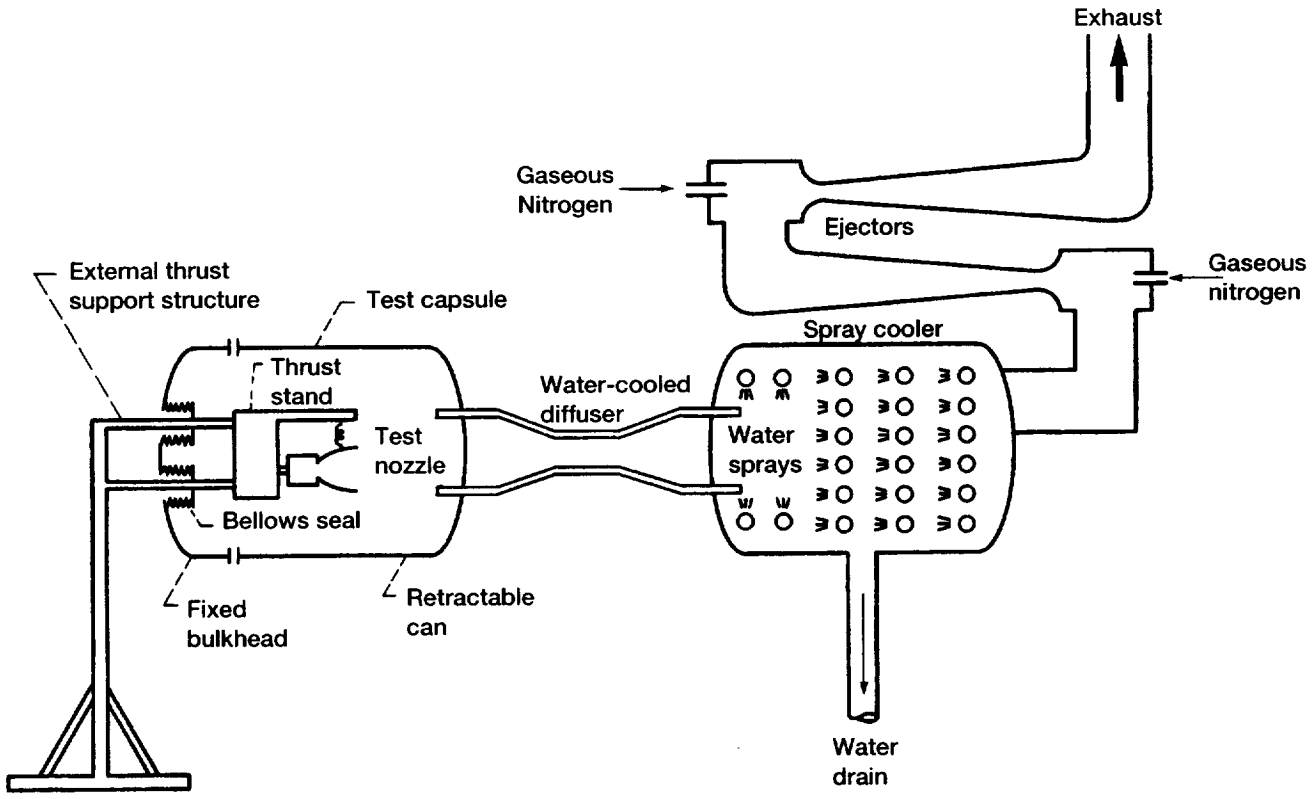

Figure 2.—Schematic of altitude test facility.

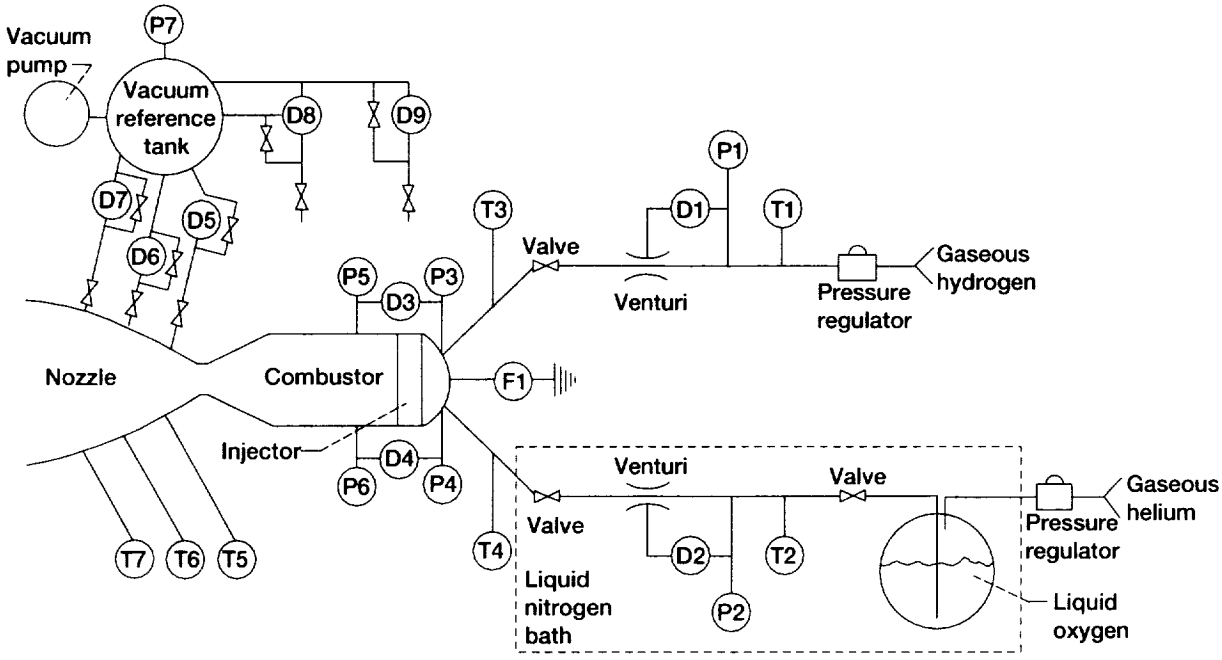

D1 Fuel venturi ΔP
D2 Oxygen venturi ΔP
D3 Fuel injection ΔP
D4 Oxygen injection ΔP
D5 Nozzle wall ΔP
D6 Nozzle wall ΔP
D7 Nozzle wall ΔP
D8 Altitude ΔP
D9 Altitude ΔP
F1 Thrust
P1 Fuel supply pressure
P2 Oxygen supply pressure
P3 Fuel injection pressure
P4 Oxygen injection pressure
P5 Chamber pressure
P6 Chamber pressure
P7 Vacuum reference pressure
T1 Fuel supply temperature
T2 Oxygen supply temperature
T3 Fuel injection temperature
T4 Oxygen injection temperature
T5 Nozzle wall temperature
T6 Nozzle wall temperature
T7 Nozzle wall temperature

Figure 3.—Schematic showing propellant circuit and instrumentation.

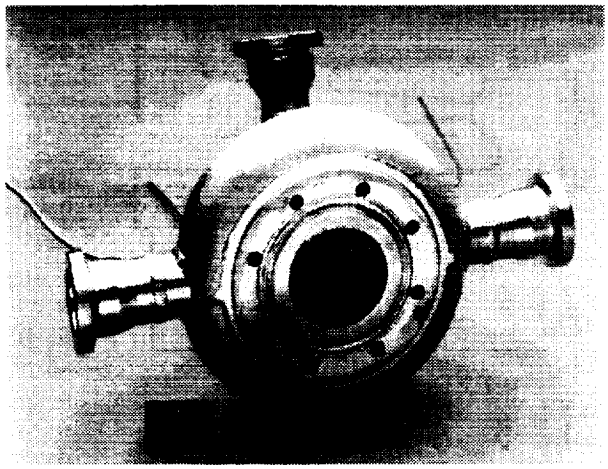

Figure 4.—Rocket engine injector.

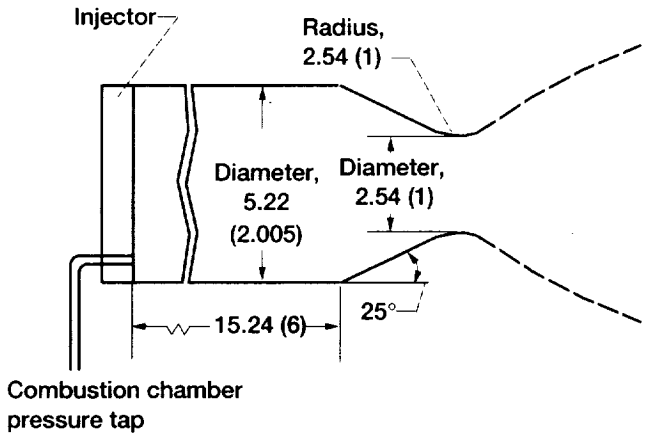

Figure 5.—Schematic of rocket combustion chamber. All dimensions in inches (centimeters).

Test Hardware

The test hardware consisted of an injector, chamber, nozzles, and boundary layer total pressure rakes. The injector (fig. 4) had a porous faceplate for gaseous hydrogen injection and 36 tubes for liquid oxygen injection. A gaseous hydrogen and gaseous oxygen torch igniter located in the center of the injector ignited the propellant mixture. As shown in figure 5, the combustion chamber was a water-cooled copper spool 15.24-cm (6-in.) long with an inside diameter of 5.22 cm (2.055 in.).

Two low-area-ratio nozzles, $\varepsilon = 10.7{:}1$ and 4:1 (fig. 6), were used to calibrate the effective combustion chamber pressure

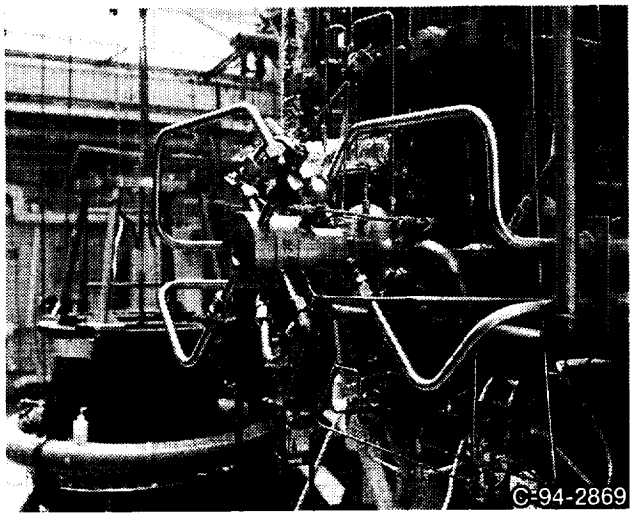

Figure 6.—Sea-level engine installed on test stand.

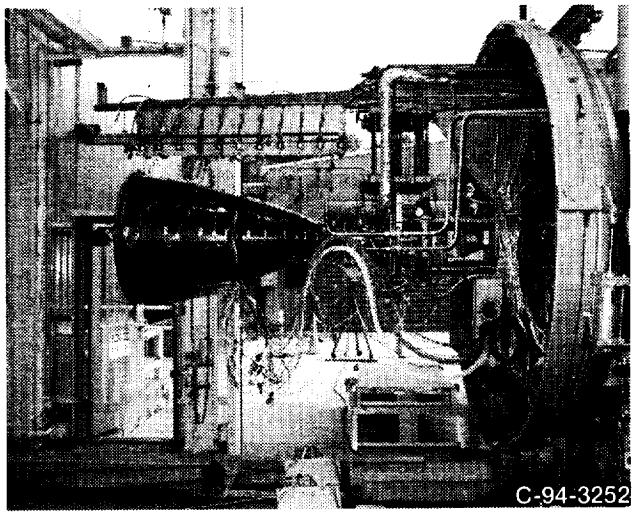

Figure 7.—High-area-ratio nozzle on test stand.

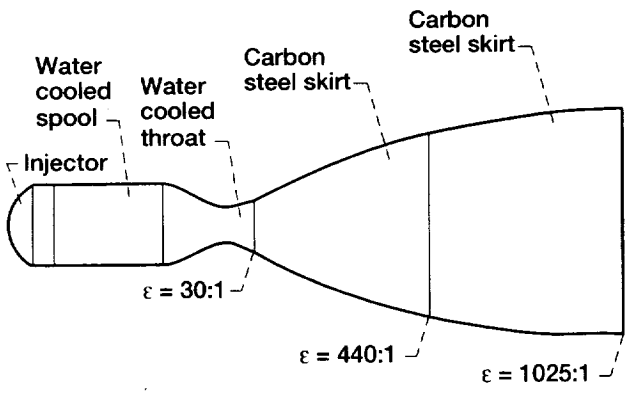

Figure 8.—Thruster assembly showing components and expansion area ratios, ε.

Axial distance from throat		Radius	
cm	in.	cm	in.
0	0	1.2700	0.5000
.3929	.1547	1.4371	.5658
.4641	.1827	1.4961	.5890
.6068	.2389	1.6190	.6374
.7503	.2954	1.7404	.6852
.8230	.3240	1.8031	.7099
1.3246	.5215	2.2426	.8829
1.7844	.7025	2.6515	1.0438
2.3777	.9361	3.1643	1.2458
3.2062	1.2623	3.8572	1.5186
7.0256	2.7660	6.6703	2.6261
7.8931	3.1075	7.2426	2.8514
9.6269	3.7901	8.3320	3.2803
10.6505	4.1931	8.9433	3.5210
11.6738	4.5960	9.5341	3.7536
12.9022	5.0796	10.2189	4.0232
15.3429	6.0405	11.5108	4.5318
16.5392	6.5115	12.1150	4.7697
19.5651	7.7028	13.5702	5.3426
23.3688	9.2003	15.2710	6.0122
25.4869	10.0342	16.1651	6.3642
29.5410	11.6303	17.7871	7.0028
33.7297	13.2794	19.3558	7.6204
36.2996	14.2912	20.2705	7.9805
38.8696	15.3030	21.1524	8.3277
41.4193	16.3068	21.9977	8.6605
47.2194	18.5903	23.8201	9.3780
51.1703	20.1458	24.9895	9.8384
55.1213	21.7013	26.1064	10.2781
60.4944	23.8167	27.5486	10.8459
71.1091	27.9957	30.1694	11.8777
76.2211	30.0083	31.3365	12.3372
90.6396	35.6849	34.3444	13.5214
105.3071	41.3532	36.9933	14.5643
113.0838	44.5212	38.3365	15.0931
128.5725	50.6191	40.6598	16.0078

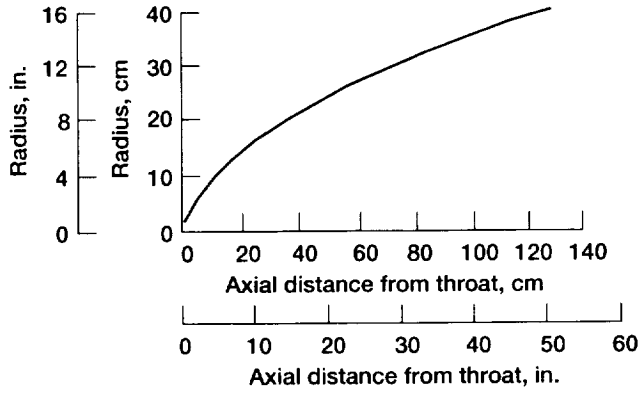

Figure 9.—Nozzle contour and coordinates.

Location	Nominal distance from nozzle wall, in.	Actual distance from nozzle wall, in.
1037:1 Area ratio nozzle		
A	0.0655	0.0655
B	.6855	.6795
C	1.3055	1.3135
D	1.9255	1.9345
E	2.5455	2.5645
F	3.1655	3.1615
G	3.7855	3.7865
440:1 Area ratio nozzle		
A	0.0900	0.0900
B	.7100	.7045
C	1.3300	1.2970
D	1.9500	1.9155
E	2.5700	2.5375
F	3.1900	3.1515
G	3.8100	3.7625

(a)

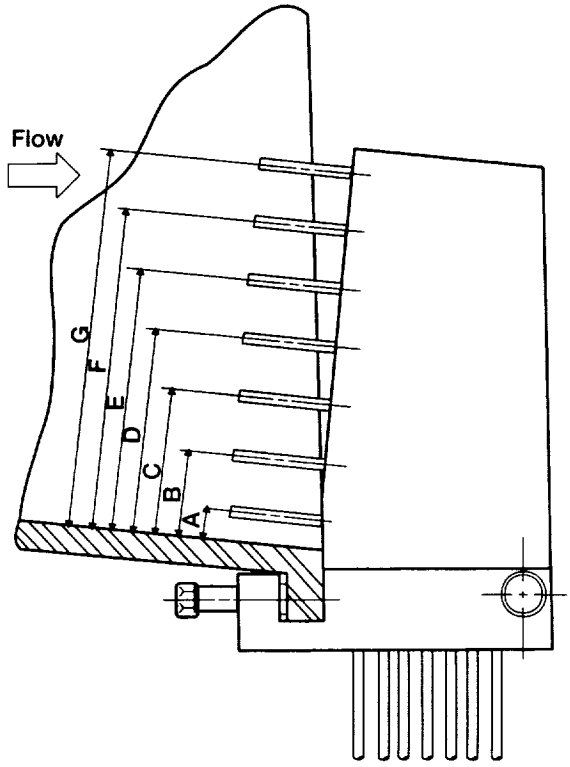

Location	Nominal distance from nozzle wall, in.	Actual distance from nozzle wall, in.
1037:1 Area ratio nozzle		
A	0.0440	0.0440
B	---	---
C	.4040	.3845
D	---	---
E	.7640	.7535
F	---	---
G	1.1240	1.1280
440:1 Area ratio nozzle		
A	0.0680	0.0680
B	---	---
C	.4280	.4195
D	---	---
E	.7880	.7455
F	---	---
G	1.1480	1.0805

(b)

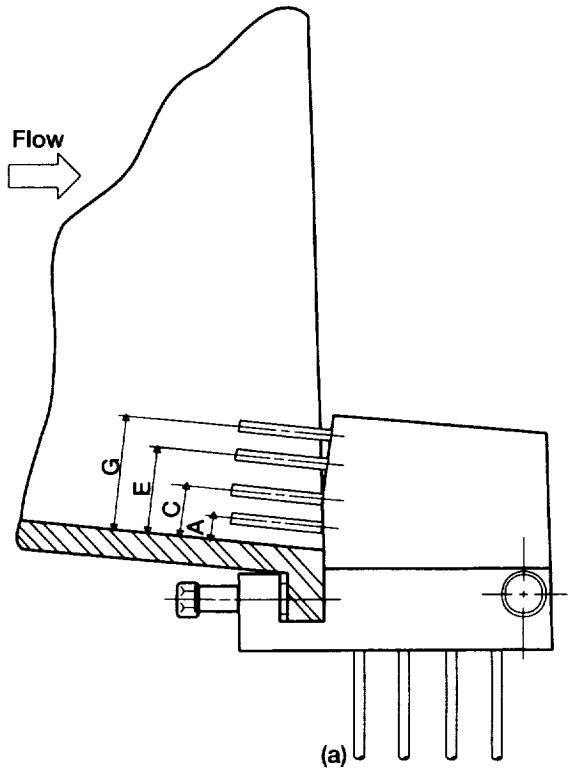

(a)

Figure 10.—Boundary layer rakes. (a) Nominally 4-in. high. (b) Nominally 1-in. high.

Location	Nominal distance from nozzle wall, in.	Actual distance from nozzle wall, in.
1037:1 Area ratio nozzle		
A	---	---
B	0.0895	0.0895
C	---	---
D	.4495	.4380
E	---	---
F	.8095	.8240
G	---	---
440:1 Area ratio nozzle		
A	---	---
B	0.2845	0.2845
C	---	---
D	.6445	.6440
E	---	---
F	1.0045	1.0125
G	---	---

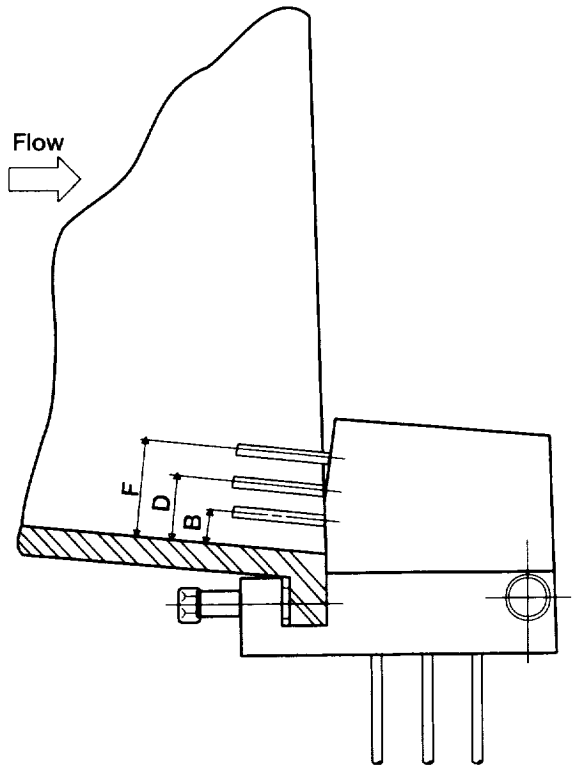

(c)

Figure 10.—Concluded. (c) Alternate nominally 1-in. high.

$P_{c,e}$ at the nozzle entrance as a function of the static pressure $P_{c,d}$ at the end of the combustion chamber. Two high-area-ratio nozzle configurations, ε = 1025:1 (fig. 7) and 440:1, were used to obtain performance data. The nozzle converging-diverging section was a water-cooled copper throat piece that started at the 5.22-cm (2.055-in.) combustion chamber inside diameter, converged to the 2.54-cm (1.0-in.) throat, and diverged to an area ratio of 30:1. At this point, a 0.635-cm- (0.25-in.-) thick carbon-steel nozzle skirt was attached that continued the contour to an expansion area ratio of 440:1. The final piece of the nozzle was a 0.635-cm- (0.25-in.-) thick carbon-steel skirt extension that concluded the contour to an area ratio of 1025:1 (fig. 8). The carbon-steel sections of the nozzle skirt, which were not actively cooled, were designed to survive the exhaust temperatures by nature of their inherent heat sink.

Contour calculations were based on the Rao nozzle optimization process (ref. 10), which uses a Rao nozzle design code (ref. 11). Figure 9 shows a plot and a table of the nozzle coordinates. A row of static pressure taps through the wall of the carbon-steel nozzle skirt measured the nozzle wall static pressures, and chromel-constantan thermocouples spot-welded to the outside surface measured the temperature of the outside wall of the carbon-steel skirts. These thermocouples were prereferenced to a 67 °C (150 °F) oven. Their specified absolute accuracy was ±1.1 K (±2 °F). Temperatures were measured at nine axial locations in a row, circumferentially displaced 45° from the static pressure tap locations.

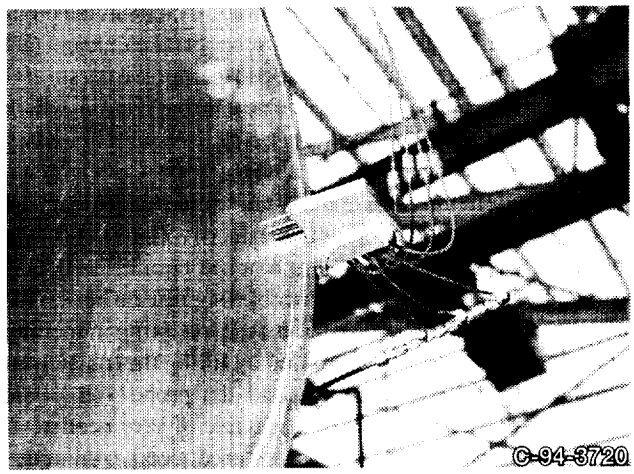

Figure 11.—Nominal 1-in. rake mounted on a nozzle.

Boundary-layer total pressure measurements were made with a series of three total pressure rakes (figs. 10(a) to (c)) that were constructed with massive copper bodies to provide conduction and a heat-sink for the main probe support structure. The individual probe tubes were made of 0.203-cm- (0.08-in.-) diameter tubing to provide adequate spatial resolution to the pressure profiles, yet they were not so fine as to have no thermal survivability. These tubes were made of a moly-rhenium alloy to provide some additional thermal survival capability. Figure 11 shows a nominal 2.54-cm (1-in.) rake mounted on a nozzle.

Procedure

Experimental Procedure

Atmospheric Testing.—Atmospheric pressure tests were first performed with the two low-area-ratio nozzles (ε = 10.7:1 and 4:1) to determine $P_{c,e}$. The firings were approximately 3 sec in duration. A steady-state condition was reached at or before 2.5 sec; this provided about 0.5 sec of steady-state operation before shutdown.

Altitude Testing.—The high-area-ratio nozzles (ε = 1025:1 and 440:1) were tested at altitude. A typical altitude firing started with the gaseous nitrogen ejectors evacuating the test capsule and spray cooler to a pressure of approximately 4.1 kPa (0.6 psia). At this pressure, the thruster was fired for about 3 sec. The pumping action during firing further reduced the pressure in the test capsule from 4.1 to approximately 1.4 kPa (0.6 to ~0.2 psia). A steady-state pressure condition was reached at, or before, 2.5 sec, again providing about 0.5 sec of steady-state operation before shutdown.

At thruster shutdown, the exhaust flow through the diffuser stopped, and a pressure pulse propagated from the spray cooler to the test capsule, raising its pressure to the original 4.1 kPa (0.6 psia). Simultaneously, the two isolation valves between the ejectors and the spray cooler were closed and the ejectors were turned off.

The high-area-ratio nozzles (1037:1 and 440:1) with the boundary layer rakes were tested at altitude exactly as the high-area-ratio (1025:1 and 440:1) nozzles without rakes, except that some operational techniques were added to improve the survivability of the rakes. The addition of a new throat section, which was required for testing at the higher area ratio with boundary layer rakes, resulted in the 1037:1 configuration. Conventional transducer installation at the end of some tubing length from the rake would require the tubing and transducer volume to fill with combustion gas until the pressure reached equilibrium. This flow into the rake would have transferred significant heat to the thin wall sections of the probe and tubing, resulting in melting or burning. Such inflow was avoided by filling the transducer, the connecting tubing, the rake, and the probe with room temperature gaseous nitrogen at a pressure of very nearly full scale on the transducer. This pressure produced a continuous outflow through the rake and probe tube that achieved three beneficial effects: (1) hot gas would not flow into the rake, (2) all the attendant hardware was cooled convectively by the outflow, and (3) the outside of the rake was shielded and/or film-cooled by spillage of the out-flow over the outside of the rake. No boundary-layer measurements could be made during the gaseous nitrogen purge. However, the rake was well protected during thruster startup and until the nozzle flow achieved steady-state conditions. Once at steady-state, the purge flow was stopped by a high-speed solenoid valve. Then, the gaseous nitrogen bled down until it was at the same pressure as the nozzle total pressure at the tip of the rake probe. This was then recorded, and the thruster was shut down. The entire duration of the shutoff gaseous nitrogen rake purge was 0.5 sec. This was sufficient to allow the transducer to get well into steady-state pressure.

Analytical Procedure

Experimental results for all the tests were compared with analytical predictions from the Liquid Propulsion Program (LPP) (June 1994) version of the TDK code. This program performs two-dimensional equilibrium, frozen, or kinetic nozzle performance calculations with boundary layer effects (ref. 2). The computational portion of TDK consists of six modules: one-dimensional equilibrium (ODE), one-dimensional kinetic (ODK), transonic flow (TRANS), method of characteristics (MOC), and two boundary layer modules (BLM and MABL). Figures 12(a) and (b) show the distribution of the modules in the nozzle along with a master flowchart of the program (ref. 12). A brief description of the modules follows. Additional information can be found in references 2, 3, and 12.

The ODE module calculates one-dimensional ideal rocket engine performance using either chemical frozen or chemical equilibrium conditions. The ODK module calculates inviscid one-dimensional equilibrium, frozen, and nonequilibrium nozzle expansion of gaseous propellant exhaust flows. The TRANS flow module calculates two-dimensional flow conditions in the transonic region of the nozzle throat. TDK uses this information to obtain an initial data line for the MOC module. The MOC module calculates the loss in nozzle performance caused by flow divergence. A finite difference mesh was constructed by tracing gas streamlines and characteristic surfaces. A separate boundary layer analysis was performed by using both the BLM and the MABL modules. As reported previously (ref. 5), the BLM module calculates compressible laminar and turbulent wall boundary layers in axisymmetric nozzles. BLM uses the Keller and Cebeci (ref. 13) two-point finite difference method to calculate the boundary layer properties and uses the Cebeci-Smith (ref. 14) eddy-viscosity formulation to model the turbulent boundary layer.

The MABL module found in TDK is a modified version of the original MABL module, which was developed in 1971 by Levine (ref. 15). Unlike BLM, MABL allows users to chose either shifting equilibrium, frozen chemistry, or finite rate kinetics to govern the boundary layer flow chemistry. In the current analysis, the code was run with finite rate kinetics for the MABL module. As with BLM, the Cebeci-Smith eddy-viscosity model is used to model the turbulent boundary layer.

Both hardware dimensions and experimental test conditions were input to the TDK code to model nozzle performance. Table I gives the geometry input for the combustion chamber section through the tangent point of the throat exit radius, and figure 9 gives the coordinates for the nozzle contour. Each point was normalized by the throat radius before being input to the program. Table II shows the experimental values input to

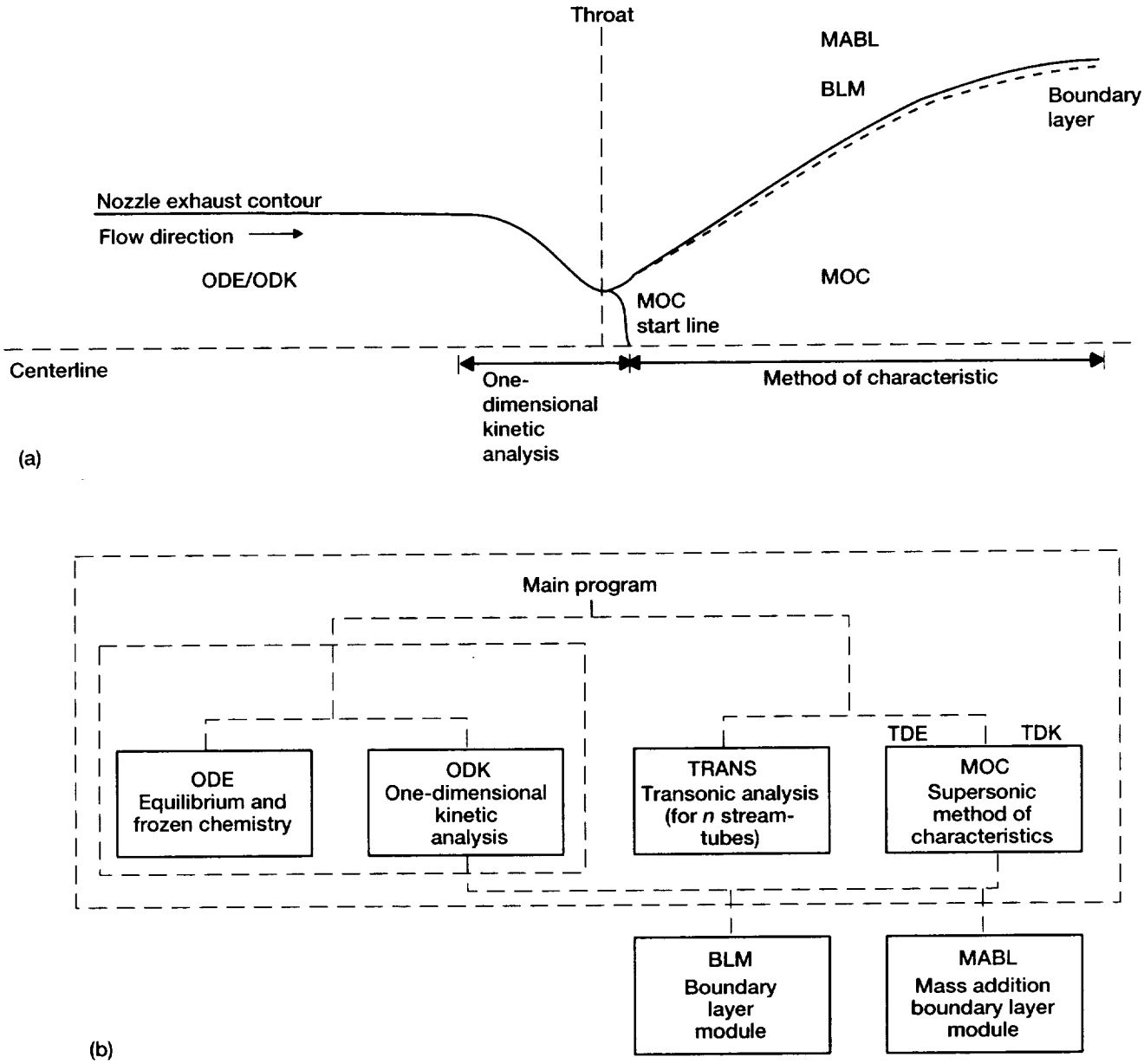

Figure 12.—TDK analysis (ref. 2). (a) Schematic. (b) Master flow chart.

TABLE I.—GEOMETRY INPUT TO TDK FOR COMBUSTION CHAMBER SECTION

Parameter	TDK variable	Expansion area ratio, ε	
		1025:01	440:1
Throat radius, cm (in.)	RSI	1.27 (0.5)	1.262 (0.497)
Inlet contraction ratio	ECRAT	4.223	4.274
Inlet wall radius[a]	RI	2	2
Inlet angle, deg	THETAI	25	25
Upstream wall radius of curvature[a]	RWTU	2	2
Downstream wall radius of curvature[a]	RWTD	0.4	0.4
Nozzle attachment angle, deg	THETA	39.41	39.41
Nozzle exit angle, deg	THE	7.94	15.5

[a]Normalized by throat radius.

TABLE II.—RESULTS OF ALTITUDE PRESSURE TESTS

Reading	Nozzle throat area, A_t		Nozzle exit expansion area ratio, ε	Measured chamber pressure				Effective chamber pressure,[a] $P_{c,e}$		Propellant mixture ratio, O/F
				At injector end, $P_{c,a}$		Corrected for momentum pressure loss, $P_{c,T}$				
	cm^2	$in.^2$		MPa	psia	MPa	psia	MPa	psia	
569	5.067	0.7854	1025	12.485	1810.8	12.448	1805.3	12.326	1787.7	3.89
570	↓	↓	↓	12.867	1866.1	12.797	1856.0	12.645	1834.0	5.97
571				12.675	1838.3	12.621	1830.4	12.488	1811.1	4.70
575				14.562	2111.9	14.502	2103.3	14.350	2081.2	4.65
576				14.850	2153.8	14.775	2142.9	14.605	2118.2	5.68
577				14.429	2092.7	14.373	2084.6	14.225	2063.1	4.47
580				16.586	2405.5	16.531	2397.5	16.364	2373.3	4.27
601	5.007	.7760	440	12.993	1884.4	12.923	1874.3	12.768	1851.8	6.15
602	5.007	.7760	440	12.740	1847.7	12.681	1839.2	12.542	1819.0	5.11
603	5.007	.7760	440	12.621	1830.4	12.581	1824.7	12.457	1806.7	4.01

[a]Calculated with low nozzle exit expansion area ratio ε correlation.

Reading	Vacuum thrust, F_V		Ambient pressure around nozzle, P_a		Characteristic exhaust velocity, C^*		Characteristic exhaust velocity efficiency, η_{C^*},
	N	lbf	kPa	psia	m/s	ft/s	percent
569	11 863	2667.1	1.491	0.2162	2476	8124	98.9
570	12 957	2913.0	1.342	.1947	2330	7643	98.6
571	12 392	2785.9	1.313	.1905	2448	8033	99.7
575	14 179	3187.7	1.470	.2132	2448	8033	99.5
576	14 904	3350.8	1.510	.2190	2372	7782	99.4
577	14 010	3149.8	1.446	.2097	2467	8094	99.8
580	16 109	3621.7	1.582	.2295	2490	8170	100.2
601	12 498	2809.7	.9143	.1326	2328	7637	99.2
602	11 923	2680.5	.7812	.1133	2416	7925	99.5
603	11 450	2574.1	.6943	.1007	2497	8192	100.0

Reading	Fuel injection				Oxidizer injection				Propellant flow rate, $\dot{m}$	
	Pressure, P_{fi}		Temperature, T_{fi}		Pressure, P_{oi}		Temperature, T_{oi}			
	MPa	psia	K	°R	MPa	psia	K	°R	kg/s	lbm/s
569	16.563	2402.2	297.1	534.8	13.509	1959.3	112.6	202.6	2.522	5.561
570	15.316	2221.3	297.1	534.8	14.393	2087.4	117.8	212.1	2.751	6.064
571	15.863	2300.7	297.3	535.1	13.967	2025.6	121.6	218.8	2.584	5.697
575	18.317	2656.6	296.3	533.3	16.138	2340.6	108.6	195.4	2.970	6.547
576	17.837	2586.9	296.8	534.2	16.778	2433.3	111.6	200.9	3.120	6.878
577	18.353	2661.8	296.8	534.3	15.998	2320.3	115.0	207.0	2.922	6.441
580	21.422	3106.9	298.9	538.1	18.521	2686.1	106.6	191.8	3.329	7.340
601	15.311	2220.6	300.7	541.3	14.480	2100.1	109.1	196.3	2.746	6.054
602	15.570	2258.2	299.5	539.1	14.011	2032.1	109.6	197.2	2.600	5.731
603	16.431	2383.1	299.3	538.8	13.707	1987.9	113.0	203.4	2.498	5.506

Reading	Measured vacuum thrust coefficient, $C_{F,V}$	Thrust coefficient efficiency, $\eta_{C_{F,V}}$, percent	Vacuum specific impulse, $I_{sp,V}$, s	Vacuum specific impulse efficiency, $\eta_{I_{sp,V}}$, percent
569	1.900	96.8	479.6	95.8
570	2.022	96.3	480.4	95.0
571	1.958	97.3	489.0	96.9
575	1.950	97.1	486.9	96.9
576	2.014	97.0	487.2	96.4
577	1.944	97.3	489.0	97.1
580	1.943	97.9	493.4	98.2
601	1.955	94.0	464.1	93.2
602	1.899	94.2	467.7	93.7
603	1.836	94.2	467.5	94.1

TABLE III.—NOZZLE INSIDE WALL TEMPERATURES

Reading	Effective combustion chamber total pressure at nozzle entrance, $P_{c,e}$		Propellant mixture ratio, O/F	Expansion area ratio, ε					
				50		50.6		100	
				Nozzle wall temperature					
	MPa	psia		K	°R	K	°R	K	°R
569	12.326	1787.7	3.89	431.55	776.79	------	------	363.59	654.47
570	12.645	1834.0	5.97	518.48	933.26	------	------	419.70	755.46
571	12.488	1811.1	4.7	491.77	885.18	------	------	407.41	733.33
575	14.350	2081.2	4.65	503.29	905.92	------	------	405.86	730.55
576	14.605	2118.2	5.68	536.22	965.19	------	------	434.23	781.62
577	14.225	2063.1	4.47	495.39	891.71	------	------	421.26	758.27
580	16.364	2373.3	4.27	520.37	936.67	------	------	418.81	753.85
601	12.768	1851.8	6.15	------	------	505.34	909.62	------	------
602	12.542	1819.0	5.11	------	------	496.83	894.30	------	------
603	12.457	1806.7	4.01	------	------	470.64	847.16	------	------

Reading	Expansion area ratio, ε									
	101.2		200		202.4		300		303.6	
	Nozzle wall temperature									
	K	°R	K	°R	K	°R	K	°R	K	°R
569	------	------	326.67	588.01	------	------	314.03	565.25	------	------
570	------	------	365.39	657.70	------	------	345.37	621.67	------	------
571	------	------	360.81	649.45	------	------	344.37	619.87	------	------
575	------	------	350.89	631.61	------	------	330.71	595.28	------	------
576	------	------	378.03	680.46	------	------	356.04	640.88	------	------
577	------	------	378.01	680.41	------	------	362.50	652.50	------	------
580	------	------	359.93	647.88	------	------	337.52	607.54	------	------
601	413.56	744.41	------	------	354.56	638.21	------	------	335.68	604.23
602	434.67	782.41	------	------	387.57	697.63	------	------	367.03	660.66
603	419.88	755.79	------	------	386.30	695.34	------	------	373.26	671.87

Reading	Expansion area ratio, ε											
	388.0		392.7		500		635		800		975	
	Nozzle wall temperature											
	K	°R	K	°R	K	°R	K	°R	K	°R	K	°R
569	312.41	562.34	------	------	306.48	551.66	309.00	556.20	310.91	559.63	308.89	556.01
570	336.46	605.63	------	------	326.89	588.40	322.96	581.32	320.07	576.13	314.78	566.60
571	337.66	607.78	------	------	329.03	592.25	327.11	588.79	326.74	588.14	323.06	581.51
575	324.82	584.67	------	------	314.52	566.14	313.56	564.40	311.21	560.17	310.17	558.31
576	347.07	624.73	------	------	335.72	604.30	329.56	593.20	325.63	586.14	320.85	577.53
577	356.27	641.28	------	------	344.16	619.48	340.23	612.42	337.56	607.61	334.11	601.39
580	329.67	593.41	------	------	319.46	575.02	317.65	571.77	314.06	565.31	313.92	565.06
601	------	------	331.71	597.08	------	------	------	------	------	------	------	------
602	------	------	360.11	648.20	------	------	------	------	------	------	------	------
603	------	------	370.24	666.44	------	------	------	------	------	------	------	------

TDK: effective chamber pressure, mixture ratio, fuel injection temperature, and oxidizer injection temperature. The propellant injection temperatures were used to determine the propellant enthalpies. Since the fuel was gaseous hydrogen, the TDK code used the enthalpy that was based on the input temperature. The GASPLUS code (ref. 16) was used to determine the enthalpy for liquid oxygen on the basis of the experimentally determined inlet pressure and temperature to the injector. Because GASPLUS has a different reference state than TDK, the enthalpy values were corrected for this.

The experimentally determined outside wall temperatures and their time rate of change were used to calculate the inside nozzle wall temperatures according to the method described in reference 5. These calculated temperatures were then used as nozzle input (table III). Conditions on the water-cooled combustion chamber wall from the injector face through the throat plane were not available and had to be estimated. For the purpose of this analysis, wall temperatures were distributed between 700 and 844.4 K (1260 and 1520 °R) in this region. This temperature range was selected on the basis of previous combustion chamber testing data (refs. 17 and 18). Sensitivity of the TDK code results to variations in combustor wall temperatures was negligible, especially in comparison to the effects of chamber pressure and mixture ratio on the final results.

The TDK code requires that the boundary layer be set to either laminar, turbulent, or transitional flow at either a specific nozzle location or at a specific Reynolds number based on the momentum thickness Re_θ. When $Re_\theta = 400$, the boundary layer transitions to turbulent flow (ref. 5). Although it was assumed that the boundary layer was turbulent, both TDK/BLM and TDK/MABL were run in transition with $Re_\theta = 400$ to allow the code to estimate the exact transition point. In all cases, the code indicated that transition occurred near the injector face in the combustion chamber; therefore, the program results were based on a fully turbulent boundary layer. As a point of comparison, but of no physical significance, the code was also run with a laminar boundary layer assumption. These results are reported in appendix B.

The analytically predicted total pressures in the rakes were obtained from the LPP version of the TDK code using a pitot probe subroutine. This subroutine provides total flow conditions to simulate the placement of a pitot probe into the flow field at specified radial locations.

Experimental Data Analysis

Performance

Propellant Mass Flow.—Propellant mass flows were measured with calibrated venturis. Each mass flow was calculated from conditions at the venturi throat by

$$\dot{m} = C_d \rho A_v V \tag{1}$$

where C_d is the venturi discharge coefficient, ρ is the throat density, A_v is the venturi throat area, and V is the velocity; ρ and V were calculated from one-dimensional mass and energy equations; and real fluid properties were obtained from the fluid properties program GASP (ref. 19). Venturi calibrations of C_d were performed by the Colorado Engineering Experiment Station. Values of the discharge coefficient were traceable NIST, and the uncertainty values were ±0.5 percent of full scale.

Vacuum Thrust.—The vacuum thrust was determined by measuring the thrust produced at the test capsule ambient pressure P_a and by applying two corrections. The first correction compensated for the thrust-stand zero shift that occurred from the change in capsule pressure during thruster startup. This correction, referred to as an aneroid correction, is explained in reference 4. The second correction adjusted the thrust measured at a P_a of approximately 1.4 kPa (0.2 psia) to the thrust that would have been measured if P_a had been an absolute vacuum. This thrust was calculated by adding the force induced by the capsule pressure on the nozzle exit area to the measured thrust:

$$F_V = F + \left(P_a \times A_{ex}\right) \tag{2}$$

where F is the aneroid-corrected thrust and A_{ex} is the nozzle exit area.

Effective Chamber Pressure.—For the effective combustion chamber total pressure at the nozzle entrance $P_{c,e}$ to be truly representative, a thorough survey of the distribution of pressures in the combustion chamber would have had to have been made by taking readings from several static pressure taps in the combustion chamber. Then, these measurements would have had to have been integrated and averaged to obtain an integrated mean pressure that could be corrected for momentum pressure loss and used as $P_{c,e}$. In an alternative method that was used for the present study, $P_{c,e}$ was determined by the following equation:

$$P_{c,e} = P_{c,a}\left(\frac{P_{c,T}}{P_{c,a}}\right)\left(\frac{P_{c,e}}{P_{c,T}}\right) \tag{3}$$

where $P_{c,a}$ is the chamber pressure measured at a single injector faceplate position, $P_{c,T}/P_{c,a}$ is the conversion of the chamber static pressure before combustion to total pressure after combustion (momentum pressure loss), and $P_{c,e}/P_{c,T}$ is the correction that accounts for any variations in pressure distribution across the injector face. The momentum pressure loss was calculated by the following equation from reference 20:

$$\frac{P_{c,T}}{P_{c,a}} = \left(\frac{P_s}{P_T} + \frac{Ig_c - V_{av}}{C^*_{Th(ODE)}\,\varepsilon_c}\right)^{-1} \tag{4}$$

where P_s/P_T is the static-to-total pressure ratio in the combustion chamber; I is the theoretical subsonic specific impulse inside the combustion chamber; g_c is the proportionality constant; V_{av} is the propellant mass-averaged injection velocity; $C^*_{Th(ODE)}$ is the theoretical characteristic exhaust velocity, and ε_c is the thruster contraction area ratio. The ratio $P_{c,e}/P_{c,T}$ was derived semi-empirically by the following procedure. A series of low-area-ratio nozzle tests (ε = 10:7 and 4:1) were performed to develop a correlation between single-point chamber pressure measurements corrected for momentum pressure loss and the effective chamber pressure. These two pressures are defined at the same axial location in the chamber and vary only in that $P_{c,T}$ defines a single point and $P_{c,e}$ defines an average pressure at that axial location. This procedure is a calibration of the injector and chamber pressure tap. In these tests, the contour of the combustion chamber up to the throat was identical to that used in the test of the high-area-ratio nozzles.

The contour downstream of the throat was identical to that of a low-area-ratio divergent nozzle with a thrust coefficient calculated by an iterative procedure using the TDK program. The calculated thrust coefficient obtained from TDK was used with the experimental measurements of thrust from the low-area-ratio tests and with the $P_{c,e}$ calculated by the following equation:

$$P_{C,e} = \frac{F_V}{C_{F,V,Th(TDK)} A_t} \tag{5}$$

where $C_{F,V,Th(TDK)}$ is the theoretical, two-dimensional-kinetics, vacuum thrust coefficient and A_t is the nozzle throat area. Next, the values of $P_{C,e}$ were related to the calculated total pressure after combustion $P_{C,T}$, and a correlation was developed. This correlation, $P_{C,e}/P_{C,T}$, which was plotted versus the propellant mixture ratio O/F, represents the correction for nonuniform pressure distributions (fig. 13). A straight line was fit to the data with a least-squares best fit, and the equation of this line was used as the correlation.

Equation (3) is valid because the same injector and chamber contour were used in both the low-area-ratio and high-area-ratio tests. The chamber static pressure was measured at the injector face static tap to obtain $P_{C,a}$, and the momentum pressure loss conversion (eq. (4)) provided $P_{C,T}/P_{C,a}$. The semi-empirical correlation $P_{C,e}/P_{C,T}$ versus O/F from the low-area-ratio nozzle tests provided the $P_{C,e}/P_{C,T}$ correlation.

Performance Calculations.—By definition,

$$C^* = \frac{P_{C,e} A_t g_c}{\dot{m}} \tag{6}$$

$$C_{F,V} = \frac{F_V}{P_{C,e} A_t} \tag{7}$$

$$I_{sp,V} = \frac{F_V g_c}{\dot{m} g} \tag{8}$$

The values of $P_{C,e}$, mass flow, and vacuum thrust were calculated as described in the preceding section. The throat diameter was measured each test day to ensure that no distortion or eroding was occurring. None was observed, and an average value was used to calculate the throat area (tables I and II; one value for each throat section used).

Efficiency Calculations.—The performance parameters ($I_{sp,V}$, $C_{F,V}$, C^*) were divided by the theoretical, one-dimensional-equilibrium (ODE) values obtained from the Chemical Equilibrium Composition (CEC) program (ref. 21) to derive the efficiencies. The inlet enthalpy conditions were derived from measurements of the injection pressure and temperature of the hydrogen and oxygen. Equations for the various efficiencies follow. The characteristic exhaust velocity efficiency is

$$\eta_{C^*} = \frac{C^*}{C^*_{Th(ODE)}} \tag{9}$$

the vacuum thrust coefficient efficiency is

$$\eta_{C_{F,V}} = \frac{C_{F,V}}{C_{F,V,Th(ODE)}} \tag{10}$$

and the vacuum specific impulse efficiency is

$$\eta_{I_{sp,V}} = \frac{I_{sp,V}}{I_{sp,V,Th(ODE)}} \tag{11}$$

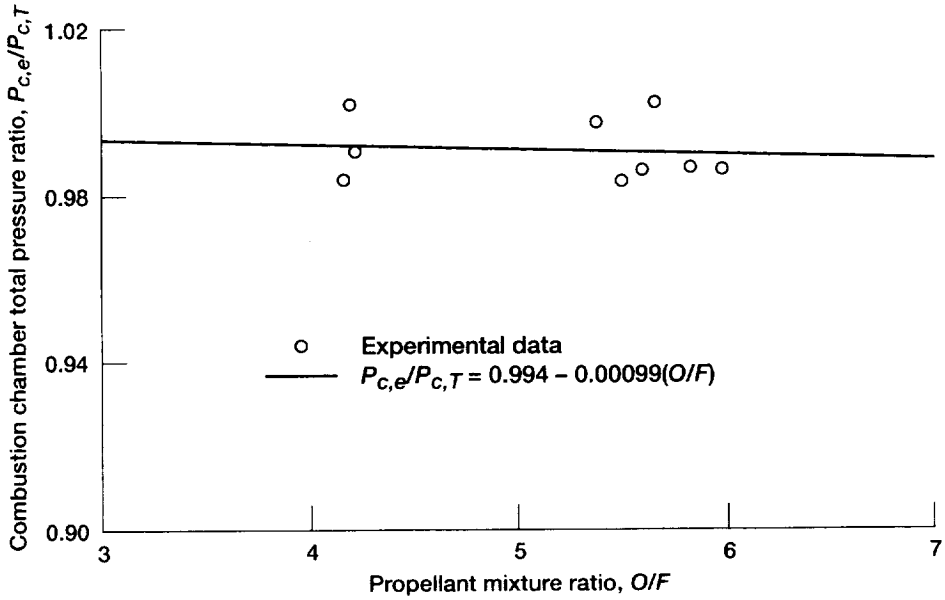

Figure 13.—Effective chamber pressure correlation.

Heat Transfer

Seven test firings were for experimental determinations of the attainable thrust performance of high-area-ratio rocket nozzles. During these firings, the outer wall temperatures of the carbon-steel, heat-sink nozzle skirt were measured. From these measurements, the heat fluxes were calculated.

The technique of calculating heat flux from the wall temperature data of a heat-sink nozzle was first employed in reference 5. This technique, which is very simple in principle, resulted from observations that the nozzle wall temperature time histories were linear once the rocket thruster achieved steady-state thrust. The slope of the time response of the temperature was directly proportional to the heat flux to the wall. A detailed derivation of this principle is presented in appendix A of reference 5. Further analysis showed that axial conduction and radiation losses were the primary heat losses that would cause errors in the heat flux determination. In general, these were less than 2 percent in the area considered. This error analysis is detailed in appendix B of reference 5.

During performance testing of the 1025:1 nozzle, thermocouple measurements were taken at a rate of 50 Hz, averaged in groups of five, and displayed at 0.1-sec intervals. Table IV lists the temperatures taken just prior to thruster shutdown. At this point, the thruster was at steady state with regard to the static pressure measurements in the nozzle. Measurements were taken at nine axial locations, which are identified in the table by the area ratio at the location. Also listed are the combustion conditions of the thruster for each of the firings.

TABLE IV.—NOZZLE OUTSIDE WALL TEMPERATURES

Reading	Effective combustion chamber total pressure at nozzle entrance, $P_{c,e}$		Propellant mixture ratio, O/F	Expansion area ratio, ε					
				50		50.6		100	
				Nozzle wall temperature					
	MPa	psi		K	°R	K	°R	K	°R
569	12.326	1787.7	3.89	361.69	651.05	---------	---------	325.56	586.00
570	12.645	1834.0	5.97	428.94	772.09	---------	---------	370.09	666.17
571	12.488	1811.1	4.70	411.62	740.91	---------	---------	363.23	653.82
575	14.350	2081.2	4.65	414.72	746.50	---------	---------	356.46	641.63
576	14.605	2118.2	5.68	438.81	789.86	---------	---------	379.98	683.96
577	14.225	2063.1	4.47	416.22	749.20	---------	---------	375.08	675.15
580	16.364	2373.3	4.27	429.66	773.38	---------	---------	366.32	659.37
601	12.768	1851.8	6.15	---------	---------	416.91	750.44	---------	---------
602	12.542	1819.0	5.11	---------	---------	421.42	758.56	---------	---------
603	12.457	1806.7	4.01	---------	---------	406.07	730.93	---------	---------

Reading	Expansion area ratio, ε									
	101.2		200		202.4		300		303.6	
	Nozzle wall temperature									
	K	°R	K	°R	K	°R	K	°R	K	°R
569	---------	---------	306.32	551.38	---------	---------	299.35	538.83	---------	---------
570	---------	---------	339.28	610.71	---------	---------	327.02	588.63	---------	---------
571	---------	---------	337.71	607.88	---------	---------	327.87	590.16	---------	---------
575	---------	---------	324.02	583.23	---------	---------	311.82	561.27	---------	---------
576	---------	---------	348.91	628.03	---------	---------	335.87	604.57	---------	---------
577	---------	---------	353.87	636.96	---------	---------	345.15	621.27	---------	---------
580	---------	---------	330.98	595.76	---------	---------	317.27	571.08	---------	---------
601	365.07	657.13	---------	---------	328.47	581.25	---------	---------	317.13	570.84
602	391.28	704.31	---------	---------	365.24	657.44	---------	---------	350.88	631.58
603	382.32	688.18	---------	---------	367.27	661.08	---------	---------	358.88	645.99

Reading	Expansion area ratio, ε											
	388		392.7		500		635		800		975	
	Nozzle wall temperature											
	K	°R	K	°R	K	°R	K	°R	K	°R	K	°R
569	300.61	541.09	---------	---------	297.56	535.61	301.44	542.60	303.82	546.88	302.86	545.14
570	322.01	579.61	---------	---------	316.16	569.09	314.66	566.38	313.57	564.42	309.35	556.83
571	324.53	584.16	---------	---------	319.16	574.49	319.45	575.01	320.53	576.95	317.96	572.32
575	309.96	557.92	---------	---------	303.44	546.20	304.79	548.62	304.29	547.73	304.32	547.77
576	331.11	595.99	---------	---------	323.84	582.92	320.29	576.52	318.52	573.34	314.78	566.61
577	342.49	616.49	---------	---------	333.86	600.95	332.06	597.70	330.83	595.50	328.28	590.90
580	313.56	564.40	---------	---------	307.35	553.23	308.32	554.98	306.74	552.13	307.64	553.75
601	---------	---------	316.88	570.38	---------	---------	---------	---------	---------	---------	---------	---------
602	---------	---------	347.11	624.80	---------	---------	---------	---------	---------	---------	---------	---------
603	---------	---------	358.74	645.74	---------	---------	---------	---------	---------	---------	---------	---------

TABLE V.—EXPERIMENTALLY MEASURED RATES OF INCREASE IN NOZZLE TEMPERATURE

Reading	Effective combustion chamber total pressure at nozzle entrance, $P_{c,e}$		Propellant mixture ratio, O/F	Expansion area ratio, ε					
				50		100		200	
				Measured rate of increase in nozzle temperature					
	MPa	psia		K/s	°R/s	K/s	°R/s	K/s	°R/s
569	12.326	1787.7	3.89	63.67	114.60	34.89	62.81	18.76	33.76
570	12.645	1834.0	5.97	81.61	146.89	45.51	81.91	24.06	43.31
571	12.488	1811.1	4.70	73.04	131.48	40.52	72.94	21.29	38.32
575	14.350	2081.2	4.65	80.72	145.29	45.32	81.57	24.77	44.59
576	14.605	2118.2	5.68	88.77	159.79	49.77	89.59	26.85	48.33
577	14.225	2063.1	4.47	72.16	129.88	42.36	76.25	22.25	40.05
580	16.364	2373.3	4.27	82.68	148.82	48.15	86.67	26.69	48.04

Reading	Expansion area ratio, ε											
	300		388		500		635		800		975	
	Measured rate of increase in nozzle temperature											
	K/s	°R/s	K/s	°R/s	K/s	°R/s	K/s	°R/s	K/s	°R/s	K/s	°R/s
569	13.56	24.40	10.92	19.65	8.26	14.86	7.00	12.60	6.57	11.82	5.60	10.08
570	16.89	30.40	13.37	24.06	9.93	17.87	7.69	13.84	6.03	10.86	5.03	9.06
571	15.24	27.44	12.13	21.84	9.13	16.44	7.09	12.77	5.76	10.37	4.73	8.52
575	17.45	31.41	13.74	24.74	10.26	18.46	8.12	14.62	6.41	11.53	5.43	9.78
576	18.63	33.54	14.77	26.58	10.99	19.79	8.58	15.45	6.59	11.87	5.63	10.13
577	16.03	28.85	12.73	22.92	9.53	17.15	7.58	13.64	6.24	11.23	5.41	9.73
580	18.71	33.68	14.91	26.83	11.21	20.17	8.64	15.55	6.79	12.22	5.83	10.49

The time rate of change of the nozzle wall temperature measurements was also noted. For every thermocouple, the rate of change for any thermocouple was constant during the last second of firing. These measurements are tabulated in table V, which shows the rate of temperature increases $\partial T/\partial t$, for all nine locations for each of seven firings. From these values of $\partial T/\partial t$, we could calculate the temperature of the inside wall:

$$T_i = T_o - \frac{R_o^2 \partial T}{4\alpha \partial t}\left[1 - \left(\frac{R_i}{R_o}\right)^2 - \ln\left(\frac{R_i}{R_o}\right)\right] \tag{12}$$

Equation (12) is derived in reference 5. Values for T_o were obtained from table IV, and values for $\partial T/\partial t$ were obtained from table V. Calculated inside wall temperatures are presented in table III. The heat fluxes to the wall of the nozzle were also calculated:

$$q'' = \frac{kR_i}{2a}\frac{\partial T}{\partial t}\left[\left(\frac{R_o}{R_i}\right)^2 - 1\right] \tag{13}$$

Equation (13) is also derived in reference 5. Calculated nozzle wall heat fluxes are tabulated in table VI.

The heat rate Q to the walls of a rocket nozzle between two axial locations can be determined by integrating the heat flux values with respect to the nozzle surface area. Details of this derivation are in reference 5:

$$Q = \int_{L_1}^{L_2} q'' \partial A_s = \int_{L_1}^{L_2}\left(\frac{q'' \pi D_i}{\cos\theta}\right) \tag{14}$$

Calculated total heat rates for the seven firings are tabulated in table VII.

Boundary Layer

Two different instrumentation configurations were used to obtain total pressure measurements in the 12 firings reported herein. The first was with a single, nominally 4-in. high, boundary-layer rake (fig. 10(a)) with seven total pressure probes. The other was with two small rakes (figs. 10(b) and (c)), nominally 1-in. high with three and four total pressure probes, respectively. The rakes were mounted at the exit of the nozzle, with the two short rakes mounted 180° apart. This arrangement allowed total pressure measurements to be obtained at 14 different distances from the nozzle wall. The rakes were installed with the probe tubes inserted into the exit of the nozzle, with the probe tubes parallel to the nozzle wall. Because of the nozzle wall divergence, the body of the rake was not radial, but perpendicular, to the wall. As a result, the individual probes were each located at a slightly different axial dimension, and hence, at a slightly different expansion area ratio (see figs. 10(a) to (c)).

The boundary layer rake data were not manipulated, except for the total pressure measurements, which were normalized by the effective chamber pressure.

TABLE VI.—EXPERIMENTALLY DETERMINED NOZZLE HEAT FLUX DISTRIBUTION

Reading	Effective combustion chamber total pressure at nozzle entrance, $P_{c,e}$		Propellant mixture ratio, O/F	Characteristic exhaust velocity efficiency, (best fit curve) η_{c^*}, percent	Expansion area ratio, ε			
					50		100	
					Heat flux to nozzle walls, as measured			
	MPa	psia			kW/m^2	$Btu/in.^2$-sec	kW/m^2	$Btu/in.^2$-sec
569	12.326	1787.7	3.89	99.82	1422.77	0.8706	772.02	0.4724
570	12.645	1834.0	5.97	99.07	1823.66	1.1159	1006.70	.6160
571	12.488	1811.1	4.70	99.65	1632.29	.9988	896.55	.5486
575	14.350	2081.2	4.65	99.67	1803.88	1.1038	1002.61	.6135
576	14.605	2118.2	5.68	99.26	1983.81	1.2139	1101.16	.6738
577	14.225	2063.1	4.47	99.72	1612.51	.9867	937.24	.5735
580	16.364	2373.3	4.27	99.76	1847.68	1.1306	1065.20	.6518

Reading	Expansion area ratio, ε							
	200		300		388		500	
	Heat flux to nozzle walls, as measured							
	kW/m^2	$Btu/in.^2$-sec	kW/m^2	$Btu/in.^2$-sec	kW/m^2	$Btu/in.^2$-sec	kW/m^2	$Btu/in.^2$-sec
569	411.99	0.2521	296.78	0.1816	238.60	0.1460	180.26	0.1103
570	528.52	.3234	371.30	.2272	292.20	.1788	216.70	.1326
571	467.56	.2861	333.71	.2042	265.24	.1623	199.38	.1220
575	544.20	.3330	382.09	.2338	300.37	.1838	223.89	.1370
576	589.80	.3609	408.07	.2497	322.76	.1975	239.91	.1468
577	488.80	.2991	350.87	.2147	278.31	.1703	207.88	.1272
580	586.20	.3587	409.71	.2507	325.87	.1994	244.65	.1497

Reading	Expansion area ratio, ε					
	635		800		975	
	Heat flux to nozzle walls, as measured					
	kW/m^2	$Btu/in.^2$-sec	kW/m^2	$Btu/in.^2$-sec	kW/m^2	$Btu/in.^2$-sec
569	152.64	0.0934	143.00	0.0875	121.91	0.0746
570	167.67	.1026	131.39	.0804	109.49	.0670
571	154.60	.0946	125.51	.0768	102.96	.0630
575	176.99	.1083	139.40	.0853	118.16	.0723
576	187.12	.1145	143.65	.0879	122.41	.0749
577	165.22	.1011	135.81	.0831	117.67	.0720
580	188.27	.1152	147.90	.0905	126.82	.0776

TABLE VII.—TOTAL HEAT RATE VALUES ADJUSTED TO A COMMON $P_{c,e}$

Reading	Effective combustion chamber total pressure at nozzle entrance, $P_{c,e}$		Propellant mixture ratio, O/F	Heat rate from ε = 140 to 1025							
				Experimental							
				No adjustments		Adjusted to $P_{c,e}$ = 2063.1 psia		Adjusted to η_{C^*} =100 percent		Adjusted to η_{C^*} = 100 percent and $P_{c,e}$ = 2063.1 psia	
	MPa	psia		kW	Btu/s	kW	Btu/s	kW	Btu/s	kW	Btu/s
569	12.326	1787.7	3.89	380.43	360.67	426.63	404.47	381.81	361.97	428.17	405.93
570	12.645	1834.0	5.97	425.68	403.56	467.71	443.41	433.71	411.18	476.54	451.78
571	12.488	1811.1	4.70	390.23	369.96	433.10	410.60	392.98	372.56	436.15	413.49
575	14.350	2081.2	4.65	443.65	420.60	440.56	417.67	446.59	423.39	443.48	420.44
576	14.605	2118.2	5.68	471.11	446.63	461.27	437.31	478.15	453.31	468.17	443.85
577	14.225	2063.1	4.47	416.83	395.17	416.83	395.17	419.17	397.39	419.17	397.39
580	16.364	2373.3	4.27	476.84	452.07	426.30	404.15	479.14	454.25	428.35	406.10

Reading	Heat rate from ε = 140 to 1025			
	TDK/MABL turbulent			
	Adjusted to η_{C^*} =100 percent		Adjusted to η_{C^*} =100 percent and $P_{c,e}$ = 2063.1 psia	
	kW	Btu/s	kW	Btu/s
569	520.36	493.33	583.57	553.25
570	617.50	585.42	678.48	643.23
571	559.67	530.59	621.14	588.87
575	626.02	593.50	621.66	589.36
576	681.88	646.45	667.65	632.96
577	608.06	576.47	608.06	576.47
580	675.04	639.97	603.48	572.13

Results

Performance Results

Atmospheric Pressure Tests.—Tests were performed at atmospheric pressure to determine the relationship between the effective and measured chamber pressures of the thruster. The tests were conducted with low-area-ratio configurations (ε = 10.7:1 and 4:1), the performance of which is well documented and agrees with calculated values from the TDK program. Because of the low-area-ratio of the nozzles, an altitude condition was not necessary to obtain full, unseparated nozzle flow. The results of the nine successful atmospheric tests are summarized in table VIII. In this table, the measured combustion chamber static pressure at the injector face is listed as $P_{c,a}$, and equation (4) was used to derive the $P_{c,T}$ values from the $P_{c,a}$ values. The effective chamber pressures $P_{c,e}$, derived from thrust measurements as previously described, are also listed in table VIII. A consistent variation between $P_{c,e}$ and $P_{c,T}$ was observed and was attributed to variations in the static pressure profile that most likely occurred at the static tap used for the $P_{c,a}$ measurements.

So that the decrease in thrust attributable to combustion losses could be properly accounted for, the characteristic exhaust velocity C^* and the characteristic exhaust velocity efficiency η_{C^*} were derived for both the atmospheric and altitude tests. Within the range of these tests, chamber pressure had no effect on η_{C^*} and only a slight variation with respect to O/F. Figure 14 shows η_{C^*} as a function of O/F for all atmospheric and altitude firings. A mean value of η_{C^*} was described by a second-order polynomial curve fit (eq. (15)) by the least-squares method, with values ranging from approximately 99.0 to 99.9 percent.

$$\eta_{C^*} = 98.43 + 0.824(O/F) - 0.120(O/F)^2 \qquad (15)$$

Altitude Tests.—High-area-ratio nozzle tests were performed at altitude conditions to avoid separated flow in the divergent portion of the nozzle. The first test objective was to ascertain whether the flow was attached or separated by examining the nozzle wall static pressure distribution. Static pressures, which were measured at eight axial locations, are given in table IX. Figure 15 shows a typical distribution along the length of the nozzle. Plotted there from reading 577 are the static pressure ratios $P_s/P_{c,e}$ versus the nozzle expansion ratio of the pressure tap locations. When plotted on log-log coordinates, the result is a straight line. If the flow were separated, the pressure distribution would display a sudden increase. As this was not the case for any of the tests, all the data reported have attached flow.

TABLE VIII.—RESULTS OF ATMOSPHERIC PRESSURE TESTS

Reading	Expansion area ratio, ε	Nozzle throat area, A_t		Measured chamber pressure				Propellant mixture ratio, O/F	Measured thrust, F	
				At injector face, $P_{c,A}$		Corrected for momentum pressure loss, $P_{c,T}$				
		cm^2	$in.^2$	MPa	psia	MPa	psia		N	lb_f
514	10.72	5.103	0.7909	13.942	2022.1	13.893	2014.9	4.21	11 209	2520.0
515	10.72	5.103	.7909	15.801	2291.7	15.748	2284.0	4.16	12 677	2850.1
523	3.99	5.091	.7890	12.254	1777.3	12.211	1771.0	4.19	9 491	2133.7
524	3.99	5.091	.7890	12.524	1816.4	12.461	1807.3	5.38	9 735	2188.6
526	4.02	5.047	.7823	14.362	2083.0	14.293	2072.9	5.66	11 174	2512.2
527	↓	↓	↓	14.746	2138.7	14.675	2128.4	5.60	11 285	2537.1
528				15.096	2189.4	15.023	2178.8	5.50	11 511	2587.8
529				12.825	1860.1	12.756	1850.1	5.83	9 808	2205.0
530				14.642	2123.6	14.564	2112.3	5.98	11 423	2568.2

Reading	Vacuum thrust,[a] F_V		Propellant flow rate, $\dot{m}$		Fuel injection pressure, P_{fi}		Fuel injection temperature, T_{fi}		Oxidizer injection pressure, P_{oi}	
	N	lb_f	kg/s	lb_m/s	MPa	psia	K	°R	MPa	psia
514	11 746	2640.7	2.852	6.287	17.818	2584.2	294.9	530.8	15.271	2214.8
515	13 214	2970.8	3.158	6.962	20.030	2905.0	294.7	530.4	17.411	2525.1
523	9 690	2178.5	2.500	5.512	16.147	2341.9	308.5	555.3	13.399	1943.3
524	9 934	2233.3	2.644	5.828	15.389	2231.9	306.5	551.7	13.891	2014.6
526	11 374	2557.0	3.037	6.696	17.508	2539.3	309.3	556.7	16.326	2367.8
527	11 486	2582.2	3.102	6.839	17.915	2598.3	300.8	541.5	16.791	2435.3
528	11 711	2632.8	3.143	6.928	18.258	2648.0	299.1	538.4	17.036	2470.8
529	10 008	2250.0	2.707	5.968	15.341	2224.9	299.8	539.6	14.329	2078.2
530	11 424	2568.3	3.082	6.794	17.420	2526.4	300.9	541.7	16.602	2407.8

Reading	Oxidizer injection temperature, T_{oi}		Theoretically predicted			Effective chamber total pressure calculated from thrust, $P_{c,e}$		Correlation pressure ratio for use in altitude tests, $P_{c,e}/P_{c,T}$	Characteristic exhaust velocity efficiency, η_{C^*}, percent
			ODE vacuum thrust coefficient, $C_{F,V,Th}$ (ODE)	TDK vacuum thrust coefficient, $C_{F,V,Th}$ (TDK)	Vacuum thrust coefficient efficiency, TDK/ODE, $\eta_{C_{F,V}}$				
	K	°R				MPa	psia		
514	90.9	163.6	1.737	1.673	96.3	13.758	1995.4	0.990	99.1
515	88.8	159.9	1.736	1.673	96.4	15.483	2245.5	.983	100.6
523	96.7	174.1	1.601	1.557	97.2	12.230	1773.8	1.002	100.2
524	92.9	167.3	1.615	1.570	97.2	12.433	1803.2	.998	99.5
526	110.2	198.3	1.619	1.573	97.2	14.327	2077.9	1.002	99.8
527	110.2	198.4	1.619	1.572	97.1	14.476	2099.5	.986	98.5
528	92.3	166.2	1.617	1.571	97.2	14.769	2142.0	.983	98.9
529	92.8	167.0	1.622	1.576	97.2	12.585	1825.3	.987	99.0
530	93.1	167.6	1.623	1.576	97.1	14.365	2083.3	.986	99.6

Reading	Vacuum specific impulse $I_{sp,V}$, s	Vacuum specific impulse efficiency, $\eta_{I_{sp,V}}$, percent	Ambient pressure around nozzle, P_a	
			kPa	psia
514	420.0	95.5	98.143	14.234
515	426.7	96.9	98.109	14.229
523	395.2	97.4	↓	↓
524	383.2	96.7		
526	381.9	96.9		
527	377.6	95.7	98.854	14.337
528	380.0	96.0	98.819	14.332
529	377.0	96.2	98.785	14.327
530	378.0	96.8	98.681	14.312

[a]Measured thrust corrected to vacuum conditions.

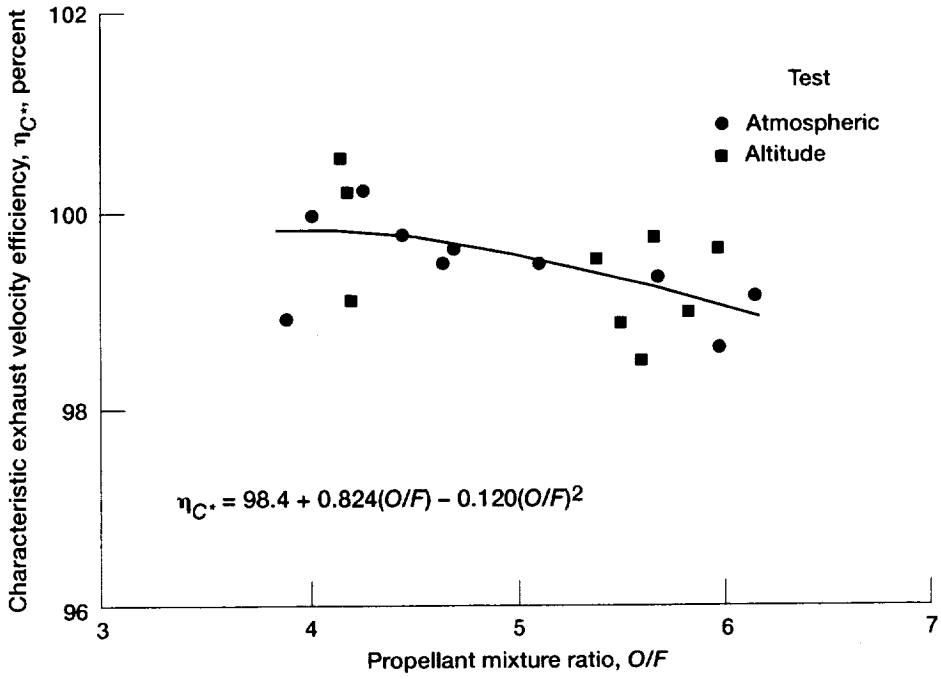

Figure 14.—Characteristic exhaust velocity efficiency as function of propellant mixture ratio.

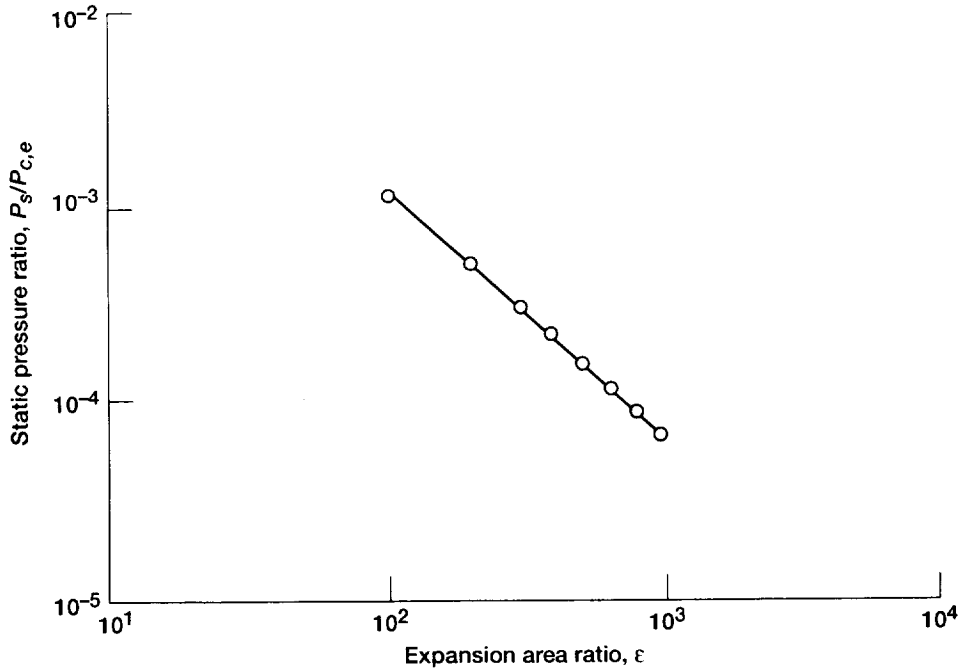

Figure 15.—Typical nozzle wall static pressure distribution (reading 577).

TABLE IX.—NOZZLE WALL STATIC PRESSURES

Reading	Effective combustion at chamber total pressure nozzle entrance, $P_{c,e}$		Propellent mixture ratio, O/F	Expansion area ratio, ε					
				100		101.2		200	
				Nozzle wall static pressure, P_s					
	MPa	psia		kPa	psia	kPa	psia	kPa	psia
569	12.326	1787.7	3.89	13.34	1.935	------	------	5.766	0.8362
570	12.645	1834.0	5.97	14.39	2.087	------	------	6.281	.9109
571	12.488	1811.1	4.70	14.90	2.161	------	------	6.470	.9383
575	14.350	2081.2	4.65	17.03	2.470	------	------	7.350	1.066
576	14.605	2118.2	5.68	17.20	2.495	------	------	7.426	1.077
577	14.225	2063.1	4.47	16.80	2.436	------	------	7.302	1.059
580	16.364	2373.3	4.27	19.09	2.769	------	------	8.253	1.197
601	12.768	1851.8	6.15	------	------	14.78	2.143	------	------
602	12.542	1819.0	5.11	------	------	14.79	2.145	------	------
603	12.457	1806.7	4.01	------	------	13.68	1.984	------	------

Reading	Expansion area ratio, ε									
	202.4		300		303.6		388		392.7	
	Nozzle wall static pressure, P_s									
	kPa	psia	kPa	psia	kPa	psia	kPa	psia	kPa	psia
569	------	------	3.476	0.5041	------	------	2.522	0.3658	------	------
570	------	------	3.929	.5699	------	------	2.990	.4337	------	------
571	------	------	3.895	.5649	------	------	2.832	.4108	------	------
575	------	------	4.456	.6462	------	------	3.252	.4717	------	------
576	------	------	4.656	.6753	------	------	3.512	.5093	------	------
577	------	------	4.410	.6396	------	------	3.232	.4688	------	------
580	------	------	4.955	.7186	------	------	3.609	.5234	------	------
601	6.847	0.9930	------	------	4.028	0.5842	------	------	3.026	0.4389
602	6.723	.9750	------	------	4.003	.5805	------	------	2.968	.4305
603	6.172	.8952	------	------	3.725	.5403	------	------	2.755	.3996

Reading	Expansion area ratio, ε							
	500		635		800		975	
	Nozzle wall static pressure, P_s							
	kPa	psia	kPa	psia	kPa	psia	kPa	psia
569	1.789	0.2594	1.351	0.1959	1.008	0.1462	0.7853	0.1139
570	2.224	.3225	1.624	.2356	1.197	.1736	.9163	.1329
571	2.035	.2952	1.496	.2169	1.105	.1602	.8550	.1240
575	2.299	.3335	1.687	.2446	1.247	.1809	.9646	.1399
576	2.535	.3676	1.854	.2689	1.362	.1975	1.048	.1520
577	2.289	.3320	1.674	.2428	1.246	.1807	.9550	.1385
580	2.549	.3697	1.872	.2715	1.380	.2002	1.069	.1551
601	------	------	------	------	------	------	------	------
602	------	------	------	------	------	------	------	------
603	------	------	------	------	------	------	------	------

Ten successful firings were accomplished at altitude—seven with the 1025:1-area-ratio nozzle and three with the nozzle truncated to an area ratio of 440:1. Table II summarizes the hot-fire results, including measured and calculated values.

Figure 16 shows the nozzle thrust performance in terms of $C_{F,V}$. Two sets of data are shown: the first is for the original nozzle with the 1025:1 area ratio, and the second is for the truncated nozzle with the 440:1 area ratio. Straight lines of the best fit by the least-squares method are shown. For the 1025:1 nozzle, the thrust coefficients ranged from approximately 1.92 to 2.02, and for the 440:1 nozzle, they ranged from 1.83 to 1.94.

The nozzle thrust efficiency is shown in figure 17 as straight lines of the best fit by the least-squares method. The efficiencies ranged from approximately 96.6 to 97.5 percent for the 1025:1 nozzle and from 94.0 to 94.2 percent for the 440:1 nozzle.

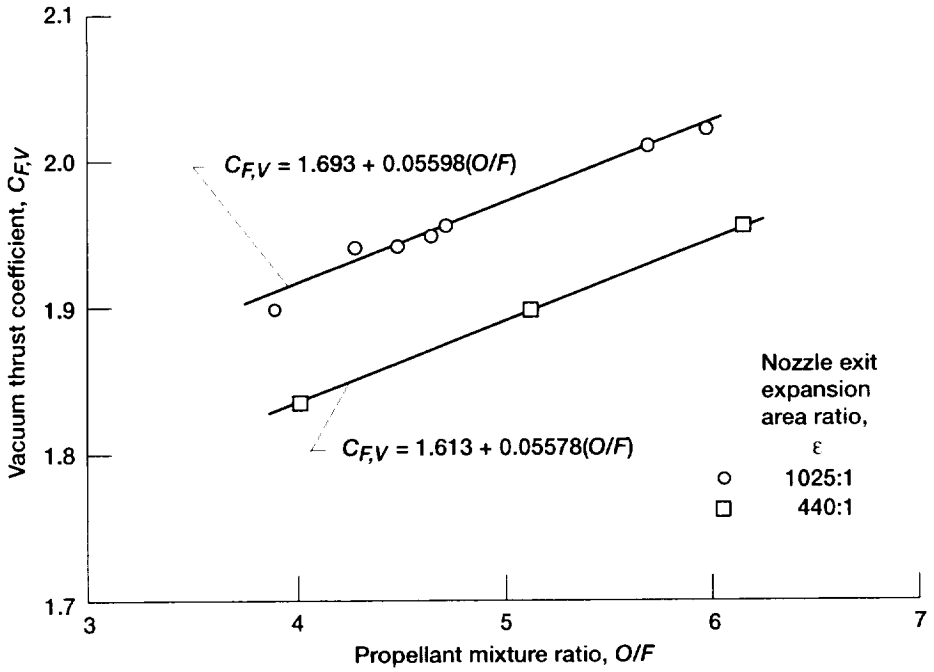

Figure 16.—Nozzle thrust performance as a function of mixture ratio.

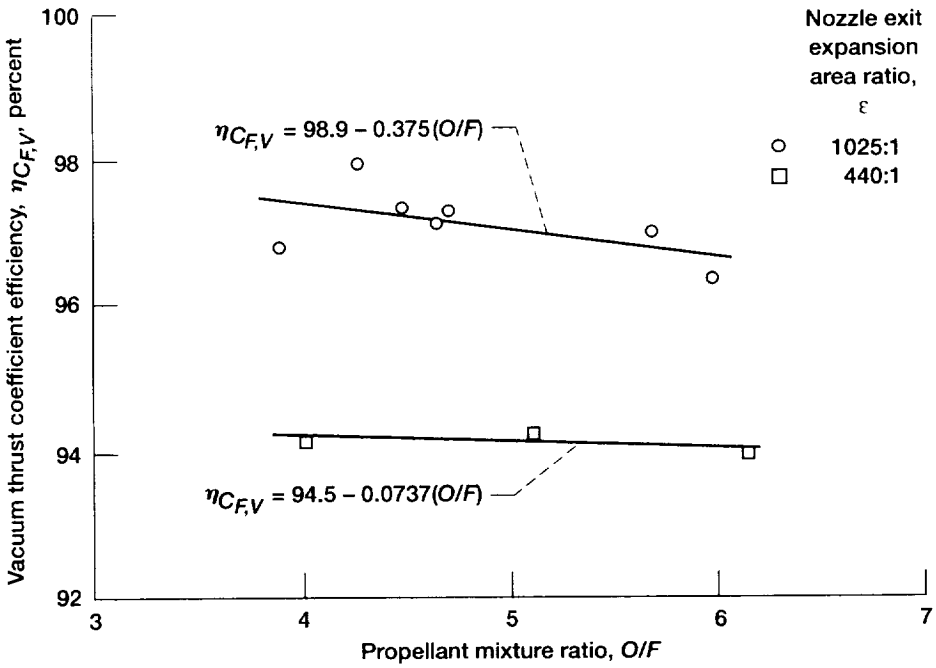

Figure 17.—Nozzle thrust efficiency as a function of mixture ratio.

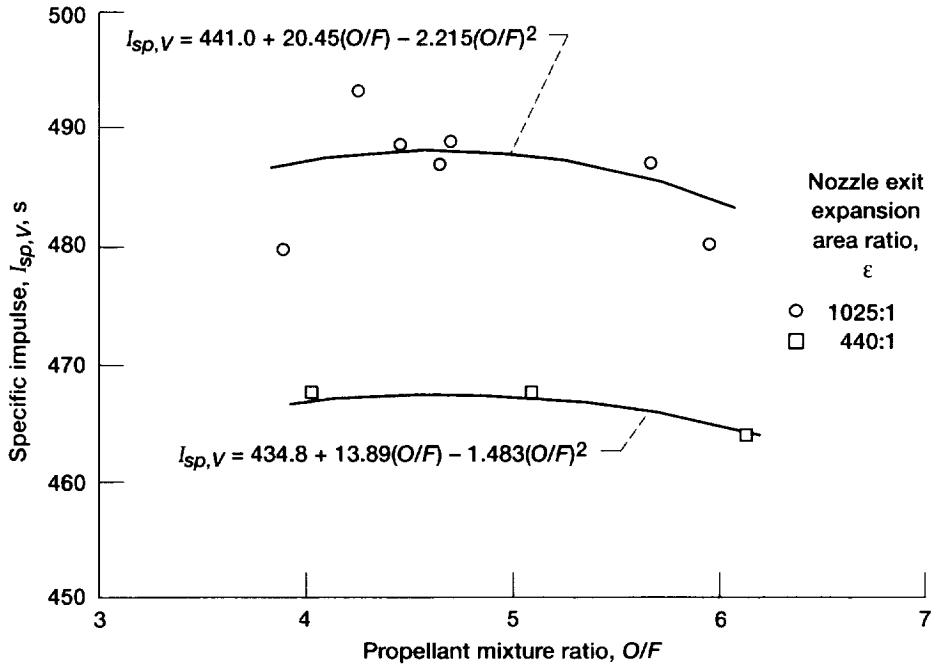

Figure 18.—Overall thruster performance as a function of mixture ratio.

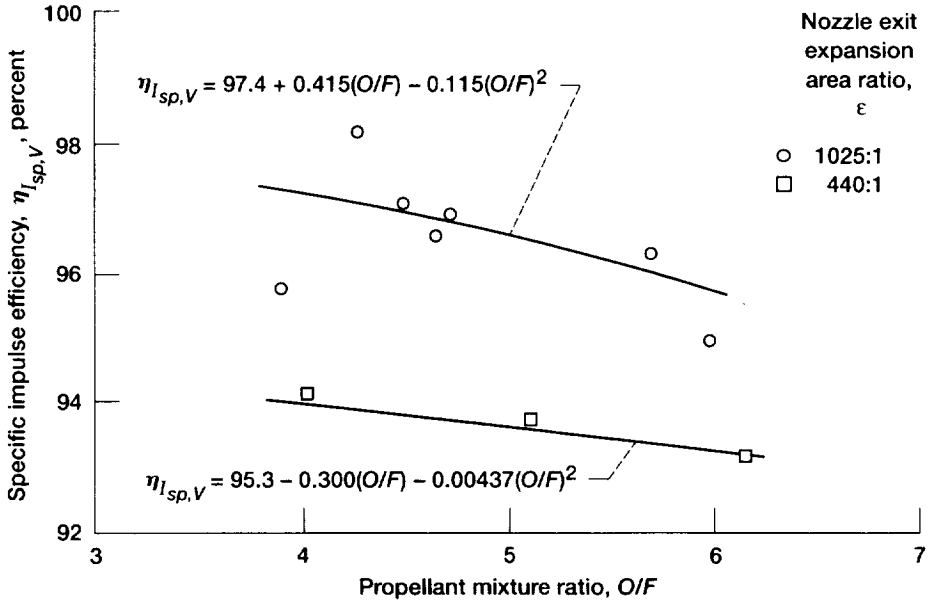

Figure 19.—Overall thruster efficiency as a function of mixture ratio.

Figure 18 shows the overall thruster performance with a plot of specific impulse versus *O/F* for both the 1025:1 and 440:1 configurations. The faired curves were obtained from the product of the faired curves of figure 17 and the theoretical ODE values of reference 21. The specific impulse attained was as high as 488 sec for the 1025:1-nozzle configuration and 467 sec for the 440:1-nozzle configuration.

Figure 19 shows the overall thruster efficiency as the specific impulse efficiency plotted as a function of *O/F* for the 1025:1- and 440:1-area-ratio configurations. Ideally, overall specific impulse efficiency should be equal to the product of η_{C^*} and $\eta_{C_{F,V}}$ as shown in equation (16):

$$\eta_{C^*} \times \eta_{C_{F,V}} = \eta_{I_{sp,V}} \tag{16}$$

The faired curves shown in figure 19 were obtained from the product of the best-fit curves of η_{C^*} and $\eta_{C_{F,V}}$ from figures 14 and 17, respectively. The coincidence of the faired curves through the center of the apparent data scatter reinforces the quality of the results. Deviations from this relationship were attributed to measurement uncertainties in effective combustion chamber total pressure, vacuum force, and mass flow rate. Values of $\eta_{I_{sp,V}}$ ranged from 95.5 to 97.5 percent for the 1025:1 configuration and from 93.3 to 94.0 percent for the 440:1 configuration.

TABLE X.—TDK/BLM TURBULENT PREDICTIONS

Reading	Nozzle exit expansion area ratio, ε	Effective combustion chamber total pressure at nozzle entrance, $P_{c,e}$		Measured propellant mixture ratio, O/F	Predicted propellant flow rate	
		MPa	psia		kg/s	lb_m/s
569	1025	12.326	1787.7	3.89	2.5144	5.5432
570	↓	12.645	1834.0	5.97	2.7306	6.0198
571	↓	12.488	1811.1	4.70	2.5937	5.7181
575	↓	14.350	2081.2	4.65	2.9469	6.5628
576	↓	14.605	2118.2	5.68	3.1214	6.8813
577	↓	14.225	2063.1	4.47	2.9370	6.4748
580	↓	16.364	2373.3	4.27	3.3617	7.4111
601	440	12.768	1851.8	6.15	2.7384	6.0371
602	440	12.542	1819.0	5.11	2.6018	5.7359
603	440	12.457	1806.7	4.01	2.5135	5.5413

Reading	Nozzle exit expansion area ratio, ε	Computer code: TDK/BLM Turbulent					
		Predicted characteristic exhaust velocity, C*		Predicted vacuum thrust, F_V		Predicted vacuum thrust coefficient, $C_{F,V}$	Predicted vacuum thrust coefficient efficiency, $\eta_{C_{F,V}}$, percent
		m/s	ft/s	N	lb_f		
569	1025	2483.97	8149.51	11 701	2630.72	1.87	95.49
570	↓	2346.55	7698.65	12 754	2867.32	1.99	94.84
571	↓	2439.50	8003.61	12 132	2727.59	1.92	95.26
575	↓	2442.52	8013.52	13 935	3132.98	1.92	95.45
576	↓	2370.80	7778.23	14 619	3286.56	1.98	95.12
577	↓	2454.20	8051.85	13 742	3089.58	1.91	95.48
580	↓	2466.44	8091.99	15 719	3533.93	1.90	95.56
601	440	2334.25	7658.31	12 445	2797.95	1.95	93.61
602	440	2413.37	7917.89	11 861	2666.66	1.89	93.75
603	440	2481.10	8140.08	11 410	2565.17	1.83	93.83

Reading	Nozzle exit expansion area ratio, ε	Computer code				Predicted vacuum specific impulse (adjusted), $I_{sp,V}$	Predicted vacuum specific impulse efficiency (adjusted), $\eta_{I_{spV}}$, percent
		ODE	ODK	MOC	TDK/BLM turbulent		
		Predicted vacuum specific impulse, $I_{sp,V}$, s					
569	1025	500.63	499.61	495.13	474.59	473.73	94.63
570	↓	505.53	502.12	498.63	476.31	471.89	93.35
571	↓	504.43	502.71	498.57	477.01	475.35	94.23
575	↓	503.90	502.51	498.30	477.38	475.79	94.42
576	↓	505.55	503.10	499.40	477.61	473.96	93.75
577	↓	503.48	502.22	497.93	477.17	475.82	94.51
580	↓	502.54	501.62	497.23	476.84	475.70	94.66
601	440	497.81	494.39	482.30	463.46	458.64	92.13
602	440	498.99	496.98	483.92	464.91	462.62	92.71
603	440	496.58	495.52	481.57	462.92	462.01	93.04

TABLE XI.—TDK/MABL TURBULENT PREDICTIONS

Reading	Nozzle exit expansion area ratio, ε	Effective combustion chamber total pressure at nozzle entrance, $P_{c,e}$		Propellant mixture ratio, O/F	Predicted propellant flow rate	
		MPa	psia		kg/s	lb_m/s
569	1025	12.326	1787.7	3.89	2.5095	5.5323
570	↓	12.645	1834.0	5.97	2.7240	6.0052
571		12.488	1811.1	4.70	2.5883	5.7061
575		14.350	2081.2	4.65	2.9708	6.5494
576		14.605	2118.2	5.68	3.1143	6.8658
577		14.225	2063.1	4.47	2.9311	6.4618
580	↓	16.364	2373.3	4.27	3.3556	7.3976
601	440	12.768	1851.8	6.15	2.7342	6.0277
602	440	12.542	1819.0	5.11	2.5989	5.7296
603	440	12.457	1806.7	4.01	2.5127	5.5395

Reading	Nozzle exit expansion area ratio, ε	Predicted characteristic exhaust velocity, C*		Computer code: TDK/MABL Turbulent			
				Predicted vacuum thrust, F_V		Predicted vacuum thrust coefficient, $C_{F,V}$	Predicted vacuum thrust coefficient efficiency, $\eta_{C_{F,V}}$, percent
		m/s	ft/s	N	lb_f		
569	1025	2488.86	8165.54	11 690	2628.16	1.87	95.40
570	↓	2352.27	7717.43	12 751	2866.68	1.99	94.82
571		2444.64	8020.47	12 108	2722.22	1.91	95.07
575		2447.53	8029.95	13 923	3130.11	1.91	95.36
576		2376.16	7795.79	14 614	3285.59	1.98	95.09
577		2459.12	8067.99	13 732	3087.30	1.91	95.41
580	↓	2470.97	8106.85	15 710	3531.83	1.89	95.50
601	440	2337.88	7670.21	12 458	2800.75	1.95	93.70
602	440	2416.01	7926.55	11 883	2671.58	1.89	93.93
603	440	2481.91	8142.74	11 426	2568.73	1.83	93.96

Reading	Nozzle exit expansion area ratio, ε	Computer code					
		ODE	ODK	MOC	TDK/MABL turbulent	Predicted vacuum specific impulse (adjusted), $I_{sp,V}$	Predicted vacuum specific impulse efficiency (adjusted), $\eta_{I_{sp,V}}$, percent
		Predicted vacuum specific impulse, $I_{sp,V}$, s					
569	1025	500.63	499.61	495.13	475.06	474.20	94.72
570	↓	505.53	502.12	498.63	477.37	472.93	93.55
571		504.43	502.71	498.58	477.07	475.41	94.25
575		503.90	502.51	498.32	477.92	476.33	94.53
576		505.55	503.09	499.43	478.54	474.89	93.94
577		503.48	502.22	497.95	477.78	476.42	94.63
580	↓	502.54	501.62	497.24	477.43	476.29	94.78
601	440	497.81	494.36	482.36	464.64	459.82	92.37
602	440	498.99	496.98	483.98	466.28	463.98	92.98
603	440	496.58	495.52	481.61	463.71	462.80	93.20

All the results discussed previously were compared with analytical predictions obtained from the TDK computer program, as previously described. Two turbulent models were run for each firing: one with the BLM module and one with the MABL module. A laminar boundary layer module was also run with the MABL module. Tables X and XI give the turbulent results for the BLM and MABL modules.(Laminar results are given in table XVI in app. B.) Close examination of these tabulated results shows that there is no significant difference between the results obtained with the turbulent BLM and

MABL modules. This is consistent with the findings of reference 6, which studied a 300:1 liquid hydrogen and liquid oxygen nozzle. For simplicity, the rest of this discussion is limited to the results obtained with the MABL module.

Table II gives the individual firing data points with the scatter, and the following paragraph discusses the mean values represented by curve fits of these data. Figure 20 is a plot of the predicted results and the attained $I_{sp,V}$ of the thruster with the 1025:1 nozzle as a function of *O/F*. The ODE values are the predicted ideal, one-dimensional equilibrium values of specific impulse. The ODK values are the predicted results for one-dimensional, nonequilibrium flow, and the drop in $I_{sp,V}$ from ODE to ODK represents the predicted loss in performance due to kinetics. The third line, which was obtained from the MOC module, represents the inviscid, two-dimensional, nonequilibrium predictions. The difference between the ODK and MOC values is the loss in performance due to nozzle divergence and shock losses occurring in the inviscid core portion of the nozzle flow.

The next specific impulse decrement to be considered is the losses attributable to the boundary layer. The analytical model used for this is the MABL module of the TDK computer program. The first line, which is labeled TDK/MABL(lam), represents losses attributable to laminar boundary layer growth along the nozzle wall. This is followed by the line labeled "laminar," which represents performance losses attributable to combustion losses or energy release losses. This was determined by multiplying the last predicted $I_{sp,V}$ values by η_{C^*}. These predicted $I_{sp,V}$ values can be compared with the experimentally attained $I_{sp,V}$. Next, is the line representing the experimental results. For simplicity, the figure—the individual scatter of the experimental results—was not included and only the best fit curve was shown. The line labeled TDK/MABL (turb) represents losses attributable to turbulent boundary layer growth along the nozzle wall. The last performance decrement to be considered is the $I_{sp,V}$ losses attributable to combustion losses or energy release loss. These are given in the bottom line on the chart labeled "turbulent." The experimentally measured values did not fall on either the predicted laminar values or turbulent values as expected, but do have very similar shapes and are very nearly parallel to one another.

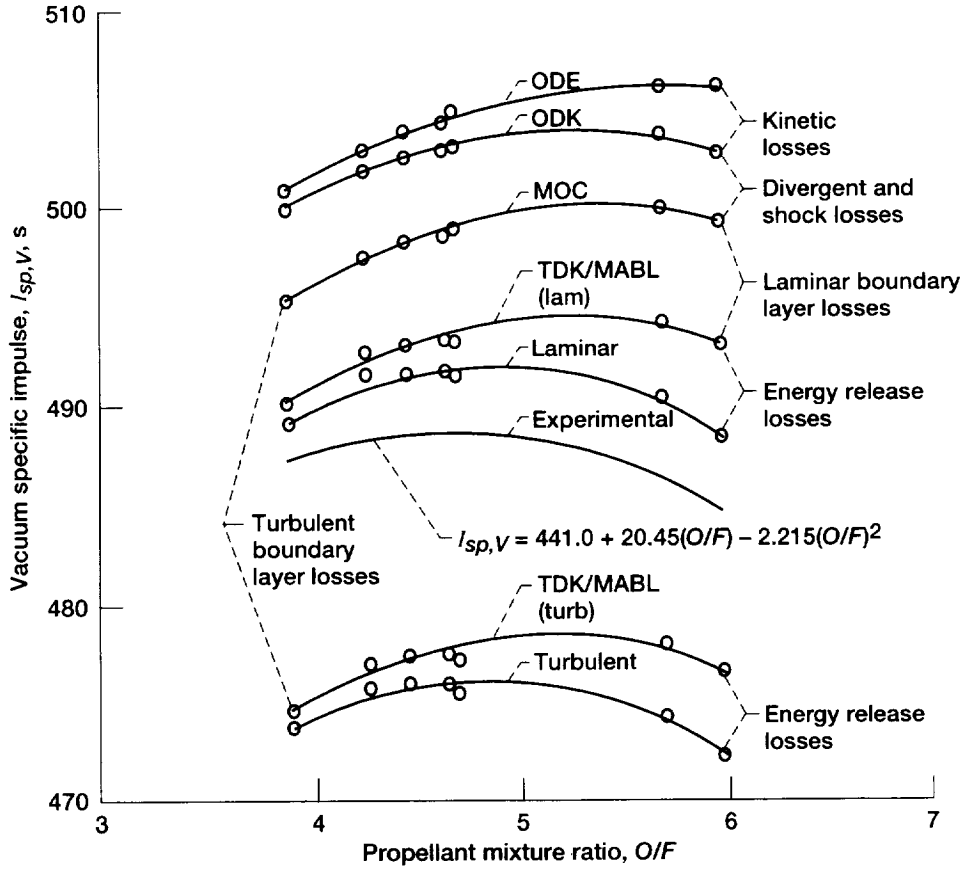

Figure 20.—Predicted thrust chamber losses from ideal performance. Area ratio, ε, 1025:1.

Figure 21 is a plot of $\eta_{I_{sp,V}}$ as a function of *O/F*. Values of the predicted laminar and turbulent impulse efficiencies are shown for comparison to the curve of the experimentally achieved impulse efficiency. Predicted laminar values are about 0.5-percent higher than the experimentally achieved values, and turbulent values are uniformly 2-percent lower than the experimentally achieved values.

Figure 22 is a plot of $C_{F,V}$ for the 1025:1 nozzle as a function of *O/F*. Shown here are the values of the predicted laminar, turbulent, and experimentally achieved nozzle $C_{F,V}$. For

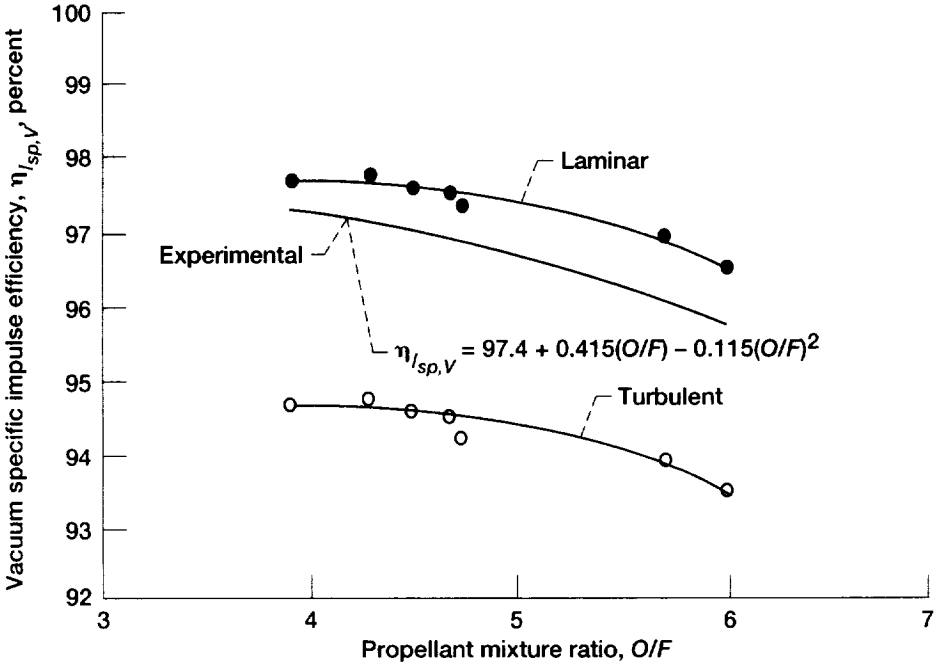

Figure 21.—Thrust chamber performance efficiency. Area ratio, ε, 1025:1. Specific impulse, $\eta_{I_{sp,V}}$, is based on ideal one-dimensional equilibrium (ODE) results.

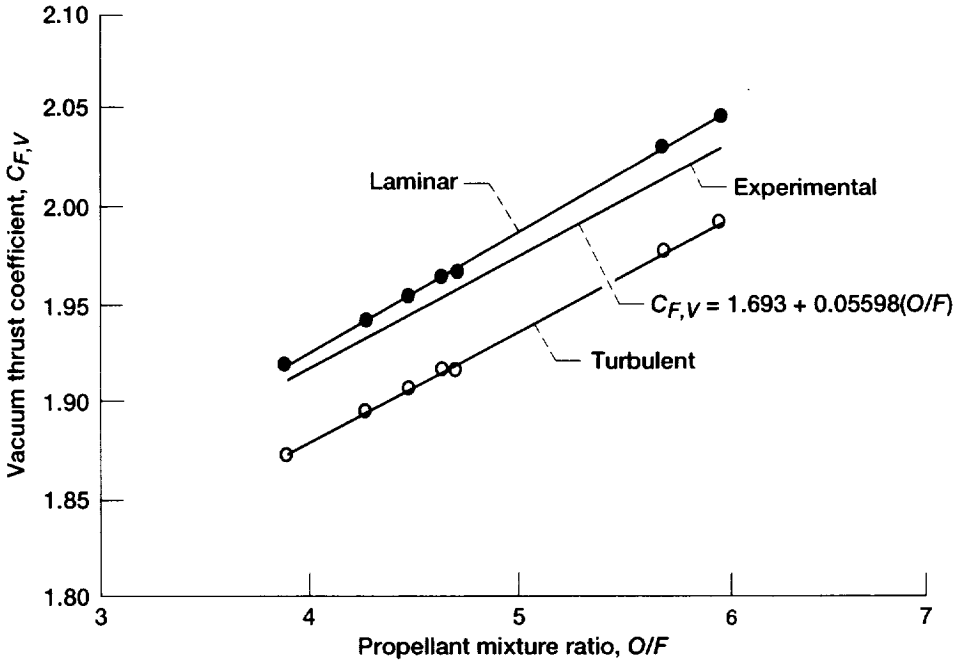

Figure 22.—Experimental and predicted nozzle vacuum thrust coefficient. Area ratio, ε 1025:1.

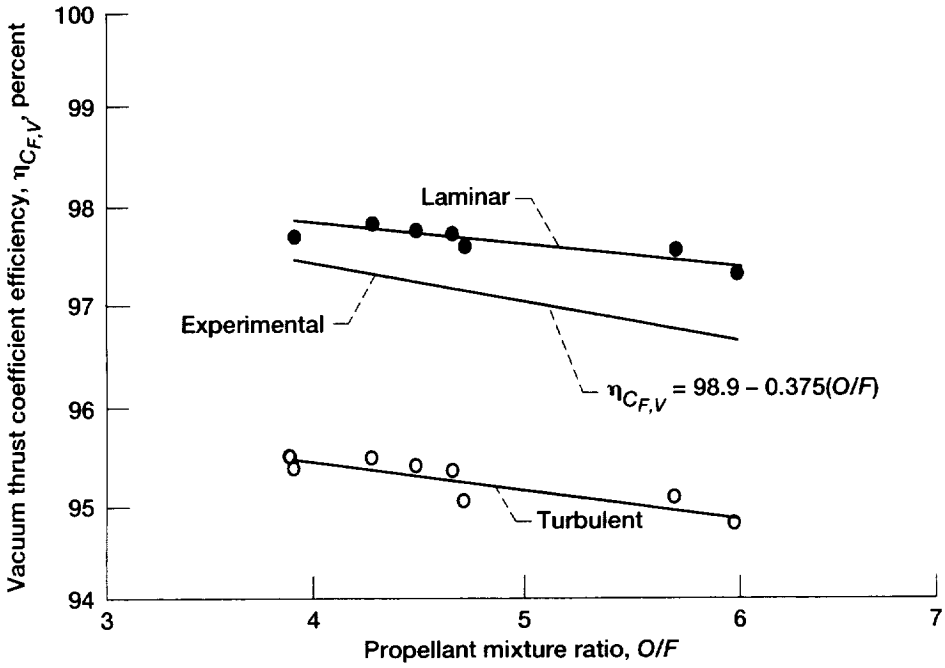

Figure 23.—Nozzle thrust coefficient efficiency. Area ratio, ε, 1025:1.

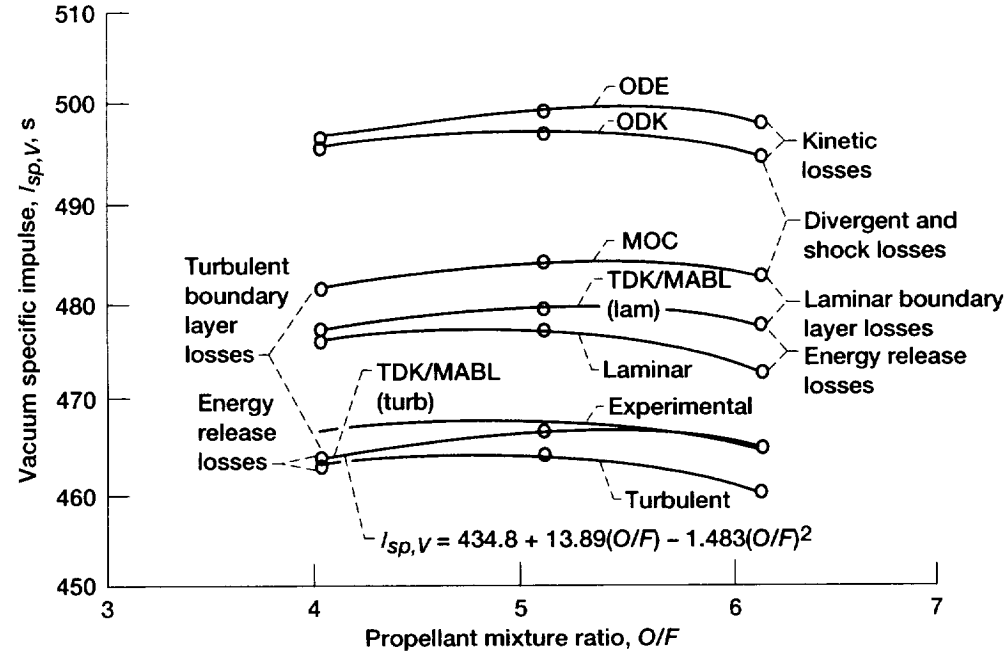

Figure 24.—Thrust chamber performance efficiency. Area ratio, ε, 440:1.

clarity, the best fit straight line was plotted instead of the experimental data scatter. As in figures 20 and 21, the experimentally achieved results are greater than the values obtained from the turbulent analysis but only slightly less than the values obtained from the laminar analysis.

Figure 23 shows nozzle $\eta_{C_{F,V}}$ as a function of *O/F*. As in figures 21 to 22, the experimentally achieved values are about 0.5-percent lower than the predicted laminar values and uniformly 2-percent higher than the predicted turbulent values.

For the next series of comparisons, the rearmost part of the nozzle was removed. This provided a nonoptimized nozzle truncated at an exit area ratio of 440:1 instead of extending to the optimized 1025:1 area ratio. The resulting divergence angles were higher than they would have been for an optimized 440:1 configuration. Figure 24 is a plot of predicted thruster performance and attained thruster performance for the 440:1 configuration. Shown are the results of three firings. In comparing the 440:1 performance (fig. 24) to that of the 1025:1 configuration (fig. 20), one observes the obvious decrease in performance (~20-s I_{sp}) attributable to both a reduced area ratio and an increased nozzle exit divergence angle. In comparison, the attained performance represented by the best fit curve to the predicted performance for the 440:1 configuration falls much closer to the predicted turbulent values than does the 1025:1 configuration, and it is lower than the predicted laminar values. Figure 25 summarizes this same result by showing $\eta_{I_{sp,V}}$ for the 440:1 configuration. In comparison to the 1025:1 configuration, again the experimentally attained efficiency for the 440:1 configuration is much closer to the TDK predicted turbulent values than to the predicted laminar values.

Figure 26 shows the $C_{F,V}$ of the 440:1-nozzle configuration as a function of *O/F*. As was the case for the 1025:1 configuration, $C_{F,V}$ varies linearly with respect to *O/F*, and the experimental values fall quite close to the TDK turbulent prediction, and well below the linear predictions. Again, this is significantly different from the 1025:1 results, where the experimental values were closer to the laminar predictions. This correspondence is further illustrated in figure 27, which is a plot of $\eta_{C_{F,V}}$ as a function of *O/F*. The efficiency expressed here is, as elsewhere in this paper, based on the ODE values. The experimentally attained efficiency is about 0.25-percent higher than the turbulent prediction and nearly 2-percent lower than the laminar predictions.

Heat Transfer Results

The following is a discussion of the heat-transfer results obtained using the experimentally measured outer wall temperatures. These results are presented in tables III and VI. Table III contains the calculated nozzle inner wall temperatures, and table VI contains the calculated heat flux to the nozzle wall. These temperatures and fluxes represent the experimentally determined values. The distribution of temperature along the length of the nozzle is shown in figure 28 for a typical firing

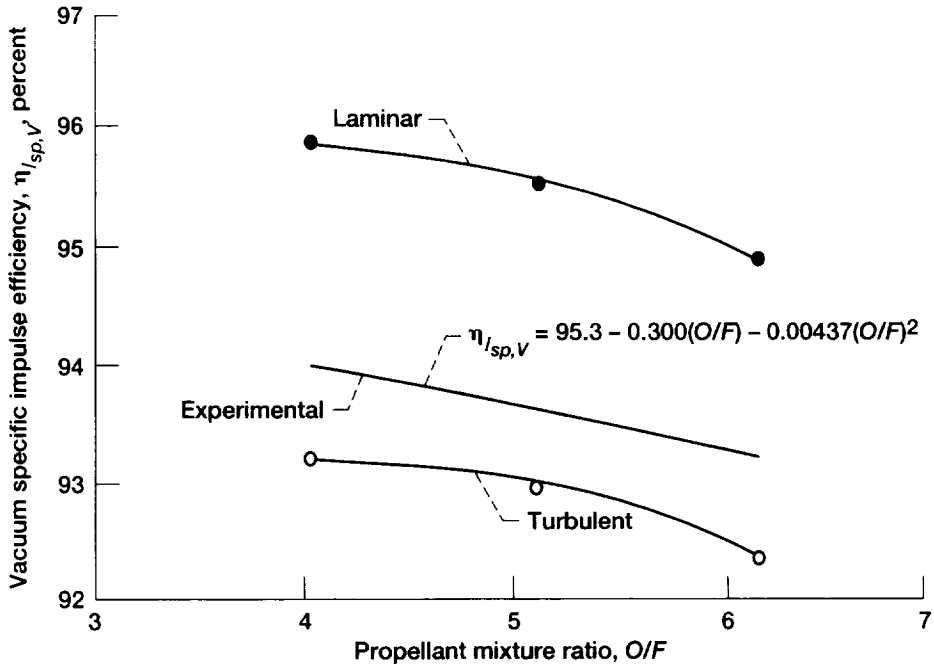

Figure 25.—Thrust chamber performance efficiency. Area ratio, ε, 440:1.

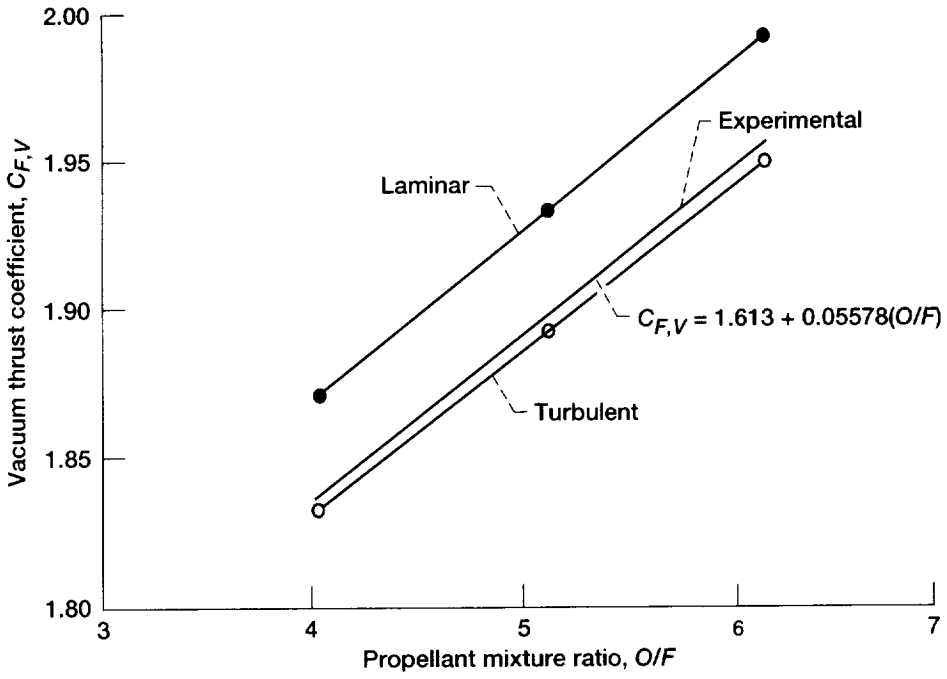

Figure 26.—Experimental and predicted nozzle vacuum thrust coefficient. Area ratio, ε, 440:1.

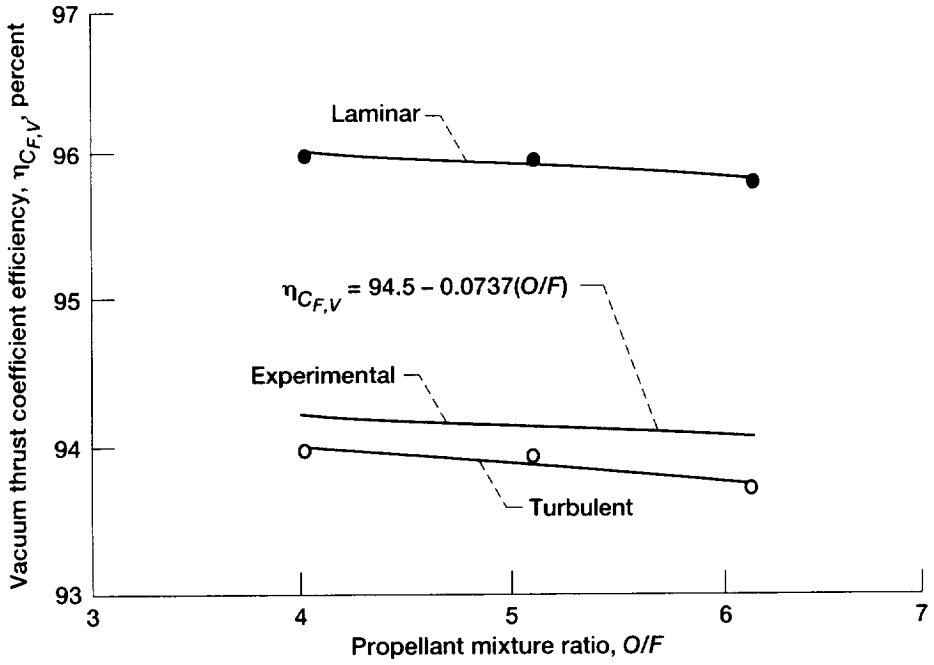

Figure 27.—Nozzle thrust coefficient efficiency. Area ratio, ε, 440:1.

(reading 577). Shown here are the measured outside wall temperatures and the calculated inner wall temperatures as a function of the nozzle length expressed as the expansion area ratio. Figure 29 shows the corresponding variation in calculated heat flux. Although the heat flux decreases to comparatively low values toward the exit of the nozzle, the corresponding nozzle surface areas involved increase substantially because of the nozzle contour. As a result, the heat rate to length ratio (product of heat flux times local circumference) of the transferred heat nearer the exit becomes more significant than is apparent in figure 29, which considers only the heat flux variation. This increased significance is apparent in figure 30,

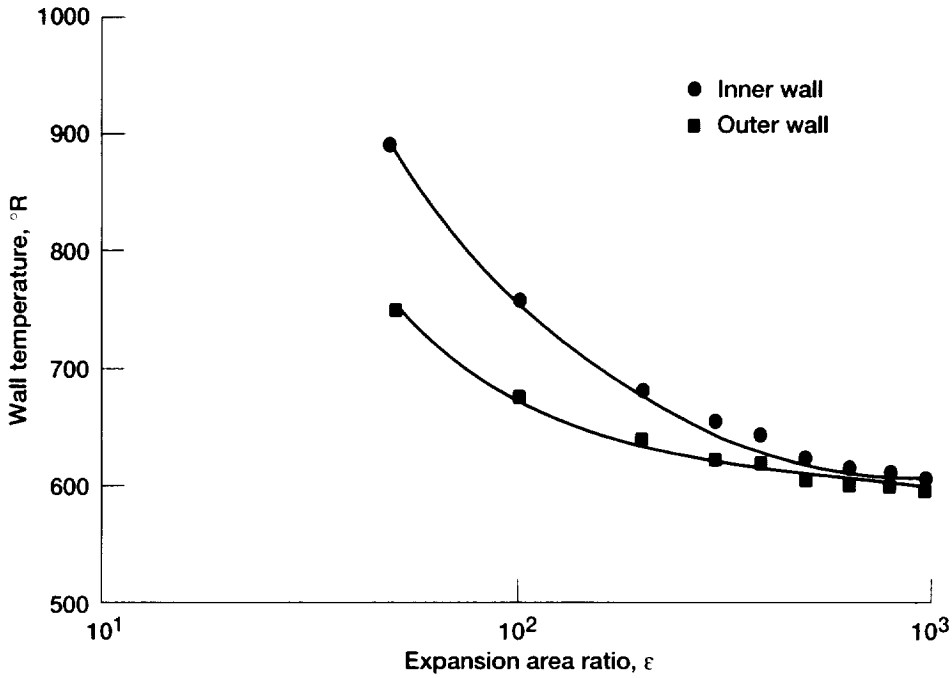

Figure 28.—Typical nozzle wall temperature distribution (reading 577).

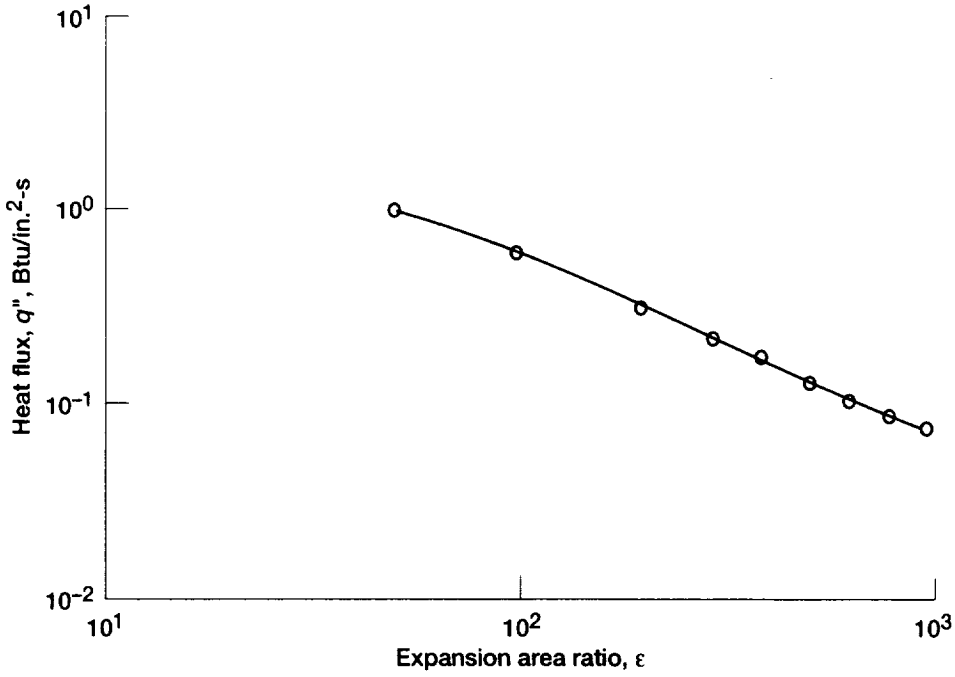

Figure 29.—Typical calculated nozzle heat flux distribution (reading 577, uncorrected *q*").

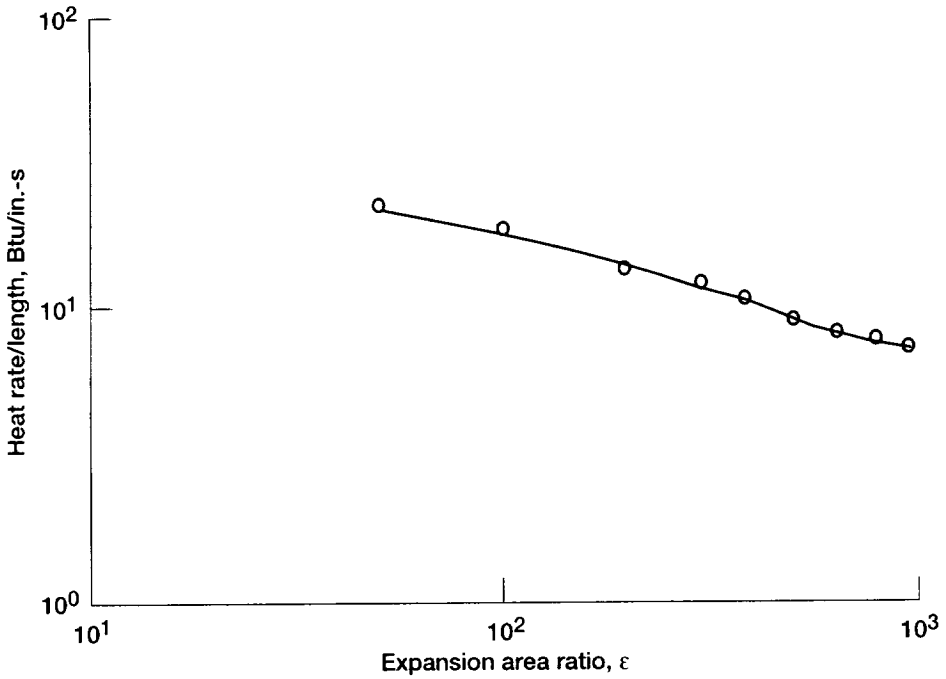

Figure 30.—Typical nozzle heat rate/length distribution versus expansion area ratio (reading 577, uncorrected q").

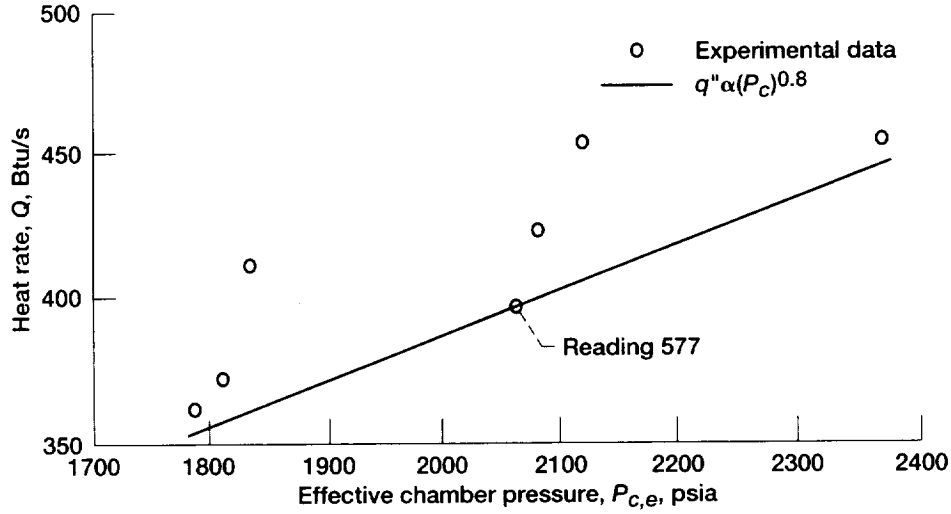

Figure 31.—Nozzle skirt heat rate (area ratio, ε, 140:1 to 1025:1) versus $P_{c,e}$.

which is a plot of the heat rate to length ratio as a function of the axial length expressed in terms of the expansion area ratio for a typical firing (reading 577). In addition, the total heat rate from an area ratio of 140:1 to an area ratio of 1025:1 at the exit was calculated to show the total heat load for the nozzle skirt. This was done by integrating heat flux values over the wetted surface area of the nozzle (table VII). Figure 31 plots the heat rates as a function of the combustion chamber pressure. A faired line of the slope $(P_c)^{0.8}$ was drawn through the reading 577 data point. For a given chamber configuration, heat-transfer rate can be considered proportional to the chamber pressure P_c raised to the 0.8 power (ref. 22). It is obvious that the data lie very parallel to this line, with a systematic scatter apparent because of the *O/F* variation of the firings.

To reconcile the P_c variation of these data, the heat rate values were adjusted to what they would have been if all the firings had been at the same P_c. The P_c selected was that of the typical firing, reading 577, which was 2063.1 psia. The other heat rate values were corrected by multiplying them by $(P_c)^{0.8}$. These values are tabulated in table VII and are also plotted in figure 32 versus *O/F*. The data are well characterized by a straight line and show a minimal amount of scatter, which is caused primarily by experimental uncertainty.

All these experimental results were then compared with the analytical predictions obtained from the TDK computer program as previously described. This computer code accounted for all the real effects expected with one exception. Because of the very specific nature of the various injectors and combustors used, the code was unable to account for combustion efficiency. Since we were able to measure this efficiency, an empirical correction was made to the heat flux calculations. This correction took the experimental values of heat flux and increased them to what they would have been had we had 100-percent combustion efficiency. Characteristic exhaust velocity C^* is proportional to the square root of the combustion gas temperature; therefore, $(\eta_{C^*})^2$ should vary directly with the combustion temperature and heat flux. Hence,

$$q''_{100\%} = \frac{q''}{(\eta_{C^*})^2} \tag{17}$$

The empirical values of η_{C^*} as a function of *O/F* were read from the best fit curve, equation (15) from figure 14. The adjusted experimental heat flux values are tabulated in table XII. Table XII also includes heat flux values predicted by the TDK computer code with the turbulent BLM and MABL modules. In addition, a laminar boundary layer module was run using the MABL module. For reference, results can be found in table XVII of appendix B. Because there was no significant difference between the turbulent BLM and MABL modules, the remaining calculations and discussion are limited to results calculated with the MABL module.

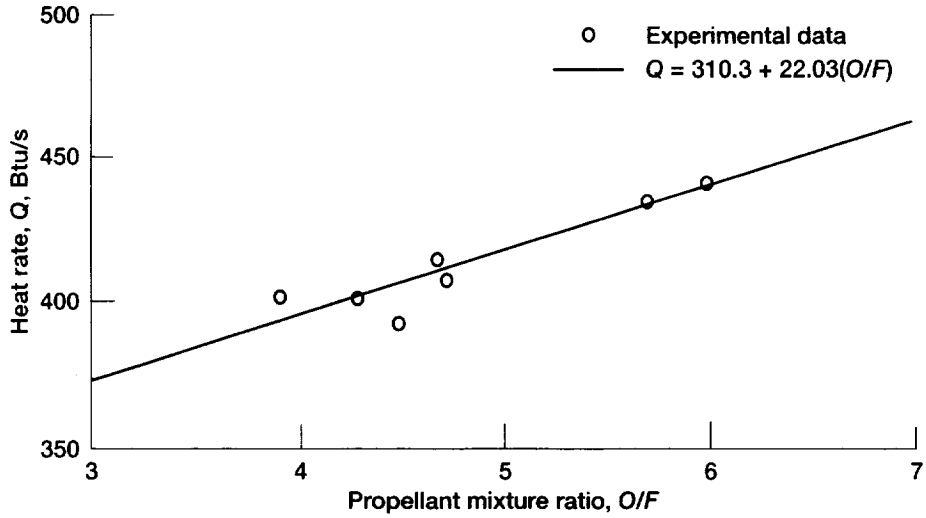

Figure 32.—Nozzle skirt heat rate (area ratio, ε, 140:1 to 1025:1) as a function of mixture ratio (corrected to $P_{c,e}$ = 2063.1 psia). Curve represents heat rate, Q.

TABLE XII.—EXPERIMENTAL (η_{C^*} = 100 PERCENT) AND TDK TURBULENT HEAT FLUX DISTRIBUTIONS

Reading	Effective combustion chamber total pressure at nozzle entrance, $P_{c,e}$		Propellant mixture ratio, O/F	Expansion area ratio, ε					
				50		100		200	
				Heat flux to nozzle walls					
	MPa	psia		kW/m^2	$Btu/in.^2$-s	kW/m^2	$Btu/in.^2$-s	kW/m^2	$Btu/in.^2$-s
Experimental adjusted to η_{C^*} = 100 percent									
569	12.326	1787.7	3.89	1428.00	0.8738	774.80	0.4741	413.46	0.2530
570	12.645	1834.0	5.97	1857.97	1.1369	1025.82	.6277	538.48	.3295
571	12.488	1811.1	4.70	1643.72	1.0058	902.76	.5524	470.83	.2881
575	14.350	2081.2	4.65	1815.81	1.1111	1009.31	.6176	547.80	.3352
576	14.605	2118.2	5.68	2013.55	1.2321	1117.66	.6839	598.62	.3663
577	14.225	2063.1	4.47	1621.66	.9923	942.47	.5767	491.58	.3008
580	16.364	2373.3	4.27	1856.50	1.1360	1070.43	.6550	588.98	.3604
TDK/MABL turbulent									
569	12.326	1787.7	3.89	2556.94	1.5646	1383.06	0.8463	714.66	0.4373
570	12.645	1834.0	5.97	3098.37	1.8959	1670.53	1.0222	853.89	.5225
571	12.488	1811.1	4.70	2754.85	1.6857	1491.74	.9128	768.26	.4701
575	14.350	2081.2	4.65	3043.78	1.8625	1673.79	1.0242	853.73	.5224
576	14.605	2118.2	5.68	3372.76	2.0638	1833.13	1.1217	942.47	.5767
577	14.225	2063.1	4.47	2975.80	1.8209	1618.23	.9902	829.05	.5073
580	16.364	2373.3	4.27	3242.83	1.9843	1780.18	1.0893	922.04	.5642
TDK/BLM turbulent									
569	12.326	1787.7	3.89	2553.84	1.5627	1361.98	0.8334	764.83	0.4680
570	12.645	1834.0	5.97	3222.90	1.9721	1719.06	1.0519	956.69	.5854
571	12.488	1811.1	4.70	2781.65	1.7021	1487.00	.9099	835.26	.5111
575	14.350	2081.2	4.65	3105.23	1.9001	1665.95	1.0194	926.45	.5669
576	14.605	2118.2	5.68	3493.69	2.1378	1868.92	1.1436	1037.91	.6351
577	14.225	2063.1	4.47	3011.75	1.8429	1603.85	.9814	892.30	.5460
580	16.364	2373.3	4.27	3245.94	1.9862	1760.57	1.0773	984.80	.6026

Reading	Expansion area ratio, ε											
	300		388		500		635		800		975	
	Heat flux to nozzle walls as measured											
	kW/m^2	$Btu/in.^2$-s	kW/m^2	$Btu/in.^2$-s	kW/m^2	$Btu/in.^2$-s	kW/m^2	$Btu/in.^2$-s	kW/m^2	$Btu/in.^2$-s	kW/m^2	$Btu/in.^2$-s
Experimental data adjusted to η_{C^*} = 100 percent												
569	297.92	0.1823	239.42	0.1465	180.91	0.1107	153.13	0.0937	143.49	0.0878	122.24	0.0748
570	378.33	.2315	297.76	.1822	220.79	.1351	170.78	.1045	133.84	.0819	111.62	.0683
571	336.16	.2057	267.04	.1634	200.69	.1228	155.74	.0953	126.33	.0773	103.77	.0635
575	384.70	.2354	302.50	.1851	225.36	.1379	178.30	.1091	140.38	.0859	118.97	.0728
576	414.12	.2534	327.67	.2005	243.50	.1490	189.90	.1162	145.77	.0892	124.20	.0760
577	353.00	.2160	279.95	.1713	209.18	.1280	166.20	.1017	136.62	.0836	118.32	.0724
580	411.67	.2519	327.34	.2003	245.79	.1504	189.25	.1158	148.55	.0909	127.47	.0780
TDK/MABL turbulent												
569	469.03	0.2870	355.78	0.2177	263.77	0.1614	201.99	0.1236	150.84	0.0923	117.99	0.0722
570	557.28	.3410	421.96	.2582	317.21	.1941	238.93	.1462	166.53	.1019	139.24	.0852
571	505.47	.3093	381.92	.2337	288.28	.1764	216.54	.1325	162.61	.0995	126.98	.0777
575	564.47	.3454	427.19	.2614	323.91	.1982	243.34	.1489	181.24	.1109	141.85	.0868
576	616.44	.3772	466.09	.2852	351.04	.2148	263.44	.1612	196.76	.1204	153.78	.0941
577	548.94	.3359	414.61	.2537	313.28	.1917	236.64	.1448	176.50	.1080	138.42	.0847
580	607.12	.3715	462.66	.2831	347.93	.2129	262.30	.1605	196.27	.1201	153.46	.0939
TDK/BLM turbulent												
569	493.38	0.3019	360.51	0.2206	275.37	0.1685	206.90	0.1266	155.58	0.0952	122.08	0.0747
570	615.13	.3764	449.58	.2751	341.23	.2088	257.39	.1575	193.00	.1181	151.82	.0929
571	538.65	.3296	392.55	.2402	302.34	.1850	226.34	.1385	170.13	.1041	133.68	.0818
575	601.08	.3678	437.00	.2674	334.04	.2044	251.51	.1539	188.59	.1154	148.39	.0908
576	667.43	.4084	488.64	.2990	372.28	.2278	278.80	.1706	209.51	.1282	164.24	.1005
577	577.05	.3531	423.27	.2590	323.91	.1982	243.99	.1493	183.04	.1120	144.14	.0882
580	642.91	.3934	470.66	.2880	358.72	.2195	269.16	.1647	202.48	.1239	158.69	.0971

Figure 33 compares the TDK-predicted heat flux values with the commensurate experimentally measured heat flux values for reading 577 (adjusted for η_{C^*}). This is a plot of the heat flux variation along the axial length of the nozzle expressed as the expansion area ratio. As seen in the figure, the experimental values fall below the heat flux values predicted by TDK for a turbulent boundary layer but are above the values predicted with a laminar boundary layer assumption. This was typical for all seven of the firings tabulated. This same variance between prediction and experiment is evident in figure 34, which is a plot of the heat rate to length ratio as a function of the location in the nozzle for reading 577. The heat rate to length ratio, which is the product of the heat flux times the local circumference, can take into consideration that the surface area of the nozzle is greater toward the exit because of the nozzle contour. Again, the experimental values fell below the heat rate to length ratios predicted by TDK for the turbulent boundary layer case but were above the values predicted with a laminar boundary layer assumption. The distributions of the heat flux and the heat rate to length ratio along the length of the nozzle were similar for all seven firings. Figure 35 illustrates the variation of the heat rate with respect to the *O/F*. This plot illustrates the total heat transferred from an area ratio of 140:1 to 1025:1 as a function of *O/F*. As with the previous two plots, the experimental results fall between the turbulent and laminar TDK predictions. Heat rate is the integral of the heat flux over the wetted surface area of the nozzle. All seven firings are represented by the data points obtained from table VII. Heat rates in this plot were generalized to a common combustion chamber pressure of 2063.1 psia, as they were in figure 32. The heat rates were also adjusted to the heat transfer values that would have occurred if the combustion were perfect (η_{C^*} = 100 percent) so that the TDK values could be compared to them. As in figures 33 and 34, the experimentally obtained values fall below the TDK-predicted values. This shortfall is quite consistent over the entire mixture ratio range, varying from 40 percent at *O/F* = 4 to 43 percent at *O/F* = 6.

Boundary Layer

Twelve firings were conducted at nominal combustion chamber pressures of 1800 psia, evenly divided amongst propellant mixture ratios of 4, 5, and 6. Six of these firings were with the 1037:1-area-ratio nozzle, and six were with the nozzle truncated to the 440:1 area ratio. In all these cases, boundary-layer pressure profile measurements were obtained with the previously described boundary-layer total pressure rakes.

To verify that the thrust performance and combustion performance of the 12 firings were representative of the firings without the rakes, the C^*, $C_{F,V}$, and $I_{sp,V}$ values were calculated

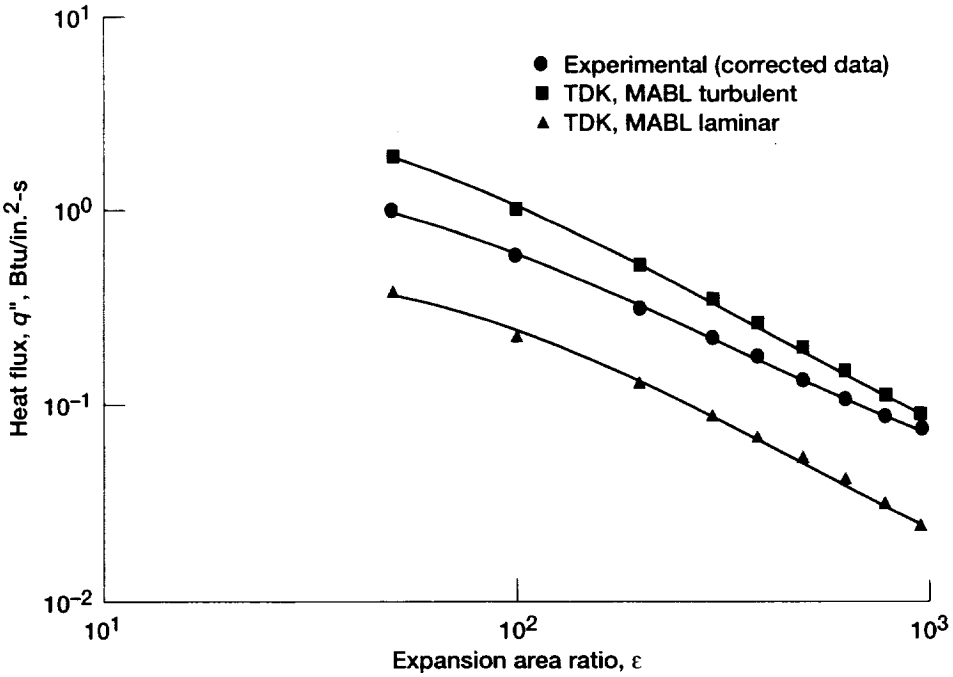

Figure 33.—Typical calculated (experimental) and predicted nozzle heat flux distribution (reading 577). Experimental values are corrected for characteristic exhaust velocity efficiency.

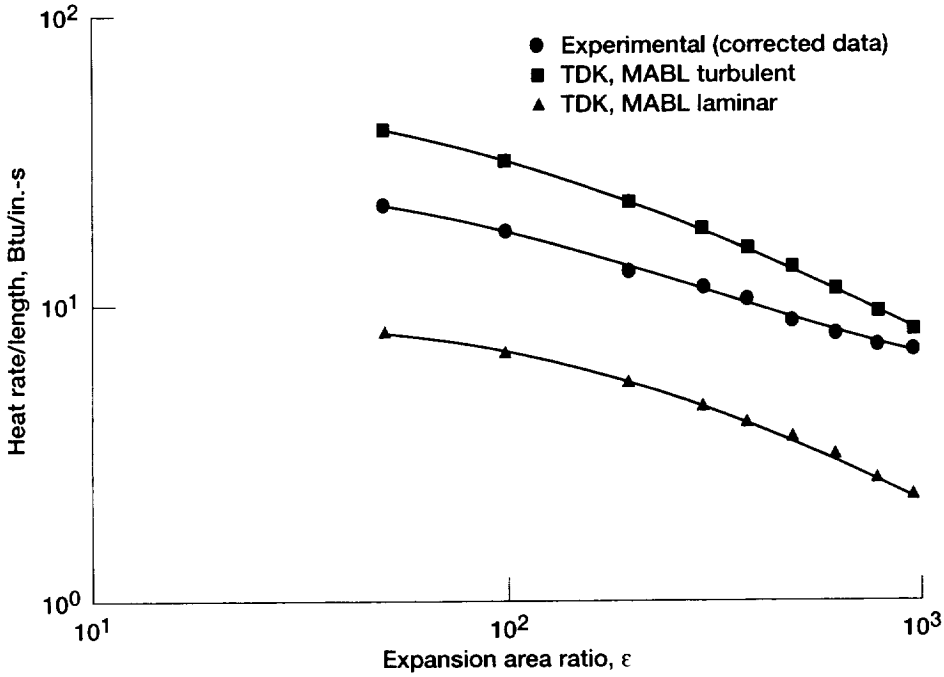

Figure 34.—Typical calculated (experimental) and predicted nozzle heat rate/length distribution (reading 577). Values are corrected for characteristic exhaust velocity efficiency.

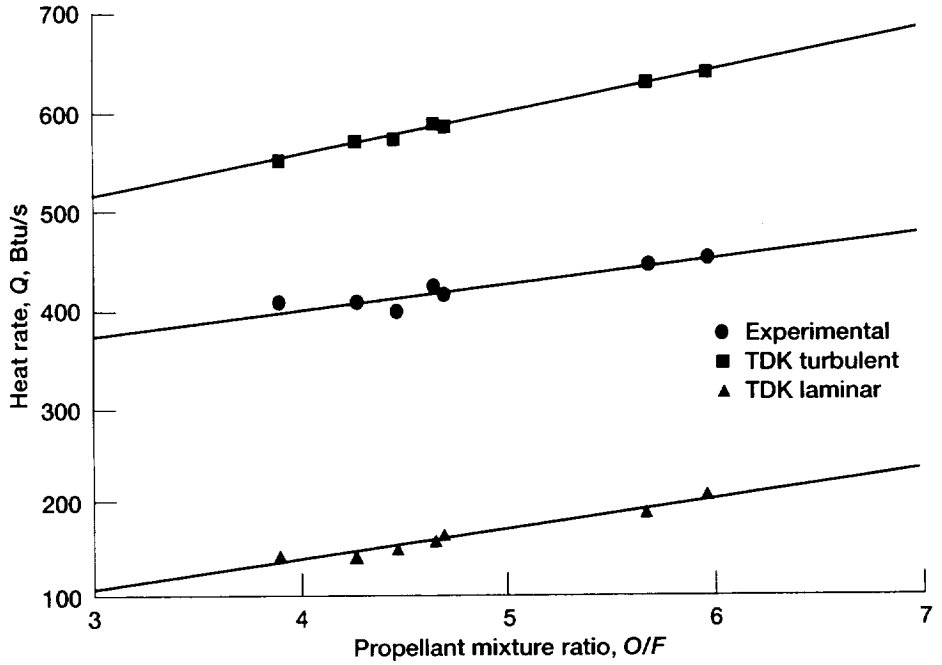

Figure 35.—Calculated (experimental) and predicted nozzle skirt heat rate as a function of mixture ratio. Area ratio, ε, 140:1 to 1025:1.

and compared with the results of the firings without the rakes. Table XIII lists the thrust performance results of the 12 firings, and figure 36 plots η_{C^*} versus *O/F*. The faired curve represented by the equation shown is the curve fit for the data without the rakes previously described. The plotted data points all fall within the scatter from earlier firings. Figure 37 shows the nozzle $C_{F,V}$ data of table XIII plotted versus *O/F*. In spite of the drag produced by the boundary-layer rakes and the small difference in area ratio, the thrust performance was essentially the same as for the previous tests. This is obvious in comparing the thrust coefficient data points with the fitted curves. Agreement with the previous tests is also evident in figure 38, which is a plot of the $\eta_{C_{F,V}}$ as a function of *O/F*. The faired lines represent the mean values of the previous firings. The data points, which are from table XIII, agree with the faired curves within the apparent scatter.

TABLE XIII.—RESULTS OF BOUNDARY LAYER TESTS

Reading	Nozzle throat area, A_t		Nozzle exit expansion area ratio, ε	Measured chamber pressure				Effective combustion chamber total pressure at nozzle entrace,[a] $P_{c,e}$		Propellant mixture ratio, O/F
				At injector end, $P_{c,a}$		Corrected for momentum pressure loss, $P_{c,T}$				
	cm^2	$in.^2$		MPa	psia	MPa	psia	MPa	psia	
589	5.007	0.776	1037	12.545	1820.0	12.507	1814.4	12.383	1796.5	3.97
592	↓	↓	↓	13.008	1887.1	12.940	1877.2	12.787	1855.1	5.91
593				12.678	1839.2	12.621	1831.0	12.484	1811.1	4.98
596				12.731	1847.0	12.676	1838.9	12.539	1819.1	4.91
597				12.580	1825.1	12.544	1819.8	12.421	1802.0	3.89
598			↓	13.090	1899.0	13.022	1889.1	12.870	1867.1	5.80
607			440	12.905	1872.2	12.836	1862.2	12.684	1840.2	5.99
608				12.651	1835.3	12.594	1827.0	12.458	1807.3	4.95
609				12.480	1810.6	12.443	1805.1	12.321	1787.4	3.91
612				12.978	1882.8	12.911	1873.0	12.760	1851.1	5.85
613				12.781	1854.2	12.727	1846.4	12.592	1826.8	4.76
614	↓	↓	↓	12.576	1824.5	12.542	1819.5	12.420	1801.8	3.84

Reading	Vacuum thrust, F_V		Ambient pressure around nozzle, P_a		Characteristic exhaust velocity, C^*		Characteristic exhaust velocity efficiency, η_{C^*}, percent
	N	lb_f	kPa	psia	m/s	ft/s	
589	11 885	2671.9	1.313	0.1905	2497	8193	99.9
592	12 920	2904.6	1.502	.218	2341	7680	98.9
593	12 318	2769.4	1.378	.200	2418	7934	99.2
596	12 369	2780.9	1.450	.210	2420	7938	99.1
597	11 860	2666.4	1.400	.203	2492	8175	99.5
598	13 015	2926.1	1.540	.223	2349	7707	98.9
607	12 278	2760.4	.892	.129	2350	7710	99.6
608	11 777	2647.6	.807	.117	2448	8031	100.4
609	11 298	2540.0	1.668	.242	2514	8248	100.5
612	12 427	2793.8	.928	.135	2372	7782	100.0
613	11 810	2655.1	.885	.128	2458	8065	100.2
614	11 322	2545.5	.849	.123	2509	8231	100.1

[a]Calculated with low nozzle exit expansion area ratio correlation.

TABLE XIII.—Concluded.

Reading	Fuel injection				Oxidizer injection				Propellant flow rate, $\dot{m}$	
	Pressure, P_{fi}		Temperature, T_{fi}		Pressure, P_{fi}		Temperature, T_{fi}			
	MPa	psia	K	°R	MPa	psia	K	°R	kg/s	lb_m/s
589	16.413	2381.1	299.4	539.0	13.670	1983.2	111.8	201.3	2.48	5.48
592	15.479	2245.6	300.7	541.3	14.490	2102.2	109.3	196.7	2.74	6.03
593	15.619	2265.9	300.1	540.1	13.962	2025.6	109.1	196.3	2.59	5.70
596	15.738	2283.2	299.3	538.8	14.044	2037.4	118.3	212.9	2.60	5.72
597	16.569	2403.8	298.2	536.8	13.678	1984.3	113.7	204.6	2.50	5.50
598	15.637	2268.5	298.8	537.9	14.607	2119.1	107.1	192.7	2.74	6.05
607	15.245	2211.6	298.3	536.9	14.367	2084.3	112.4	202.4	2.70	5.96
608	15.510	2250.1	298.2	536.7	13.902	2016.9	110.9	199.7	2.55	5.62
609	16.303	2365.1	298.0	536.4	13.549	1965.6	111.9	201.5	2.45	5.41
612	15.399	2234.0	301.2	542.1	14.449	2096.2	111.1	199.9	2.69	5.94
613	15.847	2299.0	300.3	540.6	14.042	2037.2	110.9	199.6	2.57	5.66
614	16.582	2405.6	299.9	539.8	13.648	1980.0	114.2	205.6	2.48	5.47

Reading	Measured vacuum thrust coefficient, $C_{F,V}$	Vacuum thrust coefficient efficiency, $\eta_{C_{F,V}}$, percent	Vacuum specific impulse, $I_{sp,V}$, s	Vacuum specific impulse efficiency, $\eta_{I_{sp,V}}$, percent
589	1.917	97.4	488.0	97.4
592	2.018	96.3	481.6	95.3
593	1.971	97.0	485.9	96.2
596	1.970	97.2	486.0	96.2
597	1.907	97.2	484.5	96.8
598	2.020	96.8	483.8	95.7
607	1.933	93.4	463.2	93.0
608	1.888	94.1	471.2	94.5
609	1.831	94.2	469.5	94.6
612	1.945	94.3	470.5	94.4
613	1.873	93.9	469.5	94.1
614	1.821	93.8	465.7	93.9

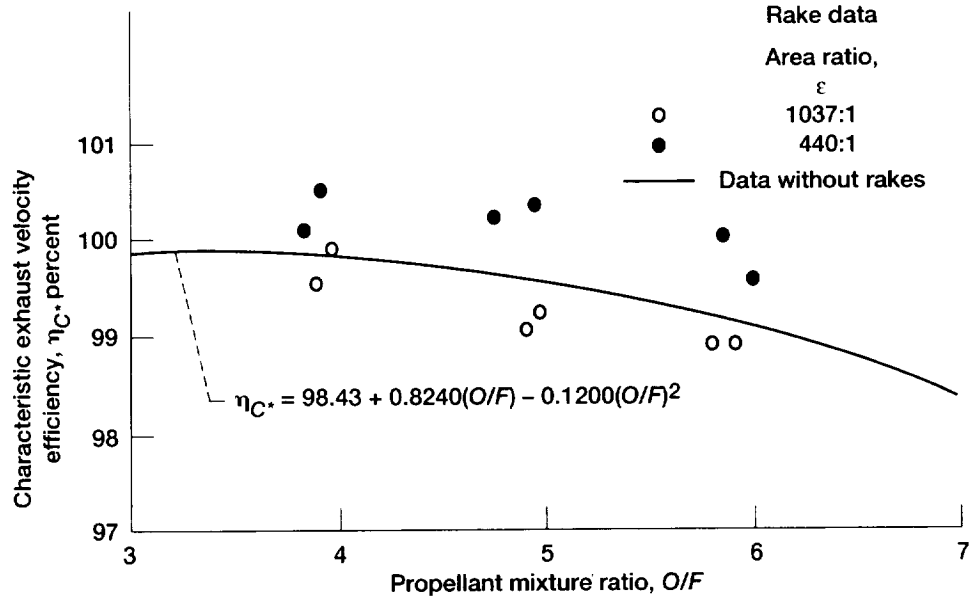

Figure 36.—Characteristic exhaust velocity efficiency as a function of mixture ratio for tests with boundary layer rakes installed.

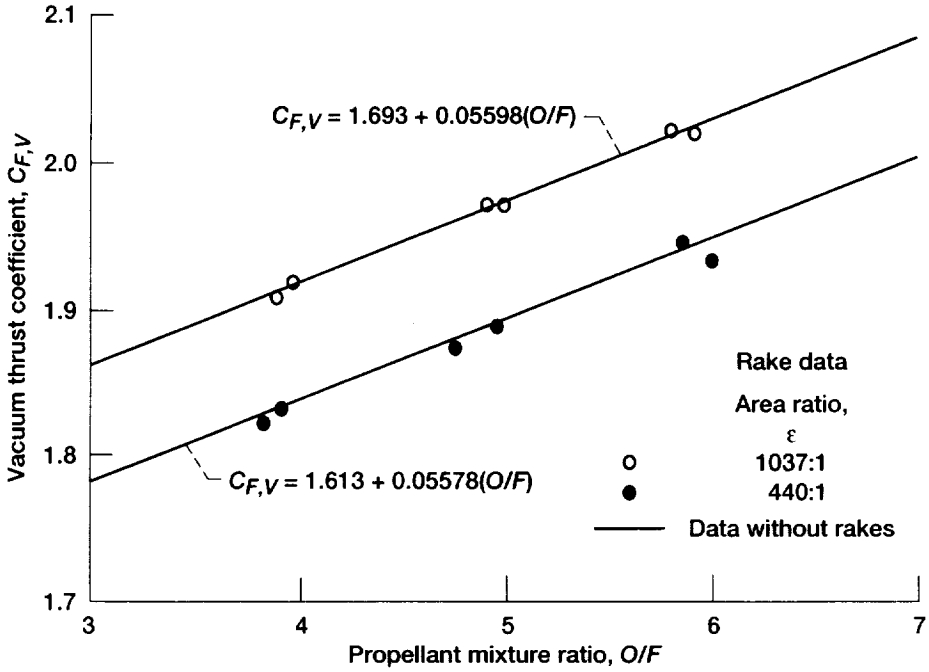

Figure 37.—Nozzle thrust performance as a function of mixture ratio for tests with the boundary layer rakes installed.

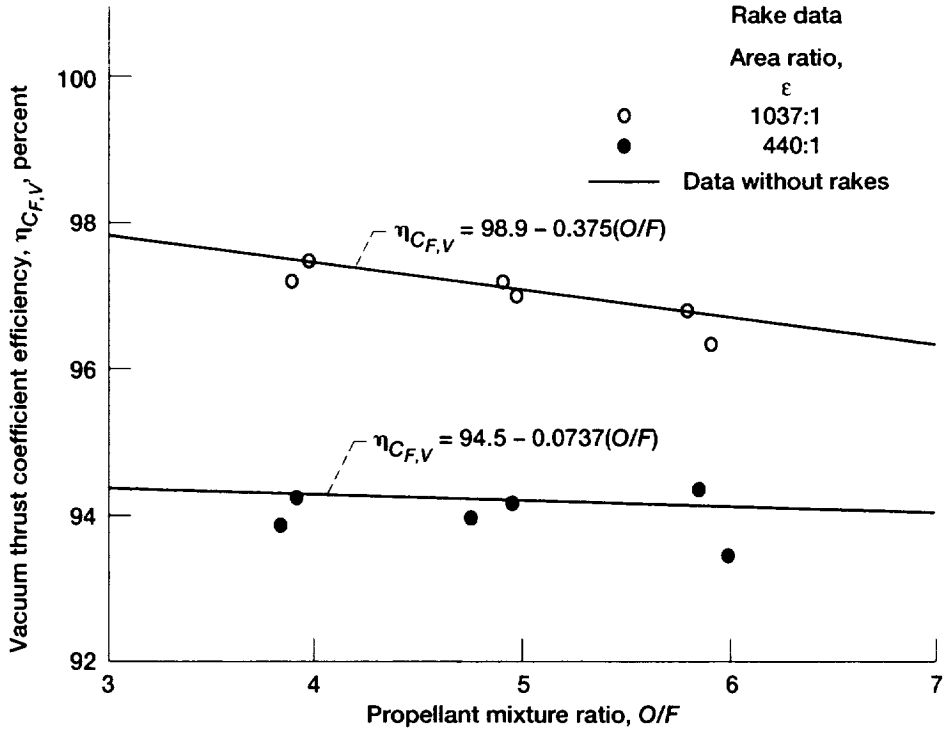

Figure 38.—Nozzle thrust coefficient efficiency as a function of mixture ratio for tests with the boundary layer rakes installed.

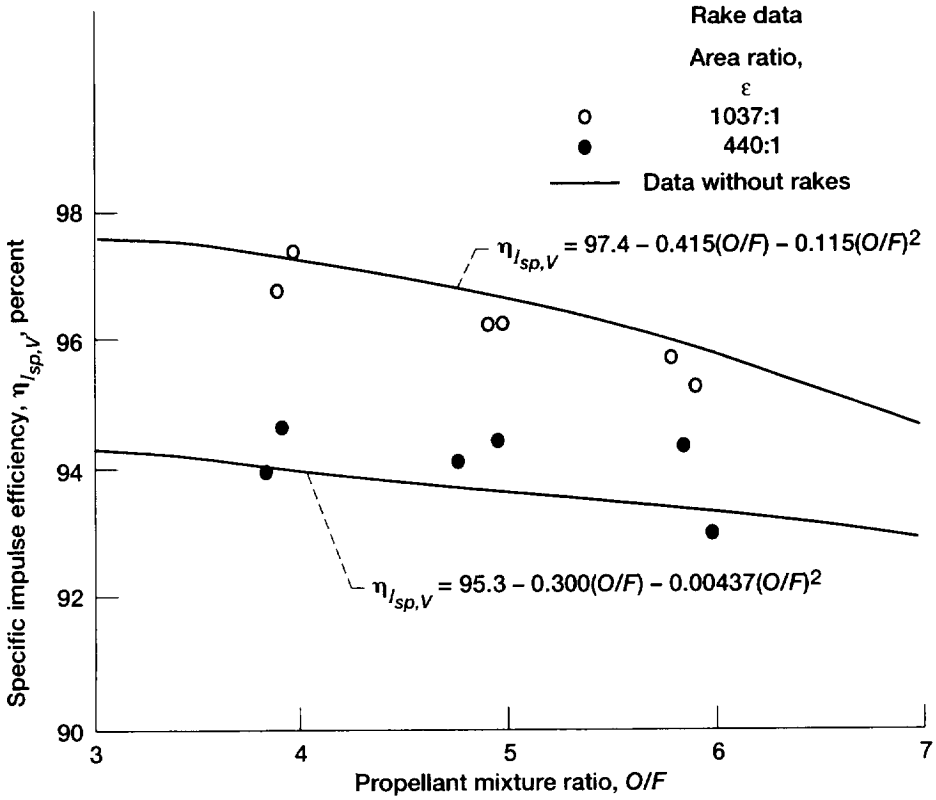

Figure 39.—Overall thruster efficiency as a function of mixture ratio for tests with the boundary layer rakes installed.

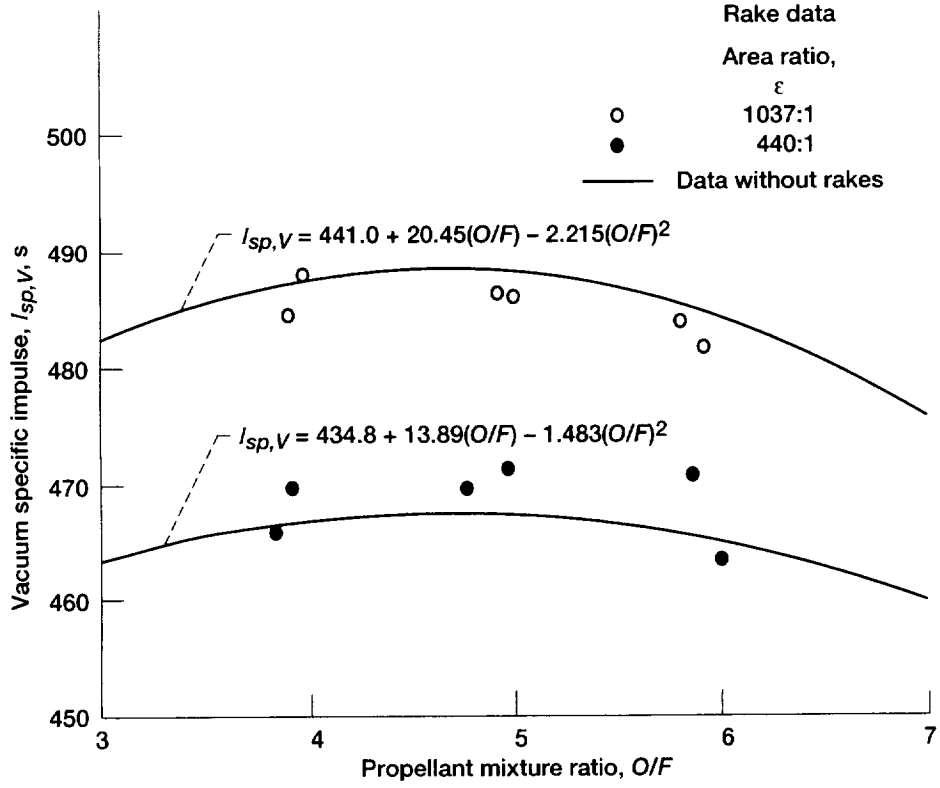

Figure 40.—Overall thruster performance as a function of mixture ratio for tests with the boundary layer rakes installed.

Overall performance of the thruster is illustrated by figure 39, which is a plot of $\eta_{I_{sp},V}$ as a function of *O/F*. Faired curves of the mean values of the previous firings are shown with the data points of table XIII superimposed; again, there is very good agreement within the scatter band. Figure 40 shows the actual specific impulse attained versus *O/F*. Here, the faired curve shows the mean values for the previous nonrake firings, and the individual data points are the values for firings with the rakes.

The total pressure measurements, along with pertinent test conditions, are listed in table XIV, which shows test results for both the 1037:1- and 440:1-area-ratio nozzles. Figure 41 shows a graphic illustration of the pressure profile measured for the 1037:1 configuration, along with bands of boundary layer thickness δ and displacement thickness δ^* from the TDK predictions. To avoid the scatter caused by slight variances in combustion chamber pressure among the six firings plotted, the measured total pressures were normalized by the combustion chamber pressure $P_{c,e}$, and the resultant pressure ratio was plotted versus the distance from the wall. The symbols for the data points are coded to indicate the nominal *O/F* for each point. A slight dependence on mixture ratio is evident in the distribution on the plot. Also evident is the consistent agreement of the data: all the data obtained in six separate firings with three different total pressure rakes defined the same total pressure

TABLE XIV.—EXPERIMENTALLY MEASURED BOUNDARY LAYER TOTAL PRESSURE

Reading	Nozzle exit expansion area ratio, ε	Effective combustion chamber total pressure at nozzle entrance,[a] $P_{c,e}$		Propellant mixture ratio, O/F	Rake total pressure			
					Tube A (1 in.)		Tube A (4 in.)	
					Exact area ratio of tube, 1019.6 (0.0440 in. from nozzle wall)		Exact area ratio of tube, 1019.7 (0.0655 in. from nozzle wall)	
		MPa	psia		kPa	psia	kPa	psia
589	1037	12.383	1796.5	3.97	------	------	9.263	1.344
592	↓	12.787	1855.1	5.91	------	------	8.546	1.240
593		12.484	1811.1	4.98	------	------	8.403	1.219
596		12.539	1819.1	4.91	5.714	0.829	------	------
597		12.421	1802.0	3.89	5.985	.868	------	------
598	↓	12.870	1867.1	5.80	5.692	.826	------	------
					Exact area ratio of tube, 418.7 (0.0680 in. from nozzle wall)		Exact area ratio of tube, 418.9 (0.0900 in. from nozzle wall)	
					kPa	psia	kPa	psia
607	440	12.684	1840.2	5.99	------	------	48.499	7.036
608	↓	12.458	1807.3	4.95	------	------	43.385	6.294
609		12.321	1787.4	3.91	------	------	38.842	5.635
612		12.760	1851.1	5.85	44.625	6.474	------	------
613		12.592	1826.8	4.76	43.564	6.320	------	------
614	↓	12.420	1801.8	3.84	43.154	6.261	------	------

Reading	Rake total pressure							
	Tube B (1 in.)		Tube C (1 in.)		Tube D (1 in.)		Tube B (4 in.)	
	Exact area ratio of tube, 1019.6 (0.0895 in. from nozzle wall)		Exact area ratio of tube, 1020.5 (0.3845 in. from nozzle wall)		Exact area ratio of tube, 1020.7 (0.4380 in. from nozzle wall)		Exact area ratio of tube, 1021.3 (0.6796 in. from nozzle wall)	
	kPa	psia	kPa	psia	kPa	psia	kPa	psia
589	------	------	------	------	------	------	22.177	3.217
592	------	------	------	------	------	------	20.969	3.042
593	------	------	------	------	------	------	20.758	3.011
596	11.084	1.608	17.653	2.561	19.575	2.840	------	------
597	11.429	1.658	18.073	2.622	20.221	2.934	------	------
598	11.091	1.609	18.122	2.629	19.679	2.855	------	------
	Exact area ratio of tube, 420.1 (0.2845 in. from nozzle wall)		Exact area ratio of tube, 421.0 (0.4195 in. from nozzle wall)		Exact area ratio of tube, 422.5 (0.6440 in. from nozzle wall)		Exact area ratio of tube, 422.9 (0.7045 in. from nozzle wall)	
	kPa	psia	kPa	psia	kPa	psia	kPa	psia
607	------	------	------	------	------	------	49.457	7.175
608	------	------	------	------	------	------	48.765	7.075
609	------	------	------	------	------	------	47.098	6.833
612	66.550	9.655	78.547	11.395	88.351	12.818	------	------
613	65.898	9.560	81.269	11.790	88.403	12.825	------	------
614	64.621	9.375	79.177	11.487	88.342	12.816	------	------

[a]Damaged tube.

TABLE XIV.—Concluded.

Reading	Rake total pressure							
	Tube E (1 in.)		Tube F (1 in.)		Tube G (1 in.)		Tube C (4 in.)	
	Exact area ratio of tube, 1021.5 (0.7535 in. from nozzle wall)		Exact area ratio of tube, 1021.7 (0.8240 in. from nozzle wall)		Exact area ratio of tube, 1022.4 (1.1280 in. from nozzle wall)		Exact area ratio of tube, 1022.9 (1.3135 in. from nozzle wall)	
	kPa	psia	kPa	psia	kPa	psia	kPa	psia
589	------	------	------	------	------	------	32.818	4.761
592	------	------	------	------	------	------	31.762	4.608
593	------	------	------	------	------	------	31.562	4.579
596	24.148	3.503	25.719	3.731	30.490	4.423	------	------
597	25.062	3.636	26.863	3.897	31.898	4.628	------	------
598	24.565	3.564	22.626	3.282	30.687	4.452	------	------
	Exact area ratio of tube, 423.1 (0.7455 in. from nozzle wall)		Exact area ratio of tube, 424.9 (1.0125 in. from nozzle wall)		Exact area ratio of tube, 425.3 (1.0805 in. from nozzle wall)		Exact area ratio of tube, 426.8 (1.2970 in. from nozzle wall)	
	kPa	psia	kPa	psia	kPa	psia	kPa	psia
607	------	------	------	------	------	------	61.990	8.993
608	------	------	------	------	------	------	59.774	8.672
609	------	------	------	------	------	------	58.040	8.420
612	88.322	12.813	52.079	[a]7.555	70.708	[a]10.258	------	------
613	55.122	7.997	25.719	[a]3.731	30.488	[a]4.423	------	------
614	56.512	8.199	51.215	[a]7.430	39.138	[a]5.678	------	------

Reading	Rake total pressure							
	Tube D (4 in.)		Tube E (4 in.)		Tube F (4 in.)		Tube G (4 in.)	
	Exact area ratio of tube, 1024.5 (1.9345 in. from nozzle wall)		Exact area ratio of tube, 1026.1 (2.5645 in. from nozzle wall)		Exact area ratio of tube, 1027.7 (3.1615 in. from nozzle wall)		Exact area ratio of tube, 1029.3 (3.7865 in. from nozzle wall)	
	kPa	psia	kPa	psia	kPa	psia	kPa	psia
589	38.169	5.537	32.911	4.775	31.239	4.532	28.477	4.131
592	36.235	5.257	30.381	4.408	31.069	4.507	28.727	4.168
593	36.281	5.263	31.744	4.605	30.946	4.490	28.290	4.104
596	------	------	------	------	------	------	------	------
597	------	------	------	------	------	------	------	------
598	------	------	------	------	------	------	------	------
	Exact area ratio of tube, 430.8 (1.9155 in. from nozzle wall)		Exact area ratio of tube, 435.0 (2.5375 in. from nozzle wall)		Exact area ratio of tube, 439.1 (3.1515 in. from nozzle wall)		Exact area ratio of tube, 443.2 (3.7625 in. from nozzle wall)	
	kPa	psia	kPa	psia	kPa	psia	kPa	psia
607	74.354	10.787	82.020	11.899	88.166	12.791	45.489	[a]6.599
608	77.799	11.287	83.583	12.126	88.192	12.795	44.363	[a]6.435
609	75.397	10.938	85.257	12.369	88.384	12.822	43.112	[a]6.254
612	------	------	------	------	------	------	------	------
613	------	------	------	------	------	------	------	------
614	------	------	------	------	------	------	------	------

[a]Damaged tube.

profile. Figure 42 illustrates the pressure profile obtained from the 440:1 configuration tests and shows bands of δ and δ^* from the TDK predictions. A slight dependence on mixture ratio is also evident here as is the consistent agreement of the six firings and three rakes, defining one total pressure profile at the 440:1 location.

For comparison, theoretical predictions were obtained from the TDK computer code for the 12 firings. A program option was used that provides the results that would be created downstream of a normal shock if a pitot tube was placed into the flow field. Table XV tabulates these results, and they are graphically displayed as solid lines in figures 41 and 42 for the 1037:1- and 440:1-expansion-area-ratio nozzles, respectively. As figures 41 and 42 illustrate, there is good agreement between the experimental results and the analytical predictions for the first 2.54 cm (1.0 in.) and 1.27 cm (0.5 in.) in the 1037:1 and 440:1 nozzles, respectively. However, the TDK code overpredicted the measured free-stream pressure at both axial locations, perhaps because of combustion or shock losses in the nozzle. The free-stream pressure in these exit planes is a function of the radius, making it difficult to sort out experimentally the free-stream viscous pressure loss from the shock and combustion losses and making it difficult to measure the edge of the boundary layer. It is impossible to translate the measured global combustion losses into the local-exit-plane pressure losses. The experimental results indicate very little variation

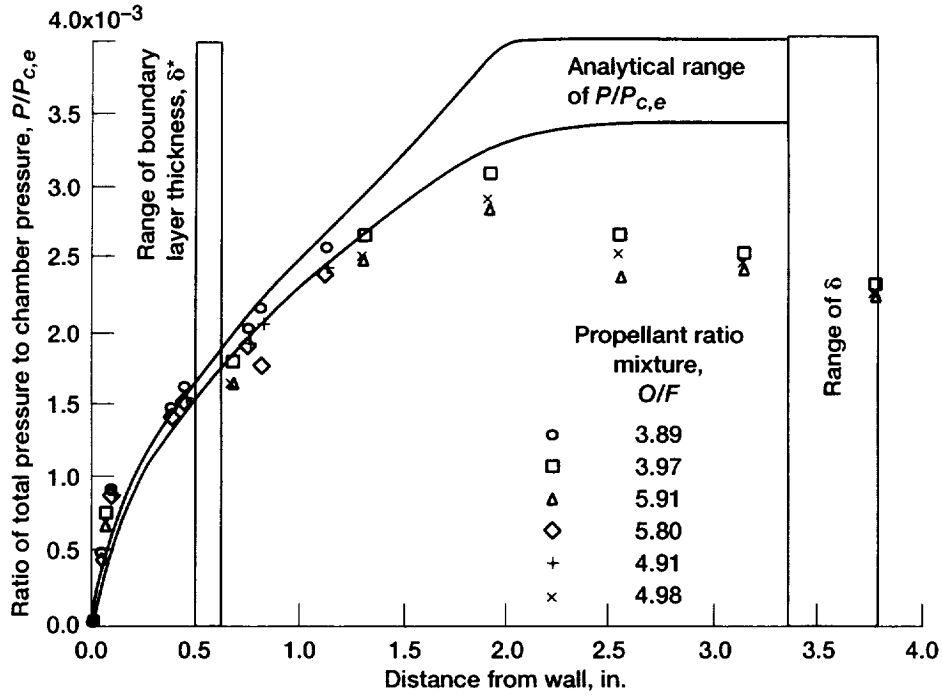

Figure 41.—Analytical and experimental $P/P_{c,e}$ comparison. Area ratio, ε, 1037:1.

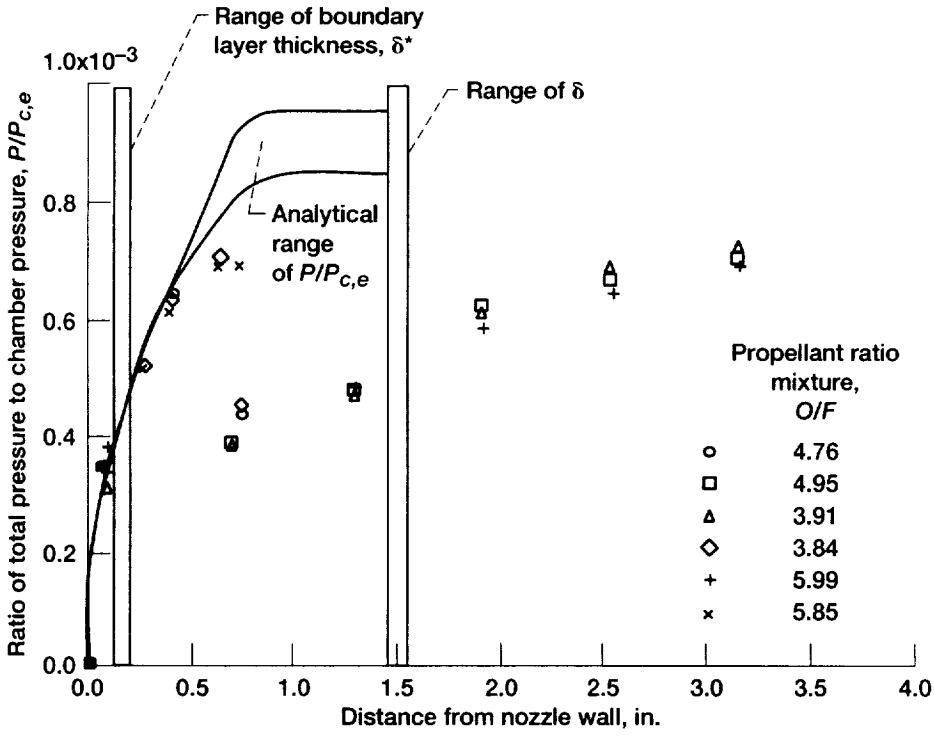

Figure 42.—Analytical and experimental $P/P_{c,e}$ comparison. Area ratio, ε, 440:1.

TABLE XV.—TDK/MABL PREDICTIONS OF BOUNDARY LAYER TOTAL PRESSURE

Reading	Nozzle exit expansion area ratio, ε	Effective combustion chamber total pressure at nozzle entrance,[a] $P_{c,e}$		Propellant mixture ratio, O/F	TDK/MABL rake total pressure predictions			
					Tube A (1 in.)		Tube A (4 in.)	
					Exact area ratio of tube, 1019.6 (0.0440 in. from nozzle wall)		Exact area ratio of tube, 1019.7 (0.0655 in. from nozzle wall)	
		MPa	psia		kPa	psia	kPa	psia
589	1037	12.383	1796.5	3.97	------	------	6.757	0.980
592	↓	12.787	1855.1	5.91	------	------	7.631	1.107
593		12.484	1811.1	4.98	------	------	7.118	1.033
596		12.539	1819.1	4.91	5.185	0.752	------	------
597		12.421	1802.0	3.89	4.853	.704	------	------
598	↓	12.870	1867.1	5.80	5.347	.776	------	------
					Exact area ratio of tube, 418.7 (0.0680 in. from nozzle wall)		Exact area ratio of tube, 418.9 (0.0900 in. from nozzle wall)	
					kPa	psia	kPa	psia
607	440	12.684	1840.2	5.99	------	------	48.051	6.971
608	↓	12.458	1807.3	4.95	------	------	45.514	6.603
609		12.321	1787.4	3.91	------	------	44.391	6.440
612		12.760	1851.1	5.85	43.054	6.246	------	------
613		12.592	1826.8	4.76	40.689	5.903	------	------
614	↓	12.420	1801.8	3.84	38.835	5.634	------	------

Reading	TDK/MABL rake total pressure predictions							
	Tube B (1 in.)		Tube C (1 in.)		Tube D (1 in.)		Tube B (4 in.)	
	Exact area ratio of tube, 1019.6 (0.0895 in. from nozzle wall)		Exact area ratio of tube, 1020.5 (0.3845 in. from nozzle wall)		Exact area ratio of tube, 1020.7 (0.4380 in. from nozzle wall)		Exact area ratio of tube, 1021.3 (0.6796 in. from nozzle wall)	
	kPa	psia	kPa	psia	kPa	psia	kPa	psia
589	------	------	------	------	------	------	24.346	3.532
592	------	------	------	------	------	------	24.525	3.558
593	------	------	------	------	------	------	24.098	3.496
596	9.002	1.306	18.935	2.747	19.933	2.892	------	------
597	8.561	1.242	18.500	2.684	19.583	2.841	------	------
598	9.308	1.350	19.414	2.817	20.371	2.955	------	------
	Exact area ratio of tube, 420.1 (0.2845 in. from nozzle wall)		Exact area ratio of tube, 421.0 (0.4195 in. from nozzle wall)		Exact area ratio of tube, 422.5 (0.6440 in. from nozzle wall)		Exact area ratio of tube, 422.9 (0.7045 in. from nozzle wall)	
	kPa	psia	kPa	psia	kPa	psia	kPa	psia
607	------	------	------	------	------	------	101.437	14.716
608	------	------	------	------	------	------	104.643	15.181
609	------	------	------	------	------	------	111.232	16.137
612	70.922	10.289	82.826	12.016	98.742	14.325	------	------
613	70.129	10.174	83.536	12.119	102.313	14.843	------	------
614	69.895	10.140	82.578	11.980	106.842	15.500	------	------

[a]Outside of theoretical boundary layer.

TABLE XV.—Concluded.

Reading	TDK/MABL rake total pressure predictions							
	Tube E (1 in.)		Tube F (1 in.)		Tube G (1 in.)		Tube C (4 in.)	
	Exact area ratio of tube, 1021.5 (0.7535 in. from nozzle wall)		Exact area ratio of tube, 1021.7 (0.8240 in. from nozzle wall)		Exact area ratio of tube, 1022.4 (1.1280 in. from nozzle wall)		Exact area ratio of tube, 1022.9 (1.3135 in. from nozzle wall)	
	kPa	psia	kPa	psia	kPa	psia	kPa	psia
589	------	------	------	------	------	------	36.650	5.317
592	------	------	------	------	------	------	34.113	4.949
593	------	------	------	------	------	------	34.688	5.032
596	25.621	3.717	26.862	3.897	32.025	4.646	------	------
597	25.980	3.769	27.413	3.977	33.403	4.846	------	------
598	25.704	3.729	26.848	3.895	31.570	4.580	------	------
	Exact area ratio of tube, 423.1 (0.7455 in. from nozzle wall)		Exact area ratio of tube, 424.9 (1.0125 in. from nozzle wall)		Exact area ratio of tube, 425.3 (1.0805 in. from nozzle wall)		Exact area ratio of tube, 426.8 (1.2970 in. from nozzle wall)	
	kPa	psia	kPa	psia	kPa	psia	kPa	psia
607	------	------	------	------	------	------	61.990	8.993
608	------	------	------	------	------	------	59.774	8.672
609	------	------	------	------	------	------	58.040	8.420
612	104.774	15.200	(a)	(a)	(a)	(a)	------	------
613	109.082	15.825	(a)	(a)	(a)	(a)	------	------
614	115.044	16.690	(a)	(a)	(a)	(a)	------	------

Reading	TDK/MABL rake total pressure predictions							
	Tube D (4 in.)		Tube E (4 in.)		Tube F (4 in.)		Tube G (4 in.)	
	Exact area ratio of tube, 1024.5 (1.9345 in. from nozzle wall)		Exact area ratio of tube, 1026.1 (2.5645 in. from nozzle wall)		Exact area ratio of tube, 1027.7 (3.1615 in. from nozzle wall)		Exact area ratio of tube, 1029.3 (3.7865 in. from nozzle wall)	
	kPa	psia	kPa	psia	kPa	psia	kPa	psia
589	47.624	6.909	49.457	7.175	49.361	7.161	(a)	(a)
592	42.027	6.097	43.771	6.350	43.660	6.334	(a)	(a)
593	43.908	6.370	45.742	6.636	45.701	6.630	(a)	(a)
596	------	------	------	------	------	------	------	------
597	------	------	------	------	------	------	------	------
598	------	------	------	------	------	------	------	------
	Exact area ratio of tube, 430.8 (1.9155 in. from nozzle wall)		Exact area ratio of tube, 435.0 (2.5375 in. from nozzle wall)		Exact area ratio of tube, 439.1 (3.1515 in. from nozzle wall)		Exact area ratio of tube, 443.2 (3.7625 in. from nozzle wall)	
	kPa	psia	kPa	psia	kPa	psia	kPa	psia
607	(a)	(a)	(a)	(a)	(a)	(a)	(a)	(a)
608	(a)	(a)	(a)	(a)	(a)	(a)	(a)	(a)
609	(a)	(a)	(a)	(a)	(a)	(a)	(a)	(a)
612	------	------	------	------	------	------	------	------
613	------	------	------	------	------	------	------	------
614	------	------	------	------	------	------	------	------

[a]Outside of theoretical boundary layer.

due to mixture ratio; they show a sudden drop in pressure and then a gradual asymptote to some core flow value. The analytical predictions, however, indicate a larger variation in the total pressure profile due to mixture ratio and also indicate a seemingly sharp knee where they asymptote to some significantly higher core flow value. The code seems to overpredict the boundary layer thickness.

Within measurement accuracy, these data suggest a turbulent boundary layer profile. However, a subtle profile change developed between the 440:1 position and 1037:1, indicating that the near-wall profile was becoming more laminarlike, possibly in a relaminarization process caused by the highly favorable pressure gradient or, perhaps, as a laminar sublayer. This process, which the code did not predict, would account for the experimental performance and heat-transfer data falling between laminar and turbulent predictions. Predicting the measure of laminarization then becomes important for predicting performance where laminar and turbulent predictions vary 3 percent, and it becomes critical to predicting heat transfer where experimental measurements and laminar and turbulent predictions vary approximately 100 percent.

Concluding Remarks

The results show that, based on the assumption of turbulent flow due to the throat Reynolds number, the TDK code predicts performance better for the 440:1-nozzle configuration. Reference 6 results are considered to have validated the TDK/MABL code up to an area ratio of 300:1. Therefore, on the basis of the current results and previous work, it would be reasonable to conclude that the TDK/MABL code is validated up to an area ratio of 440:1. The results from the TDK turbulent model provide a nearly 2-percent overprediction of experimental results at an area ratio of 1025:1 and only an approximately 0.5-percent underprediction from the TDK laminar model. However, the TDK turbulent model underpredicted performance by only 0.25 percent for an area ratio of 440:1, whereas the TDK laminar prediction was nearly 2.0-percent higher than experimental results. Although a 2-percent difference between the turbulent prediction and experiment is not desirable at the 1025:1 area ratio, it is better to have a code that underpredicts performance rather than one that is overly optimistic. Because the code seems to underpredict performance at high area ratios, it is possible that the boundary layer growth is overstated. As the boundary layer grows, it reduces the inviscid core size, which might result in lower-than-expected predicted performance. The exact nature of the boundary layer flow phenomena is still one of the least understood and most difficult portions to model of any nozzle flow. Variations in the boundary model have generally been thought of as small for performance calculations; but for high-area-ratio nozzles, that is not the case.

Summary of Results

Experimentally attained rocket performance was compared with the current JANNAF methodology of performance prediction. A gaseous hydrogen and liquid oxygen rocket thruster with a 1-in.-diameter throat was test fired at altitude, and the thrust performance, heat transfer rate, and total pressure profiles were measured. Firings with both a 1025:1 and a truncated 440:1-expansion-area-ratio configuration were compared with the predictions. The test firings were at combustion chamber pressures of 1800 to 2400 psia, and at propellant mixture ratios of 3.9 to 6.0. The Reynolds number, based on throat diameter, of the flow through the throat was 1.43×10^6 to 2.05×10^6, depending on the mixture ratio and combustion chamber pressure.

Two performance predictions were made with the TDK computer code for each of the firings, one each with the BLM boundary layer module and the MABL boundary layer module. Differences between the turbulent BLM and MABL results proved insignificant, and further discussion was limited to the MABL results. Results were also compared with predictions using the laminar boundary layer model in the MABL module. Comparisons of predicted performance to experimentally attained thrust performance indicated that the experimentally attained performance was approximately 2.0-percent higher than the turbulent prediction and approximately 0.5-percent lower than the laminar prediction for the 1025:1 configurations. However, for the 440:1 configuration, the experimentally attained performance was approximately 0.25-percent higher than the turbulent prediction and approximately 2.0-percent lower than the laminar prediction.

Nozzle wall temperatures were measured on the outside of a thin-walled heat sink nozzle during the test firings. Nozzle heat fluxes were calculated from the time histories of these temperatures. Values of the integral of heat flux as a function of nozzle surface area were also calculated. So that they could be directly compared with the analytical predictions, the experimental values were adjusted in a number of ways. The heat flux, heat rate per unit length, and heat rate values were adjusted to what they would have been with complete combustion by the square of the characteristic exhaust velocity efficiency $(\eta_{C^*})^2$. The heat rate values were adjusted to a uniform combustion chamber pressure P_c of 2063.1 psia (reading 577) by the factor $(P_c)^{0.8}$. As a result, two systematic causes of data scatter were reconciled, and true variations in heat transfer as a result of other functions became obvious. A comparison of experimental heat rate to the analytical predicted values shows a very similar *O/F* dependence, although the experimental values are lower than the predicted values. This shortfall of experimentally measured heat transfer is also evident in the comparison of the experiment to the analysis of heat flux and heat rate per axial length.

A separate series of high-pressure rocket nozzle firings were conducted to document the boundary layer profile of a high-area-ratio nozzle. The nozzles had expansion area-ratios of 1037:1 and 440:1 with a nominal throat diameter of 2.54 cm (1.0 in.). Characteristic exhaust velocity, nozzle thrust coefficient, and thruster specific impulse were determined and compared with nearly identical firings without boundary layer rakes to ensure applicability. As indicated by a comparison of boundary layer total pressure profiles and analytical predictions, there was good agreement for 0.5 in. from the nozzle wall; but the further into the core that flow measurements were taken, the more TDK overpredicted the boundary layer thickness. Several possible explanations exist, such as the possibility of relaminarization due to the highly favorable pressure gradient, the size of the laminar sublayer, or the type of turbulence waves present; however, more investigation is required. The difference between measured and predicted freestream pressures also indicates that local flow properties are significantly affected by combustion efficiency and shock losses. The current methodology does not account for this process, which may be a key to improving high-area-ratio performance predictions.

Glenn Research Center
National Aeronautics and Space Administration
Cleveland, Ohio, March 31, 1999

Appendix A

Symbols

A_{ex}	nozzle exit area, m^2 ($in.^2$)
A_s	nozzle surface area, m^2 ($in.^2$)
A_t	nozzle throat area, m^2 ($in.^2$)
A_v	venturi throat area, m^2 ($in.^2$)
C_d	venturi discharge coefficient, dimensionless
$C_{F,V}$	vacuum thrust coefficient, dimensionless
$C_{F,V,Th(ODE)}$	theoretical, one-dimensional-equilibrium (ODE) vacuum thrust coefficient (obtained from the Chemical Equilibrium Composition (CEC) program), dimensionless
$C_{F,V,Th(TDK)}$	theoretical, two-dimensional-kinetics (TDK) vacuum thrust coefficient, dimensionless
C^*	characteristic exhaust velocity, m/s (ft/s)
$C^*_{Th(ODE)}$	theoretical, one-dimensional-equilibrium characteristic exhaust velocity (obtained from the CEC program), m/s (ft/s)
D_i	diameter, m (in.)
F	thrust (corrected for aneroid effect), N (lb_f)
F_v	vacuum thrust (experimentally measured thrust corrected to vacuum conditions), N (lb_f)
g	acceleration due to gravity, 9.807 m/s^2 (32.174 ft/s^2)
g_c	proportionality constant, 1 kg-m/N-s^2 (32.2 lb_m-ft/lb_f-s^2)
I	theoretical subsonic specific impulse inside combustion chamber (obtained from the CEC program), N-s/kg (lb_f-s/lb_m)
$I_{sp,V}$	vacuum specific impulse, N-s/kg (lb_f-s/lb_m)
$I_{sp,V,Th(ODE)}$	theoretical, one-dimensional equilibrium vacuum specific impulse (obtained from the CEC program), N-s/kg (lb_f-s/lb_m)
k	conductivity, W/m-K (Btu/sec-in.-°F)
L_1	starting axial position, m (in.)
L_2	ending axial position, m (in.)
$\dot{m}$	propellant mass flow
O/F	propellant mixture ratio (oxidizer flow divided by fuel flow), dimensionless
P_a	ambient pressure in test capsule, kPa (psia)
P_c	chamber pressure
$P_{c,a}$	static pressure at injector end of combustion chamber, MPa (psia)
$P_{c,e}$	effective combustion chamber total pressure at nozzle entrance, MPa (psia)
$P_{c,T}$	combustion chamber total pressure after combustion ($P_{c,a}$ corrected for momentum pressure loss), MPa (psia)
P_{fi}	fuel injection pressure, MPa (psia)
P_{oi}	oxidizer injection pressure, MPa (psia)
P_s	static pressure in nozzle, kPa (psia)
P_s/P_T	static-to-total pressure ratio in combustion chamber (obtained from the CEC program), dimensionless
Q	heat rate, W (Btu/sec)
q_i''	heat flux to inner wall of nozzle, W/m^2 ($Btu/in.^2$-sec)
Re_θ	Reynolds number based on momentum thickness
R_i	local nozzle inner wall radius, m (in.)
R_o	local nozzle outer wall radius, m (in.)
T	temperature, K (°R)

T_{fi}	fuel injection temperature, K (°R)
T_i	nozzle inner wall temperature, K (°R)
T_o	nozzle outer wall temperature, K (°R)
T_{oi}	oxidizer injection temperature, K (°R)
t	time, sec
V	velocity through venturi throat, m/s (in./s)
V_{av}	mass-averaged injection velocity of propellants, m/s (ft/s)
α	diffusivity, m^2/s
ΔP	nominal pressure drop, kPa (psid)
δ	boundary layer thickness, cm (in.)
δ^*	boundary layer displacement thickness, cm (in.)
ε	nozzle exit expansion area ratio, A_{ex}/A_t, dimensionless
ε_c	thruster contraction area ratio, dimensionless
η_{C^*}	characteristic exhaust velocity efficiency, percent
$\eta_{C_{F,V}}$	vacuum thrust coefficient efficiency, percent
$\eta_{I_{sp,V}}$	vacuum specific impulse efficiency, percent
ρ	fluid density, kg/m^3 ($lb_m/in.^3$)
σ	standard deviation, dimensionless
θ	angle between nozzle wall and axis, deg

Appendix B

Laminar Boundary Layer Results

Table XVI presents the TDK/MABL predictions with the laminar boundary layer condition, and table XVII compares the laminar boundary layer heat flux results with the TDK/MABL predictions.

TABLE XVI.—TDK/MABL LAMINAR PREDICTIONS

Reading	Nozzle exit expansion area ratio, ε	Effective combustion chamber total pressure at nozzle entrance, $P_{c,e}$		Propellant mixture ratio, O/F	Predicted propellant flow rate	
		MPa	psia		kg/s	lb_m/s
569	1025	12.326	1787.7	3.89	2.4926	5.4961
570	↓	12.645	1834.0	5.97	2.7093	5.9740
571		12.488	1811.1	4.70	2.5718	5.6709
575		14.350	2081.2	4.65	2.9511	6.5071
576		14.605	2118.2	5.68	3.0960	6.8266
577		14.225	2063.1	4.47	2.9114	6.4196
580	↓	16.364	2373.3	4.27	3.3321	7.3472
601	440	12.768	1851.8	6.15	2.7196	5.9968
602	↓	12.542	1819.0	5.11	2.5830	5.6955
603		12.457	1806.7	4.01	2.4944	5.5001

Reading	Nozzle exit expansion area ratio, ε	Computer code					
		TDK/MABL Laminar					
		Predicted characteristic exhaust velocity, C^*		Predicted vacuum thrust, F_V		Predicted vacuum thrust coefficient, $C_{F,V}$	Predicted vacuum thrust coefficient efficiency, $\eta_{C_{F,V}}$ percent
		m/s	ft/s	N	lb_f		
569	1025	2505.14	8219.37	11975	2692.29	1.92	97.73
570	↓	2364.44	7757.74	13088	2942.47	2.04	97.32
571		2459.70	8070.27	12432	2795.05	1.96	97.61
575		2463.32	8082.16	14271	3208.30	1.96	97.75
576		2389.69	7840.57	14995	3371.15	2.03	97.56
577		2475.18	8121.07	14070	3163.33	1.95	97.76
580	↓	2487.78	8162.41	16094	3618.23	1.94	97.84
601	440	2349.84	7709.83	12733	2862.63	1.99	95.77
602	↓	2430.36	7974.01	12137	2728.56	1.93	95.93
603		2499.57	8201.08	11670	2623.55	1.87	95.96

TABLE XVI.—Concluded.

Reading	Nozzle exit expanison area ratio, ε	Computer code					
		ODE	ODK	MOC	TDK/MABL Laminar		
					Predicted vacuum specific impulse, $I_{sp,v}$, sec	Predicted vacuum specific impulse (adjusted), $I_{sp,v}$, sec	Predicted vacuum specific impulse efficiency (adjusted), $\eta_{I_{sp,v}}$, percent
569	1025	500.63	499.61	494.93	489.86	488.97	97.67
570	↓	505.53	502.12	498.62	492.55	487.97	96.53
571		504.43	502.71	498.44	492.88	491.16	97.37
575		503.90	502.51	498.18	493.05	491.41	97.52
576		505.55	503.09	499.37	493.83	490.05	96.94
577		503.48	502.22	497.79	492.75	491.35	97.59
580	↓	502.54	501.62	497.07	492.46	491.29	97.76
601	440	497.81	494.36	482.12	477.36	472.40	94.90
602	↓	498.99	496.98	483.61	479.07	476.72	95.54
603		496.58	495.52	481.11	477.00	476.06	95.87

TABLE XVII.—EXPERIMENTAL (η_{c^*} = 100 PERCENT) AND TDK/MABL LAMINAR HEAT FLUX DISTRIBUTIONS

Reading	Effective combustion chamber total pressure at nozzle entrance, $P_{c,e}$		Propellant mixture ratio, O/F	Expansion area ratio, ε					
				50		100		200	
				Heat flux to nozzle wall					
	MPa	psia		kW/m^2	Btu/in.^{2}-s	kW/m^2	Btu/in.^{2}-s	kW/m^2	Btu/in.^{2}-s
Experimental adjusted to η_{c^*} = 100 percent									
569	12.326	1787.7	3.89	1428.00	0.8738	774.80	0.4741	413.46	0.2530
570	12.645	1834.0	5.97	1857.97	1.1369	1025.82	.6277	538.48	.3295
571	12.488	1811.1	4.70	1643.72	1.0058	902.76	.5524	470.83	.2881
575	14.350	2081.2	4.65	1815.81	1.1111	1009.31	.6176	547.80	.3352
576	14.605	2118.2	5.68	2013.55	1.2321	1117.66	.6839	598.62	.3663
577	14.225	2063.1	4.47	1621.66	.9923	942.47	.5767	491.58	.3008
580	16.364	2373.3	4.27	1856.50	1.1360	1070.43	.6550	588.98	.3604
TDK/MABL laminar									
569	12.326	1787.7	3.89	536.69	0.3284	312.47	0.1912	173.23	0.1060
570	12.645	1834.0	5.97	745.71	.4563	462.00	.2827	255.76	.1565
571	12.488	1811.1	4.70	598.13	.3660	367.22	.2247	201.50	.1233
575	14.350	2081.2	4.65	630.00	.3855	389.77	.2385	216.86	.1327
576	14.605	2118.2	5.68	755.68	.4624	467.39	.2860	263.11	.1610
577	14.225	2063.1	4.47	605.16	.3703	365.58	.2237	203.30	.1244
580	16.364	2373.3	4.27	611.37	.3741	384.86	.2355	215.23	.1317

Reading	Expansion area ratio, ε											
	300		388		500		635		800		975	
	Heat flux to nozzle wall											
	kW/m^2	Btu/in.^{2}-s	kW/m^2	Btu/in.^{2}-s	kW/m^2	Btu/in.^{2}-s	kW/m^2	Btu/in.^{2}-s	kW/m^2	Btu/in.^{2}-s	kW/m^2	Btu/in.^{2}-s
Experimental adjusted to η_{c^*} = 100 percent												
569	297.92	0.1823	239.42	0.1465	180.91	0.1107	153.13	0.0937	143.49	0.0878	122.24	0.0748
570	378.33	.2315	297.76	.1822	220.79	.1351	170.78	.1045	133.84	.0819	111.62	.0683
571	336.16	.2057	267.04	.1634	200.69	.1228	155.74	.0953	126.33	.0773	103.77	.0635
575	384.70	.2354	302.50	.1851	225.36	.1379	178.30	.1091	140.38	.0859	118.97	.0728
576	414.12	.2534	327.67	.2005	243.50	.1490	189.90	.1162	145.77	.0892	124.20	.0760
577	353.00	.2160	279.95	.1713	209.18	.1280	166.20	.1017	136.62	.0836	118.32	.0724
580	411.67	.2519	327.34	.2003	245.79	.1504	189.25	.1158	148.55	.0909	127.47	.0780
TDK/MABL laminar												
569	117.18	0.0717	91.52	0.0560	69.62	0.0426	52.79	0.0323	40.20	0.0246	31.87	0.0195
570	173.23	.1060	132.86	.0813	103.28	.0632	78.61	.0481	59.16	.0362	46.58	.0285
571	137.77	.0843	106.88	.0654	80.73	.0494	62.59	.0383	46.74	.0286	37.59	.0230
575	148.55	.0909	114.07	.0698	88.09	.0539	67.49	.0413	50.50	.0309	39.55	.0242
576	178.13	.1090	136.13	.0833	106.39	.0651	80.73	.0494	60.96	.0373	48.05	.0294
577	138.09	.0845	106.72	.0653	83.18	.0509	64.23	.0393	47.88	.0293	37.91	.0232
580	146.76	.0898	113.42	.0694	87.76	.0537	67.00	.0410	50.50	.0309	40.20	.0246

REPORT DOCUMENTATION PAGE

Form Approved
OMB No. 0704-0188

1. AGENCY USE ONLY (Leave blank)	2. REPORT DATE	3. REPORT TYPE AND DATES COVERED
	June 1999	Technical Paper

4. TITLE AND SUBTITLE

High-Area-Ratio Rocket Nozzle at High Combustion Chamber Pressure—Experimental and Analytical Validation

5. FUNDING NUMBERS

WU–632–1B–1B–00

6. AUTHOR(S)

Robert S. Jankovsky, Timothy D. Smith, and Albert J. Pavli

7. PERFORMING ORGANIZATION NAME(S) AND ADDRESS(ES)

National Aeronautics and Space Administration
John H. Glenn Research Center at Lewis Field
Cleveland, Ohio 44135–3191

8. PERFORMING ORGANIZATION REPORT NUMBER

E–11265

9. SPONSORING/MONITORING AGENCY NAME(S) AND ADDRESS(ES)

National Aeronautics and Space Administration
Washington, DC 20546–0001

10. SPONSORING/MONITORING AGENCY REPORT NUMBER

NASA TP—1999-208522

11. SUPPLEMENTARY NOTES

Robert S. Jankovsky and Timothy D. Smith, NASA Glenn Research Center; Albert S. Pavli, NYMA, Inc., 2001 Aerospace Parkway, Brook Park, Ohio 44142. Responsible person, Robert S. Jankovsky, organization code 5430, (216) 977–7515.

12a. DISTRIBUTION/AVAILABILITY STATEMENT

Unclassified - Unlimited
Subject Category: 20 Distribution: Standard

This publication is available from the NASA Center for AeroSpace Information, (301) 621–0390.

12b. DISTRIBUTION CODE

13. ABSTRACT ***(Maximum 200 words)***

Experimental data were obtained on an optimally contoured nozzle with an area ratio of 1025:1 and on a truncated version of this nozzle with an area ratio of 440:1. The nozzles were tested with gaseous hydrogen and liquid oxygen propellants at combustion chamber pressures of 1800 to 2400 psia and mixture ratios of 3.89 to 6.15. This report compares the experimental performance, heat transfer, and boundary layer total pressure measurements with theoretical predictions of the current Joint Army, Navy, NASA, Air Force (JANNAF) developed methodology. This methodology makes use of the Two-Dimensional Kinetics (TDK) nozzle performance code. Comparisons of the TDK-predicted performance to experimentally attained thrust performance indicated that both the vacuum thrust coefficient and the vacuum specific impulse values were approximately 2.0-percent higher than the turbulent prediction for the 1025:1 configurations, and approximately 0.25-percent higher than the turbulent prediction for the 440:1 configuration. Nozzle wall temperatures were measured on the outside of a thin-walled heat sink nozzle during the test firings. Nozzle heat fluxes were calculated from the time histories of these temperatures and compared with predictions made with the TDK code. The heat flux values were overpredicted for all cases. The results range from nearly 100 percent at an area ratio of 50 to only approximately 3 percent at an area ratio of 975. Values of the integral of the heat flux as a function of nozzle surface area were also calculated. Comparisons of the experiment with analyses of the heat flux and the heat rate per axial length also show that the experimental values were lower than the predicted value. Three boundary layer rakes mounted on the nozzle exit were used for boundary layer measurements. This arrangement allowed total pressure measurements to be obtained at 14 different distances from the nozzle wall. A comparison of boundary layer total pressure profiles and analytical predictions show good agreement for the first 0.5 in. from the nozzle wall; but the further into the core flow that measurements were taken, the more that TDK overpredicted the boundary layer thickness.

14. SUBJECT TERMS	15. NUMBER OF PAGES
Rocket engines; Rocket nozzles	57
	16. PRICE CODE: A04

17. SECURITY CLASSIFICATION OF REPORT	18. SECURITY CLASSIFICATION OF THIS PAGE	19. SECURITY CLASSIFICATION OF ABSTRACT	20. LIMITATION OF ABSTRACT
Unclassified	Unclassified	Unclassified	

References

1. JANNAF Rocket Engine Performance Prediction and Evaluation Manual. CPIA–PUBL–246. Chemical Propulsion Information Agency, 1975.
2. Nickerson, G.R., et al: Two-Dimensional Kinetics (TDK) Nozzle Performance Computer Program, Vol. I, Engineering Methods. SN130, Software and Engineering Associates, Inc., NASA Contract NAS8–39048, March 31, 1993.
3. Smith, T.A.; Pavli, A.J.; and Kacynski, K.J.: Comparison of Theoretical and Experimental Thrust Performance of a 1030:1 Area Ratio Rocket Nozzle at a Chamber Pressure of 2413 kN/m^2 (350 psia). AIAA Paper 87–2069 (NASA TP–2725), August 1987.
4. Pavli, A.J.; Kacynski, K.J.; and Smith, T.A.: Experimental Thrust Performance of a High-Area-Ratio Rocket Nozzle. NASA TP–2720, 1987.
5. Kacynski, K.J.; Pavli, A.J.; and Smith, T.A.: Experimental Evaluation of Heat Transfer on a 1030:1 Area Ratio Rocket Nozzle. AIAA Paper 87–2070 (NASA TP–2726), 1987.
6. Dang, A.L.; and Nickerson, G.R.: A Computer Program for Performance Prediction of Tripropellant Rocket Engines With Tangential Slot Injection. 24th JANNAF Combustion Meeting, Vol. II, 1987.
7. Miyajima, H.; and Nakahashi, K.: Performance of a Low Thrust LO_2/LH_2 Engine With a 300:1 Area Ratio Nozzle. AIAA Paper 83–1313, 1983.
8. Jankovsky, R.S.; Kazaroff, J.M.; and Pavli, A.J.: Experimental Performance of a High-Area-Ratio Rocket Nozzle at High Combustion Chamber Pressure. NASA TP–3576, 1996. (Available online: http://gltrs.grc.nasa.gov/cgi-bin/GLTRS/browse.pl?1996/TP-3576.html)
9. Schoenman, L.: Low-Thrust Isp Sensitivity Study. NASA CR–165621, 1982.
10. Rao, G.V.R.: Optimum Thrust Performance of Contoured Nozzles. Chemical Propulsion Information Agency, JANNAF Liquid Propulsion Group, 1st Meeting, Nov. 1959, pp. 243–259.
11. Nickerson, G.R.; Dang, A.L.; and Dunn, S.S.: The Rao Method Optimum Nozzle Contour Program. NAS8–36863, Feb. 15, 1988.
12. Nickerson, G.R., et al.: Two-Dimensional Kinetics (TDK) Nozzle Performance Computer Program, Vol. III, Users Manual. NAS8–39048, March 31, 1993.
13. Keller, H.B.; and Cebeci, T.: Accurate Numerical Methods for Boundary-Layer Flows II: Two-Dimensional Turbulent Flows. AIAA J., vol. 10, no. 9, Sept. 1972, pp. 1193–1199.
14. Cebeci, T.; and Smith, A.M.O.: Analysis of Turbulent Boundary Layers. Academic Press, New York, 1974.
15. Levine, J.N.: Transpiration and Film-Cooling Boundary Layer Computer Program, Vol. I: Numerical Solutions of the Turbulent Boundary Layer Equations With Equilibrium Chemistry. Final Report. NASA CR–125683, 1971.
16. Fowler, J.R.: GASPLUS User's Manual. Version 2.3, NASP CR–1012, 1988.
17. Jankovsky, R.S.; and Kazaroff, J.M.: A Life Comparison of Tube and Channel Cooling Passages for Thrust Chambers. NASA TM–103613, 1990.
18. Pavli, A.J.; Kazaroff, J.M.; and Jankovsky, R.S.: Hot Fire Fatigue Testing Results for the Compliant Combustion Chamber. NASA TP–3223, 1992.
19. Hendricks, R.C.; Baron, A.K.; and Peller, I.C.: GASP: A Computer Code for Calculating the Thermodynamic and Transport Properties for Ten Fluids: Parahydrogen, Helium, Neon, Methane, Nitrogen, Carbon Monoxide, Oxygen, Fluorine, Argon, and Carbon Dioxide—Enthalpy, Entropy, Thermal Conductivity, and Specific Heat. NASA TN–D–7808, 1975.
20. Huff, V.N.; Fortini, A.; and Gordon, S.: Theoretical Performance of JP–4 Fuel and Liquid Oxygen as a Rocket Propellant. NACA RM–E56D23, 1956.
21. Gordon, S.; and McBride, B.J.: Computer Program for Calculation of Complex Chemical Equilibrium Compositions, Rocket Performance, Incident and Reflected Shocks, and Chapman-Jouguet Detonations. NASA SP–273, 1971.
22. Sutton, G.P.: Rocket Propulsion Elements: An Introduction to the Engineering of Rockets, Fifth Edition. John Wiley & Sons, New York, 1986.